
Single-Cell Analysis of Event-Time Correlations in Signaling Cascades

Alexandra Murschhauser



Munich 2019

Einzelzell-Analyse von Ereigniszeit-Korrelationen in Signalkaskaden

Alexandra Murschhauser



München 2019

Single-Cell Analysis of Event-Time Correlations in Signaling Cascades

Alexandra Murschhauser



Munich 2019

Einzelzell-Analyse von Ereigniszeit-Korrelationen in Signalkaskaden

Dissertation

an der
Fakultät für Physik
der
Ludwig-Maximilians-Universität München

vorgelegt am
26. April 2019

von
Alexandra Murschhauser
geboren am 11. Dezember 1990 in Traunstein

betreut von
Prof. Dr. Joachim O. Rädler

Single-Cell Analysis of Event-Time Correlations in Signaling Cascades

Dissertation

at the
Faculty of Physics
of the
Ludwig-Maximilians-Universität München

submitted on
26 April 2019

by
Alexandra Murschhauser
born on 11 December 1990 in Traunstein

supervised by
Prof. Dr. Joachim O. Rädler

Erstgutachter: Prof. Dr. Joachim Rädler

Zweitgutachter: Prof. Dr. Angelika M. Vollmar

Tag der mündlichen Prüfung: 26.06.2019

Contents

Associated Publications	xiii
Zusammenfassung	xv
Abstract	xvii
1 Introduction	1
2 Fundamental Concepts and Methods	5
2.1 Single-cell Time-lapse Measurements	5
2.2 Apoptosis	7
2.3 Data Acquisition	10
2.3.1 Image Acquisition	10
2.3.2 Single-cell Fluorescence Readout	11
2.4 Photochemistry and Mode of Action of Fluorescence Markers	12
2.4.1 Lysosomal Membrane Permeabilization - LysoTracker	13
2.4.2 Mitochondria Outer Membrane Permeabilization - TMRM	14
2.4.3 Reactive Oxygen Species Indicating Cellular Stress - CellROX	17
2.4.4 Calcium Release out of the Endoplasmatic Reticulum - Calbryte	20
2.4.5 Caspase-3/7 Activation - CellEvent Caspase Marker	21
2.4.6 Phosphatidylserine Flip to the Outer Membrane - pSIVA-IANBD	23
2.4.7 Plasma Membrane Permeabilization - Toto-3-/Propidium Iodide	24
2.5 Data Analysis	26
2.5.1 Maximum-likelihood Fitting and Extraction of Parameters	26
2.5.2 Interactive Fitting	29
2.5.3 Principal Component and Cluster Analysis	30
3 Event-Time Correlations in NP induced Apoptosis	33
3.1 State of the Art	33
3.1.1 Signaling Pathways Induced by PS-NH ₂ Nanoparticles	33
3.1.2 Staurosporine Induced Cell Death Pathways	36
3.1.3 Comparison to an External Apoptosis Trigger: the Fas-Ligand	36
3.2 Nanotoxicity Screening	38
3.3 Correlations in the Initiation Phase: LMP, MOMP and ROS	40
3.4 The Execution Phase: Caspases, PhS-Flip and Final Cell Death	47
3.5 Correlation between Reactive Oxygen Species and LMP or MOMP	49
3.6 Cathepsin Inhibition with Pepstatin A	51

3.7	Comparison with an External Cell Death Inducer: the Fas-Ligand . . .	53
3.8	The Delay Time Distribution Function	55
4	Correlation Analysis in Combinatorial Chemotherapy of Etoposide and PS89	57
4.1	State of the Art	57
4.2	PS89, a Potential Effect Enhancer of Etoposide	62
4.2.1	Analysis of the Signaling Cascade	62
4.2.2	Quantitative Noise Analysis of Heterogeneity in Cell Response	69
4.2.3	The Distribution Function of Delay Times	72
4.2.4	Quantitative Evaluation of Synergistic Effects of PS89	73
4.2.5	Triple Marker Correlations	75
4.3	Discussion and Outlook	77
5	Investigation of a 3D Environment For Single-cell Applications	79
5.1	State of the Art	79
5.2	Quantitative Analysis of Autofluorescence of Microwell Materials . . .	88
5.3	Analysis of Biocompatibility of Microwell Materials	90
5.4	Summary and Outlook	92
5.5	Application: Time-resolved Proliferation Study of MDS Stem Cells .	94
5.5.1	State of the Art	94
5.5.2	Single-Cell Time-lapse Setup	97
5.5.3	Results and Discussion	100
5.5.4	Outlook	102
6	Conclusion and Outlook	103
6.1	3D Microwells for Adherent Cells in Apoptosis Studies	105
6.2	The Future of Deep Machine Learning in Biological Data	106
	Bibliography	107
A	Methods and Standard Protocols	129
A.1	Cell Culture	129
A.2	Microscale Plasma-Initiated Protein Patterning (μ PIPP)	136
A.3	Protocol for the Fabrication of 3D PDMS Multi-Cell-Wells	139
A.4	Fluorescence Microscopy	141
	List of figures	145
	List of abbreviations	147
	Danksagung	149

Associated Publications

- P1** Murschhauser, A., Röttgermann, P. J., Woschée, D., Ober, M. F., Yan, Y., Dawson, K. A., Rädler, J. O. (2019). A high-throughput microscopy method for single-cell analysis of event-time correlations in nanoparticle-induced cell death. *Nature Communications biology*, 2(1), 35.
- P2** Chatzopoulou, E. I., Raharja-Liu, P., Murschhauser, A., Sekhavati, F., Buggenthin, F., Vollmar, A. M., ... & Rädler, J. O. (2018). A single-cell micro-trench platform for automatic monitoring of cell division and apoptosis after chemotherapeutic drug administration. *Scientific Reports*, 8.
- P3** Reiser, A., Zorn, M. L., Murschhauser, A., & Rädler, J. O. (2018). Single Cell Microarrays Fabricated by Microscale Plasma-Initiated Protein Patterning (μ PIPP). In *Cell-Based Microarrays* (pp. 41-54). Humana Press, New York, NY.
- P4** Hansjosten I., Rapp J., Reiner L., Vatter R., Fritsch-Decker S., Peravali R., Palosaari T., Joossens E., Gerloff K., Macko P., Whelan M., Gilliland D., Ojea-Jimenez I., Monopoli M. P., Rocks L., Garry D., Dawson K., Röttgermann P. J. F., Murschhauser A., Rädler J. O., Tang S. V. Y., Gooden P., Belinga-Desaunay M. A., Khan A. O., Briffa S., Guggenheim E., Papadiamantis A., Lynch I., Valsami-Jones E., Diabaté S., Weiss C. (2018). Microscopy-based high-throughput assays enable multi-parametric analysis to assess adverse effects of nanomaterials in various cell lines. *Archives of toxicology*, 92(2), 633-649.
- M5** Murschhauser A., Woschée D., Braig S., Angelika M. Vollmar, Rädler J. O., Targeting the ER-Mitochondria Interface Sensitizes the Leukemia Cells towards Cytostatics, in preparation.
- M6** Kyncl M., Bast L., Murschhauser A., Schuh L., Thomas M., Götze K., Marr C., Rädler J. O., Time-resolved Analysis of Stem Cell Proliferation and Differentiation, in preparation.
- M7** Woschée D., Murschhauser A., Strey H., Rädler J. O., Modeling signaling cascades based on single-cell event-time correlations, in preparation.

Zusammenfassung

Die Heterogenität von zellulären Reaktionen auf Zelltodinduktoren ist enorm und daher wichtig zu analysieren. Endpunktmessungen mit gemittelten Ergebnissen von Gesamtzellpopulationen können Heterogenität in komplexen Signalnetzwerken nicht auflösen. In dieser Arbeit wurden Methoden zu Ereigniszeit-Korrelationen von Fluoreszenzmarkern auf Einzelzellebene etabliert und in einer Nanotoxizitätsstudie sowie in einer kombinatorischen Chemotherapiestudie (in vitro) angewendet. Die paarweisen Zeitkorrelationen von Ereignissen in Fluoreszenzzeitverläufen einzelner Zellen ermöglichen es, die zeitliche Reihenfolge von apoptotischen Schlüsselereignissen in Signalkaskaden festzulegen und die Wirkungsweise und Synergie von Kombinationen von zelltodinduzierenden Agentien zu quantifizieren.

Fluoreszenzmarker sind ein wichtiges Werkzeug um biologische Ereignisse sichtbar zu machen. In dieser Studie wurden die Marker für paarweise Ereigniszeit-Korrelationen verwendet. Die Marker zeigen apoptotische Veränderungen in Lysosomen, Mitochondrien (MOMP), im oxidativen Stresslevel (OxBurst), der Kalziumfreisetzung, der Caspase-Aktivität, dem Flip von Phosphatidylserin und die Permeabilisierung der Plasmamembran an. Nach der Untersuchung der Photochemie, Wirkungsweise sowie die Funktionalität der Marker für Zeitraffer-Messungen, wurden die gewonnenen Erkenntnisse in der automatisierten Lebendzellmikroskopie auf Einzelzell-Feldern (LISCA) angewendet. Dies ist ein Raster-Zeitraff Verfahren, um parallele Bildreihen mit hunderten von Einzelzell-Fluoreszenzsignalen aufzunehmen. Spezifische Merkmale der Einzelzell-Zeitspuren wurden dann mit phänomenologischen Funktionen gefittet, um Ereigniszeiten zu extrahieren.

Nanotoxizitätsstudien auf Einzelzellebene geben Einblick in Wechselwirkungen zwischen Nanopartikeln (NP) und Zellen. Zeitkorrelationen und Verzögerungszeit-Verteilungsfunktionen legten dar, dass in der durch 58 nm amino-modifizierte Polystyrolnanopartikel (PS-NH₂) induzierten Signalkaskade in menschlichen Lungenkrebszellen (A549) der lysosomale Weg ausgelöst wurde. Darüber hinaus konnte erstmals gezeigt werden, dass bei einer hohen Konzentration an NPs ein sekundärer, mitochondrialer Weg existiert. Der zweite Signalweg ist in Huh7, einer Leberkrebs-Zelllinie, nicht zu beobachten.

Chemosensibilisatoren ermöglichen es, die Dosis von Zytostatika, welche starke Nebenwirkungen und Zytotoxizität verursachen, zu senken. Daher wurden die Signalwege und Auswirkungen des neuartigen Sensibilisators PS89 im kombinatorischen Chemotherapieansatz mit dem Zytostatika Etoposid (ETO) untersucht. Die apoptotische Signalabfolge beinhaltet in allen drei Expositionen ETO, PS89 und der Kombination von beiden, die gleiche Reihenfolge von Ereignissen: MOMP und OxBurst wurden fast gleichzeitig induziert, gefolgt von der Freisetzung von Ca²⁺ Ionen.

Zudem wurde durch den Vergleich mit einer Modellierung unabhängiger Ereignisse (Bliss) die Synergie der Ereignisse evaluiert, welche vermutlich bei der Auswertung der Plasmamembranpermeabilisierung indiziert wurde.

Um das Verhalten von nicht-adhärenenten Zellen im Hochdurchsatz zu untersuchen, ist der Bedarf an mikrostrukturierten Plattformen zur Positionierung einzelner Zellen, z.B. definierte Vertiefungen, sogenannte Mikrowells, offensichtlich. Aus diesem Grund wurden verschiedene Materialien auf ihre Eignung als Mikrowellmaterial untersucht. Zwei kritische Parameter wurden identifiziert: Geringe Autofluoreszenz für ein eindeutiges Signal und hohe Biokompatibilität.

Als erste Machbarkeitsstudie zu PDMS-Mikrowells wurde die Proliferation und Apoptose gesunder Stammzellen und Stammzellen mit myelodysplastischem Syndrom (MDS) untersucht, was Aufschluss über die Entwicklung der Krankheit gibt. Vorläufige Ergebnisse zeigen, dass die Zeit bis zur ersten Teilung sowie die Zellzyklusdauer beider Zelltypen ähnlich waren, während die apoptotische Rate bei MDS-Zellen leicht erhöht war.

Ereigniszeit-Korrelationen und Verzögerungszeit-Verteilungsfunktionen auf Einzelzellebene sind ein überzeugendes Werkzeug, um Zusammenhänge zwischen statistischen Ereignissen in Signaltransduktionskaskaden und deren chronologische Abfolge zu untersuchen. Insgesamt ermöglichen Ereigniszeit-Korrelationen auf Einzelzellebene eine breit angelegte systembiologische Sicht auf zelluläre Signalwege und die Kinetik der Signalübertragung.

Abstract

The heterogeneity of cellular reactions to cell death inducers is enormous and therefore important to analyze. Endpoint measurements with averaged results of total cell populations cannot resolve the heterogeneity in complex signaling networks. In this work, methods for event-time correlations of fluorescence markers at the single-cell level were established and applied in a nanotoxicity and a combinatorial chemotherapy study (*in vitro*). The pairwise correlations of event-times, obtained from fluorescence time courses of individual cells, allow the determination of the temporal sequence of apoptotic key events in signal cascades and to quantify the mode of action and synergy of combinations of cell death inducing agents.

Fluorescence markers are an important tool to visualize biological events. In this study, such markers were used for pairwise event-time correlations indicating apoptotic changes in lysosomes, mitochondria (MOMP), oxidative stress level (OxBurst), calcium release, caspase activity, phosphatidylserine flip, and plasma membrane permeabilization. Initially, the photochemistry, mode of action and functionality of the markers for time-lapse measurements were investigated. The insights gained were then implemented on automated live-cell imaging on single-cell arrays (LISCA). LISCA is a scanning time-lapse technique for the recording of parallel image series with hundreds of single-cell fluorescence signals. Specific features of single-cell time traces can then be fitted with phenomenological functions to extract event-times.

Single-cell nanotoxicity studies can provide insights into interactions between nanoparticles (NP) and cells. This study showed, by means of time correlations and delay-time distribution functions, that the lysosomal pathway was triggered in human lung cancer cells (A549) upon interaction with 58 nm amino-modified polystyrene nanoparticles (PS-NH₂). Furthermore, a secondary mitochondrial pathway was shown for the first time to exist in parallel at a high concentration of NPs. Interestingly, this second pathway was not observed in the liver cancer cell line Huh7.

Chemosensitizers make it possible to reduce the dose of cytostatics, which cause tremendous side effects and cytotoxicity. Therefore, the signaling pathways and effects of the novel sensitizer PS89 were investigated in a combinatorial chemotherapy approach with the cytostatic agent etoposide (ETO). It was found that the sequence of events in the apoptotic pathway was similar, irrespective of whether ETO and PS89 were incubated with cells separately or simultaneously: MOMP and OxBurst were induced almost coincidentally, followed by the release of Ca²⁺ ions. In addition, the synergy of the events was evaluated by comparison with a modelling of independent events (Bliss), indicating synergistic effects by analyzing the plasma membrane permeabilization.

In order to investigate the behavior of non-adherent cells in high-throughput, the need for microstructured platforms for positioning individual cells, e.g. defined wells, so-called microwells, becomes apparent. Therefore, various materials were investigated for their suitability as microwell materials. Two critical parameters were identified: Low autofluorescence for a clear signal and high biocompatibility.

As a first feasibility study on PDMS microwells, the proliferation and apoptosis of healthy stem cells and stem cells with myelodysplastic syndrome (MDS) were investigated, providing information on the development of the disease. Preliminary results show that the time to first division and the cell cycle duration were similar for both cell types, while the apoptotic rate was slightly increased in MDS cells.

In summary, event-time correlations and single-cell delay-time distribution functions are a powerful tool to investigate correlations between statistical events in signal transduction cascades and the chronological sequence. Overall, event-time correlations at the single-cell level provide a broadly applicable systems biology view of cellular pathways and the kinetics of signal transmission.

Chapter 1

Introduction

Cum hoc ergo propter hoc.

With this, therefore because of this.

This well-known phrase from the field of philosophy describes the fallacy of spurious causality. But correlation does not imply causation - Cum hoc non est propter hoc. At a first glance, it seems likely that the correlation or the temporal and local presence of two events (coincidence) are underlying causal dependency. But causation is not proven neither with a correlation nor with coincidence (post hoc ergo propter hoc). To prove causation, first, the relation between two events (cause-and-effect-relationship) has to be determined (Figure 1.1). Is event A caused by Event B? Or requires event A event B? Or are both events caused by another event x? In principle, each case could be true, but has to be proven first to state causation.

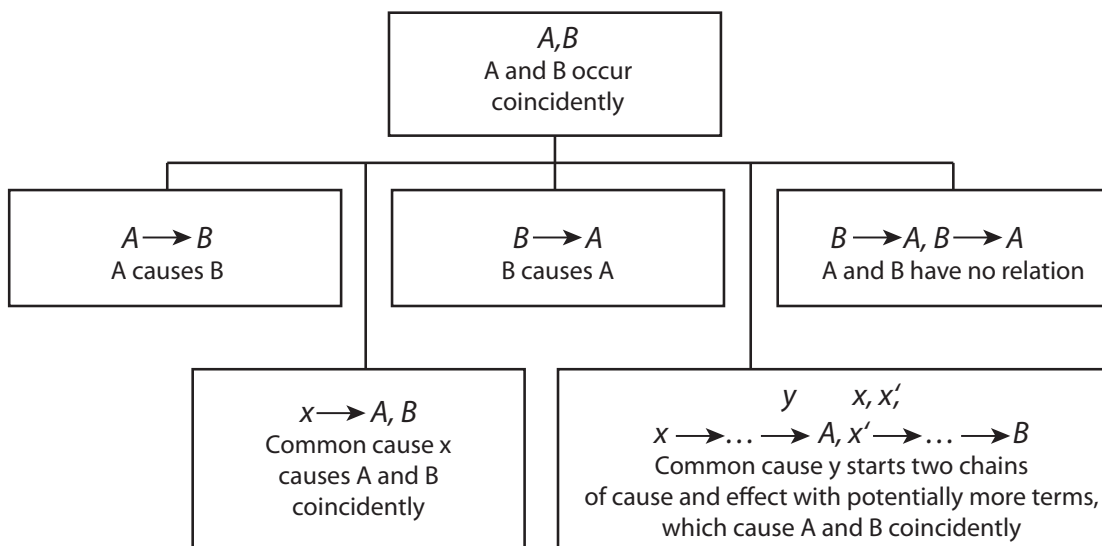


Figure 1.1: Relation between cause and correlation.

Correlation (latin: *correlatio*, interdependence) is a statistical term for a relation between two or more events, objects, attributes, conditions or functions, which neither implies causation nor is implied by it. Correlation is the connection or relationship between two variables, while causation implies a cause-and-effect-relationship. In short, a correlation only describes an existing relationship and causation clarifies which event causes the other. Statistically, the measure for a linear correlation between two variables can be quantified with the correlation coefficient according to Pearson or Bravais. The measured value can range from zero (no correlation) to one (correlation is present). Further, it is distinguished between positive (e.g.: The more, the better.) and negative correlations. The case of no correlation can be analyzed with statistical tests such as the Null Hypothesis. Is the correlation between two events assessed, causation can be attempted to be answered.

Also high-dimensional data in complex biological networks desire the investigation of causal structures. In gene expression and proteomics data, correlation networks are already frequently applied [1]. The field of system biology, where it is aimed to be understood how the cellular organization determines behavior and interaction as well as how the assembly of cell community is organized, is interested in linking correlations with causality [2]. The correlative analysis of large cellular signaling networks provides the power to test mechanistic hypothesis. Further, sufficient data, in combination with causal models, intend to draw predictions [2]. But to prove causation, well-designed experiments with as many as possible randomized factors to exclude any interferences or side effects, are needed. However, in many cases this is impossible due to infinite factors or experimental parameters or the impossibility to change some factors. Further, such experiments are cost and time intensive as well as complex to realize.

On the other hand, statistical analysis could help to draw directional relationships out of the correlation data. For example, mediation analysis is a good theoretical model to clarify the underlying mechanisms of relationship between an independent variable and a dependent variable with the help of a so called hypothetical mediator variable [3]. Also here, the direct causation can not be proven, rather the characteristic of the relationship between the two variables. In summary, a critical experimental, theoretical and statistical verification has to be given to state causation between variables.

In this work, correlations between apoptosis events in signaling cascades were analyzed. However, the correlations give a first insight into the complex network of signaling, but no causal relationships between the events were drawn.

Single-Cell Event-Time Correlations

The underlying mechanisms and pathways leading to cell death can not be fully unraveled by standard end-point bulk measurements [4, 5]. In bulk assays, where the signal is averaged over the whole population of cells, the heterogeneity of the cellular response remains hidden. But heterogeneity can be fundamental in some biological processes [6]. The-cell-to-cell variability is assumed to be caused by noise or stochasticity in gene expression (intrinsic noise) as well as by extrinsic noise (external factors) [7]. Further, if the response of the cell population is not uniformly, the average-based analysis masks potential sub-populations [8].

Moreover, mostly the readout is end-point and performed only at limited time points, thus just giving a snapshot of the whole kinetics. But time-lapsed movies enable the continuous monitoring of cells over hours to days to follow the whole dynamics of the observed phenomena [9].

In this work, single-cell measurements facilitated the analysis of the heterogeneous cell response to an apoptosis inducer and the identification of potential sub-populations. Furthermore, time-lapse measurements were performed to follow the underlying dynamics in the course of apoptosis. Therefore, cells were seeded on microstructured surfaces for a dynamic readout of single cells. Defined geometries of adhesive protein areas, isolated by cell-repellent surroundings, were achieved by microscale plasma-initiated protein patterning (μ PIPP) [10]. The micropatterns provide standardized boundary conditions for the extraction of single-cell time trajectories. Fully automated data acquisition allows the observation of hundreds of cells in parallel over long periods of time with a high time resolution in up to four different fluorescence channels. Furthermore, pair-wise event time correlations are a powerful tool to unravel signaling cascades, e.g. in apoptosis. Therefore, different marker combinations are measured in parallel per cell to resolve the chronological order of events within one cell. The assessment of multiple events within one cell enable the disclosure of potential correlations between the measured events. Accordingly, with dual correlations of the events, the signaling cascade and its temporal context can be assembled.

The semi-automated fluorescence readout generates time traces of single cells. Accordingly, the so called event times are extracted from the time courses with maximum-likelihood fitting. The detected event times are then correlated pair-wise via Principal Component and Cluster Analysis to unravel the temporal relationship within the signaling transduction. These event-time correlations compose the signaling pathways in the induced apoptosis.

Apoptosis Exploiting for Cancer Therapy

Apoptosis, a form of programmed cell death, is necessary for the homeostasis of cells in normal tissues to remove senescent, excessive or altered cells without causing

inflammation [11]. Further, apoptosis was found to contribute to a high cell loss in malignant tumors and promote tumor progression [12]. Thus, anticancer agents were developed to induce apoptosis, but tremendous side effects and cytotoxicity in chemotherapy are caused by the fact that cytostatics also trigger apoptosis in normal tissue [12]. The precise manipulation of the cell death program would lead to less toxic and mutagenic therapy than the present approaches.

Hence, in the 1960s, the development of *combinatorial chemotherapy* paved the way to overcome the problems of cancer resistance and the detrimental side effects [13]. The idea is to provoke cell death with lower concentrations of cytostatics with the support of so called chemosensitizer, which increase the vulnerability of cancer cells towards apoptosis. The reduced concentration of anticancer agents increases the chances of survival as well as the well-being of the patients. Further, the double-sided offense of the agents with different target sides increase the probability of the success potential for recovery and the absence of potential relapses.

Moreover, in the 1980s, signaling networks were found to be modified in cancer cells and *targeted therapy* was a new promising approach in cancer research [13]. Signaling cascades have a highly complex and pretentious nature. Thus it is challenging to unravel the sequence of key players and the chronological order in signaling pathways. But the identification of main check points allocates new potentially specific targets, which could be addressed in cancer therapy. Further, the analysis of the crosstalk between such main actors in signaling networks provides insight into sensitivity and resistance for rational therapeutic intervention strategies [14].

In this study, on the one hand, the apoptosis signaling cascades of one type of nanoparticles (PS-NH₂) was examined, and on the other hand, a combinatorial chemotherapy approach was investigated to understand the underlying cell death pathways.

Overview of this work

In this work, the second chapter introduces the **Fundamental Concepts and Methods**. Further, this study makes a contribution to the understanding of the underlying mechanisms in apoptotic signaling pathways induced with PS-NH₂ nanoparticles, which is described in chapter 3, **Event-Time Correlations in NP induced Apoptosis**. Correlations between key players in signaling pathways triggered by the combinatorial approach of the cytostatic Etoposide and the chemosensitizer PS89 are part of chapter 4, **Correlation Analysis in Combinatorial Chemotherapy of Etoposide and PS89**. Autofluorescence and biocompatibility tests of different potential microwell materials are described in the fifth chapter, **Investigation of a 3D Environment For Single-cell Applications**. Further, an application of PDMS microwells is delineated, namely a proliferation study of stem cells. Finally, the last chapter six provides a short **Conclusion and Outlook**.

Chapter 2

Fundamental Concepts and Methods

2.1 Single-cell Time-lapse Measurements

Since many years, biological bulk assays are widespread used to investigate the toxicity of different materials. For example, the 3-(4,5-dimethylthiazol-2-yl)-2,5-diphenyl-tetrazolium bromide (MTT) test, a colorimetric assay to analyze the metabolic activity in cells, is applied frequently. And since the metabolic activity correlates with cell viability, it is often used as cytotoxicity assay. However, here we face the first problem: is the signal due to many smaller cells, which metabolize less of the dye than the average signal or stems the signal from few big cells, which have a higher metabolism? Secondly, this average signal from bulk assays masks signals from subpopulations completely. But the heterogeneity of the cells in response and timing can be tremendous (Figure 2.1).

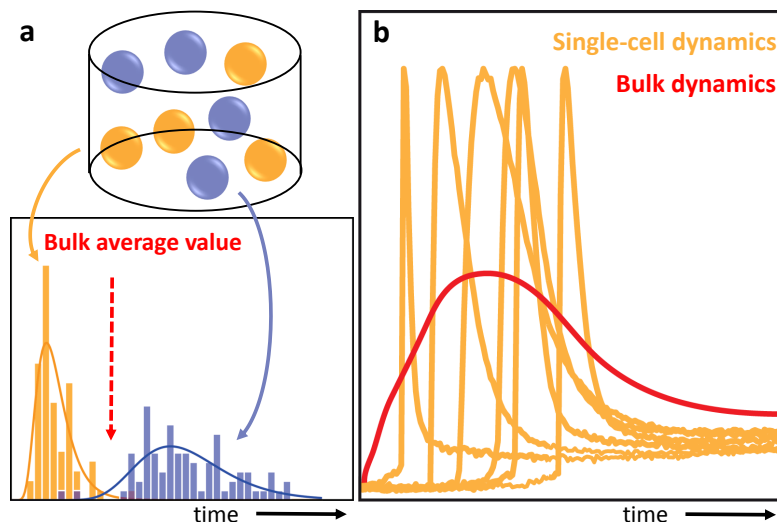


Figure 2.1: a) In bulk measurements the heterogeneity of the population is missed and potential subpopulations are masked in an averaged signal. b) Bulk measurements can give misleading information about dynamics of processes. Also end-point values, which are assembled to one presumed dynamic can result in incorrect outcomes (red time course). Figure adapted from [15].

The cell-to-cell variability is highly diverse and can have different origins. For example, genetic and epigenetic differences, intrinsic noise, differences in cell cycle or variations in reactions due to concentration differences were identified as potential causes in cell response [16].

The need of single-cell assays was realized in the past [5, 9, 17, 18] and first nanotoxicity studies at the single-cell level were published utilizing different techniques [17, 19–21]. But not only for nanotoxicity, also for stem cell research, the need for single-cell arrays was found and successfully implemented [4, 8, 22]. Also, mathematical models can support the understanding of signaling pathways [23, 24]. Nevertheless, there is little knowledge about the heterogeneity in intracellular reactions and further investigations have to be done.

To track single cells, they can be seeded in a low concentration on a cell-friendly surface, where the cells can migrate freely. But this method requires a time-consuming, laborious and often user intensive (manual) data analysis due to the movement of the cells and the change in morphology. In this work, the microscale plasma-initiated protein patterning (μ PIPP) [10] facilitates an automated high-throughput readout of single cells. Single-cell arrays provide uniform conditions for all cells by reduction of external confounding factors and by exclusion of cell-to-cell-communication due to the adequate distance to neighboring cells. Thus, a precise confinement of the cells on the surface without distracting them, is crucial for tracking hundreds or thousands of cells in parallel, possibly with different readout parameters. Another common single-cell read-out technique, which is not surface-based, is flow cytometry, but the readout is end-point only [25, 26]. Time dependent measurements with coarse grained time intervals are possible with flow cytometry, when samples are prepared at different time points and sorted one after another. Besides to flow cytometry, automated microscopy, laser scanning cytometry, capillary electrophoresis or laser capture microdissection are recently used single-cell techniques. However, they have all the disadvantage of low throughput and constrained applicability in common [27].

On the other hand, time resolved measurements were performed in the past, for example ECIS (Electric Cell-Substrate Impedance Sensing), where the impedance as a function of time after addition of an external stimulus is measured. But also here we have a bottleneck, namely that the signal is averaged over the whole monolayer. Endpoint assays give just a snapshot of dynamics, thus they are limited in information. Even more, information is lost and just a piece of the whole picture is given. Live cells observed in real time give much more information than end-point readouts: not only the dynamics of cell fate decisions can be followed (e.g. variations in signaling, time interval of signal change, oscillating behavior etc), but also the morphology of the cells as well as a quality control of the assay conditions can be analyzed. For example, parameters such as patterning quality and stability over time, indicated by migrating cells out of the adhesion sites, can be tracked. Further, the time-lapsed images can be used to analyze how many and how often cells divided

before cell death, which can give a hint of correlations between proliferation and cell death decisions. Time-lapse experiments have the power to identify atypically behaving cells and thus these cells can be excluded from the analysis, when they, for example, migrate, divide or detach. Cells, which are dead from the beginning of the experiment, can be excluded as well. This manual selection gives a high quality of data and less false positive or false negative results.

However, some limitations still remain, which can be the bottleneck for performing time-lapse measurements [5]. Although just a microscope, a camera, an incubation box with controlled temperature, CO₂ and humidity and an automated stage is needed as experimental setup, phototoxicity, photobleaching of the used fluorescence markers and biocompatible environments can cause major problems.

Furthermore, data management, handling and processing gained a lot of attention in the past years tagged with the buzzword 'big data'. In fact, such time-lapse measurements over some days with hundreds of field of views can range to some Terabytes. Furthermore, the extraction and the processing of information out of these huge data sets causes problems. Despite the fact, that already some tracking software is on the market [4, 28–31], the identification and continuous tracking of single cells, especially suspension cells, can be challenging due to the fast movement of cells in solution. For adherent cells, contour analysis would be advantageous to gain accurate and high content information, which could include morphological changes during cell death, for example [29]. However, since experimental conditions vary between the different setups and projects, e.g. the contrast of the cells to the surface differs or no fluorescence is present, optimum cell recognition is still under investigation.

To counter act these issues, the advantages of single-cell and time-lapse measurements were combined and continuous dynamics of single cells were recorded in this study.

2.2 Apoptosis

How is cell death classified?

The Nomenclature Committee on Cell Death (NCCD) has classified major regulated cell death (RCD) subroutines [32]. It is distinguished between mitochondrial permeability transition-driven necrosis, necroptosis, ferroptosis, pyroptosis, parthanatos, entotic cell death, NETotic cell death, lysosome-dependent cell death, autophagy-dependent cell death, immunogenic cell death and intrinsic and extrinsic cell death (Figure 2.2). In this work, the focus will be on the signaling pathways of apoptosis, especially the intrinsic apoptosis, since the used apoptosis trigger are intrinsic ones. A short outline for extrinsic pathways is given in Chapter 3.1.3.

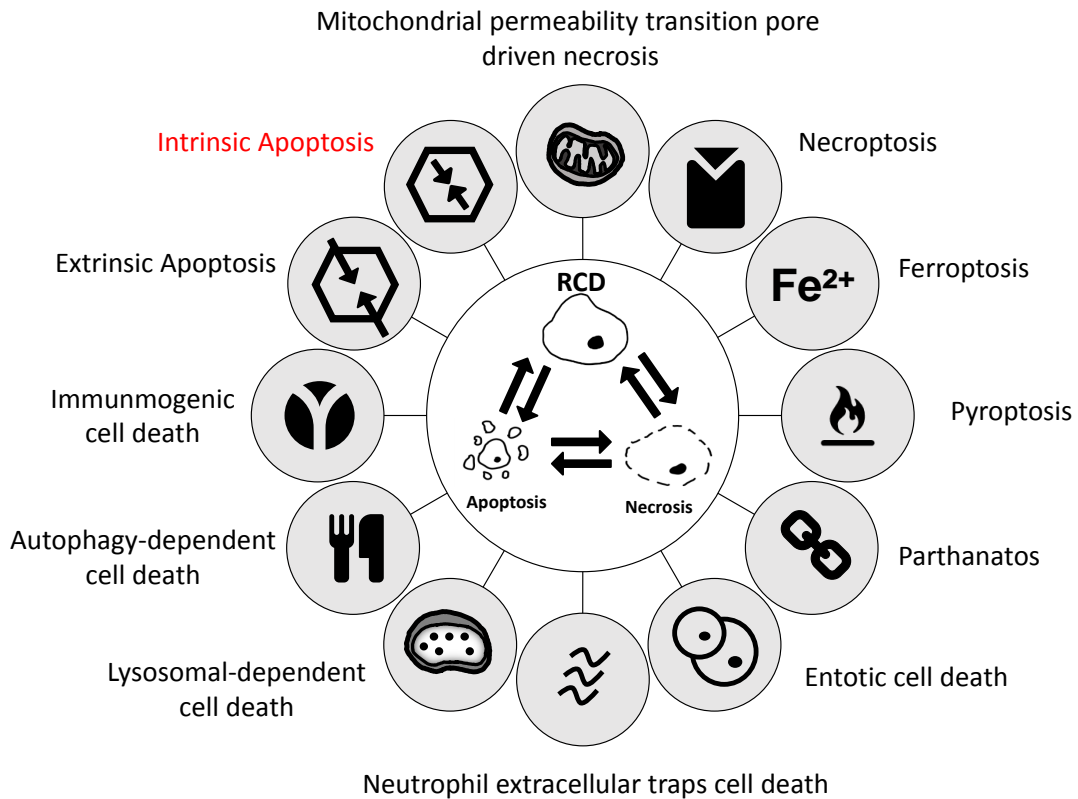


Figure 2.2: Overview of cell death types. Twelve different types of cell death are distinguished by the Nomenclature Committee of Cell Death 2018. Figure adapted from [32].

How is apoptosis defined?

Following the recommendations of the NCCD 2018, cell death can be classified by morphology [32]. One class is apoptosis, which is described as the following: "... Type I cell death or apoptosis, exhibiting cytoplasmic shrinkage, chromatin condensation (pyknosis), nuclear fragmentation (karyorrhexis), and plasma membrane blebbing, culminating with the formation of apparently intact small vesicles (commonly known as apoptotic bodies) that are efficiently taken up by neighboring cells with phagocytotic activity and degraded within lysosomes; ..." [32] (Figure 2.3). Apoptosis is programmed cell death (PCD), a particular form of RCD, and is therefore distinguished from necrosis, which is a form of traumatic cell death and induced by external factors, thus a rather spontaneous cell death than a planned, programmed and targeted cell death. Necrosis can be discerned from apoptosis easily by morphological changes, since necrotic cells increase in size until the cell membrane ruptures;

no apoptotic bodies are formed. Further, necrosis is causing inflammation, which is not the case for apoptosis.

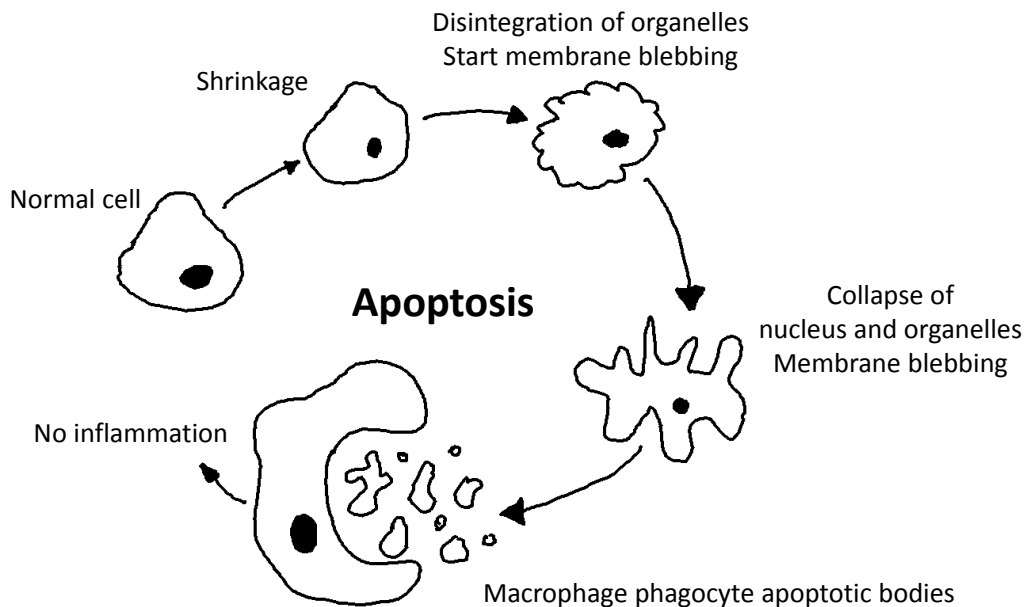


Figure 2.3: Process of apoptosis. In the first step the cell shrinks, also the nucleus and the organelles. The organelles start to disintegrate and the membrane begins to bleb until the membrane is completely blebbing and the organelles and the nucleus collapse. In the final stage, the apoptotic bodies are engulfed by macrophages. Figure is adapted from [33].

When is a cell dead?

The process of dying is as long as reversible until the 'point-of-no-return' turns the process into irreversible. Executioner caspases, the loss of outer mitochondria membrane potential, the flip of phosphatidylserine as well as the loss of plasma membrane potential was discussed as such a point-of-no-return [34]. However, all these suggestions were refuted in the past by different studies [35]. If no defined event can be identified as such reversal point, the NCCD stated a cell as dead, if any of the following criteria is given: (1) loss of plasma membrane potential, (2) the cell and also the nucleus are completely fragmented and/or (3) the corpse or the fragments were engulfed by neighboring cells [35]. Thus, dead cells have to be differentiated by dying cells, which are undergoing various pathways during this process.

2.3 Data Acquisition

2.3.1 Image Acquisition

For single-cell time-lapse measurements, microstructured slides were prepared as published elsewhere [10, 36–38]. A detailed standard protocol can be found in the Appendix A.2. In short, a PDMS 3D structured stamp is placed on a surface, which is plasma initiated afterwards. A PLL-PEG solution is added to the hydrophilic surface and is sucked underneath the stamp via capillary forces to gain non-adhesive, passivated areas. After incubation, the stamp is removed and protein squares are generated by the administration of a fibronectin solution on the sides, which were blocked by the stamp before. The standardized conditions help to track hundreds to thousands of single cells in parallel. Therefore, cells were seeded and after 6 h of cell adhesion the fluorescence markers as well as the apoptosis inducer were added. An inverted TI Eclipse microscope (Nikon) was used to set around 200 fields of view per sample. With a 10 minute interval, phase-contrast images and a maximum of three fluorescent images were acquired by a ClaraE CCD camera for each field of view over a period of 24–30 h at 10x magnification. The slide was kept at 37°C by an ibidi or an Okolab heating system. CO₂ supply was provided or CO₂ independent Leibovitz' L15 medium was used. The fluorescence time traces were obtained with fully automated data acquisition. Hence, the settings were scheduled with the JOBS tool in the NIS Elements AR 5.02.00 64-bit software. The obtained nd-files (proprietary Nikon format) were converted into TIFF files with a custom macro. The nd-files are sorted by channels over time and positions, but the TIFF files are then organized by position. So each TIFF file presents one position with all channels over time.

The automated live-cell imaging on single-cell arrays (LISCA) is represented in Figure 2.4. The overview scan of the micropatterned cell array in the middle (black) is zoomed in (on the left), where single cells on the pattern are shown. The fluorescence of different markers in single cells are depicted underneath. The following events or organelles are illustrated: the mitochondria (blue), lysosomes (cyan), the flip of phosphatidylserine (red), nucleus (brown), caspase activation (yellow), and OxBurst (purple). The scale bar represents 200 μm .

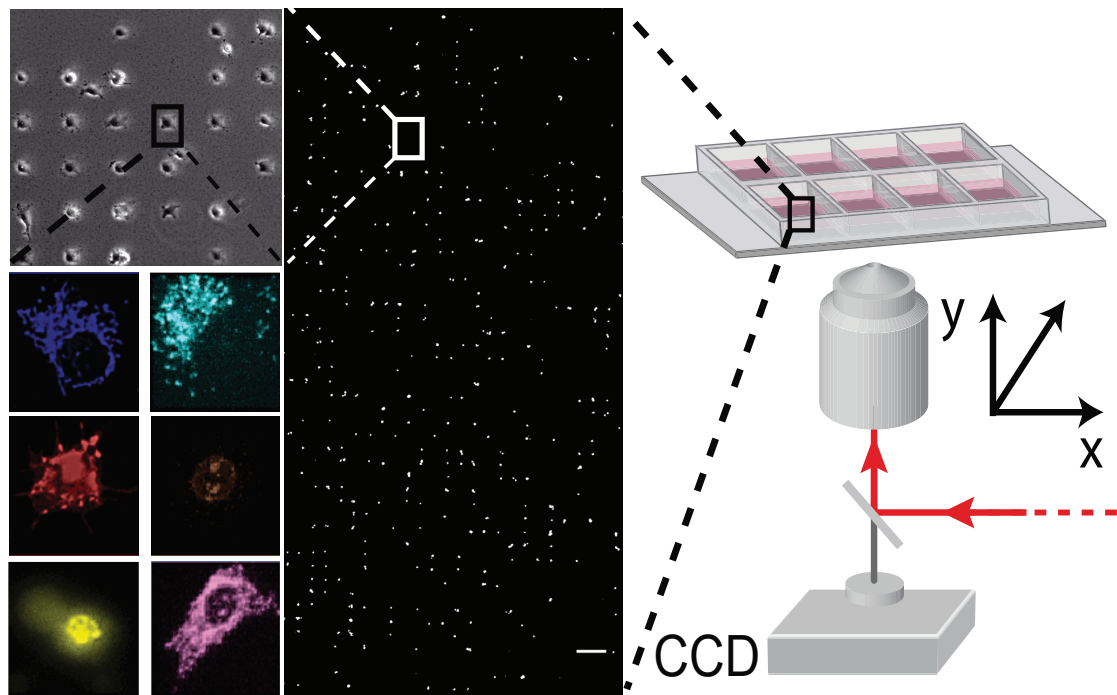


Figure 2.4: Automated live-cell imaging on single-cell arrays (LISCA). Cells are seeded on a micropatterned surface with $30 \times 30 \mu\text{m}$ adhesion sites. A cell array is shown in the middle, which is zoomed in to demonstrate the occupancy of the pattern by cells (on the left). Underneath, different events or organelles, illustrated with fluorescence markers are shown: the mitochondria (blue), lysosomes (cyan), the flip of phosphatidylserine (red), nucleus (brown), caspase activation (yellow), and OxBurst (purple). The scale bar represents $200 \mu\text{m}$. Adapted from [36], licensed under a Creative Commons license [39].

2.3.2 Single-cell Fluorescence Readout

The single-cell fluorescence readout was performed with the custom ImageJ plugin called Microwell Analysis, written by Christian Meggle, in ImageJ42. As a first step, the time-lapse image stacks were used to determine the time traces of single cells by defining a region of interest (ROI) grid corresponding to the fibronectin pattern in a semi-automated manner. Empty, multiple or displaced occupied adhesion sites were excluded from data analysis and sorted out by hand. Also doubling, migrating or detaching cells were not taken into account. ROIs, which are crossed by cell fragments, apoptotic bodies or nanoparticles were as well excluded, as this particles can be clearly seen as a peak in the time courses, which is interfering with the fitting routine. This manual, time and click intensive quality-control step is necessary to ensure to only evaluate single occupied ROIs. Then, the ordinary background correction, which is included in the plugin, is applied to the image stacks. Afterwards, the total fluorescence intensity is integrated for each ROI which is marked for analysis.

2.4 Photochemistry and Mode of Action of Fluorescence Markers

Since the discovery of fluorescence in 1904 by August Köhler and the development of fluorescence markers in the 50s, fluorescent dyes became a frequently used tool to observe and analyze cellular reactions, processes, activities and mechanisms [40].

In this work, we took a step forward and used pairwise marker combinations to gain a deeper insight into signaling cascades in cells. Usually, only one marker is added to the cell and several readouts are addressed with different markers, but in separate experiments [41, 42]. Afterwards, the chronological order is composed together out of these discrete experiments, which could be faulty, since the outcomes are not from the same cell. Here, we add mostly two, in some cases even three markers to the cells, addressing more than one target of interest. Therefore, this method provides multiparametric data from one and the same cell, which enables the possibility to draw direct relations between the signals, without the need of any assumptions. Of course, the more markers are added to the cell, the more direct would be the detected information. However, we realized that the viability of the cell and the tolerance of the fluorescence spectra are limited to three markers.

With this single-cell time-lapse data, not only signaling cascades in their chronological order can be determined, but moreover, the probability in response can be estimated. The high specificity and sensitivity of the markers as well as a good time resolution provide high quality data, which allows drawing statements with high precision and accuracy.

Several key events or checkpoints in the signaling cell death cascade were identified in the past to play an essential role leading to survival or cell death [43–46]. Depending on the apoptotic trigger, a specific type of pathway, either extrinsically or intrinsically, can be induced. Additionally, even within these pathways, the important events show huge variety depending on the cell death inducer and the cell line used [18].

Fluorescence markers are used as a tool to identify the involved events in the particular case and which events are essential for cell death. In the following chapter, the photochemistry and the biological background of the fluorescence markers, which were used to characterize the apoptotic behavior as well as the characteristic time courses, are explained in-depth.

The applied concentrations of all fluorescence markers, the corresponding absorption and emission wavelengths as well as the used exposure times for the markers can be found in the Appendix A.4.

2.4.1 Lysosomal Membrane Permeabilization - LysoTracker

In many investigated apoptosis signaling pathways, the first described apoptotic event in the signaling cascade is the lysosomal membrane permeabilization (LMP). The pH sensitive LysoTracker Deep Red (Thermo Fisher) is cell permeant and is often used to illustrate LMP *in vitro*. It labels acidic organelles in live cells due to the linkage of a weak base. It has an optimal excitation at 647 nm and an emission maximum at 668 nm. The chemical structure is shown in Figure 2.5.

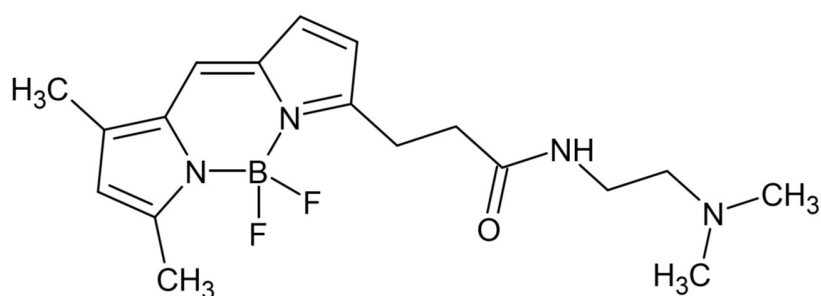


Figure 2.5: Chemical structure of the pH sensitive LysoTracker to stain acidic cell organelles.

For our setup, a low concentration of 75 nM was used, since it was staying in the media without any washing step for the whole measurement. In Figure 2.6, exemplary single-cell time traces of the LysoTracker in A549 cells are shown. Apoptosis was induced with $100 \mu\text{g mL}^{-1}$ PS-NH₂ NPs. The time traces show an initial fluorescence increase described by a parabolic function and a sigmoidal decrease of fluorescence follows. The typical offset in intensity is labeled as t_{LMP} and indicated with an arrow. Details of the phenomenological fits and the definition of events times can be found in the Chapter 2.5 and the Supplementary Information of Murschhauser et al. [36].

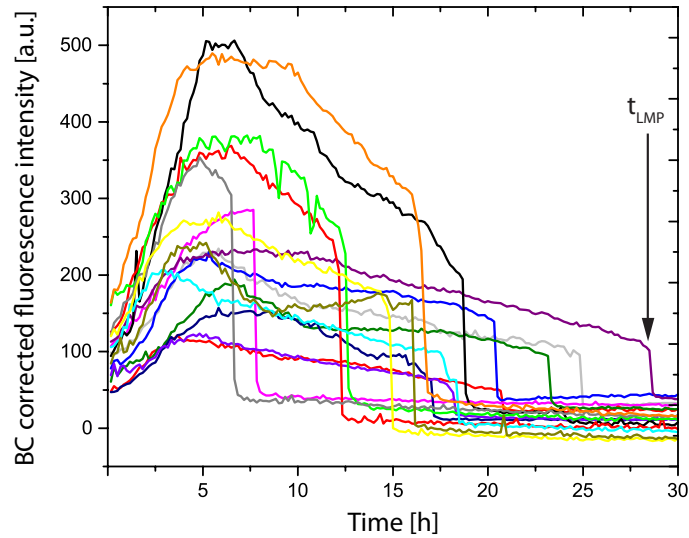


Figure 2.6: Exemplary 30 h time traces of LysoTracker green recorded after apoptosis induction with $100 \mu\text{g mL}^{-1}$ PS-NH₂ nanoparticles in A549 cells are shown. The lysosomal breakdown is indicated as t_{LMP} and labeled with an arrow.

The fluorescence molecules of the LysoTracker accumulate inside acidic organelles (lysosomes or late endosomes). In the acidic environment of these cellular organelles, the acidotropic marker is protonated, which significantly increases the fluorescence. Thus, in viable cells a bright fluorescence in the lysosomes is detected. Further, with the addition of an apoptosis inducer, we see a decrease in fluorescence. The offset in intensity is assumed to be correlated with the time point of LMP, thus the lysosomal collapse or breakdown, and is labeled as t_{LMP} .

2.4.2 Mitochondria Outer Membrane Permeabilization - TMRM

One central event in various signaling cascades is the mitochondria outer membrane permeabilization (MOMP), which is often referred as the point-of-no-return for the cell in cell fate decisions [34]. A widespread used fluorescence marker to elucidate MOMP is the lipophilic cationic tetramethylrhodamine methyl ester (TMRM) marker (Figure 2.7a).

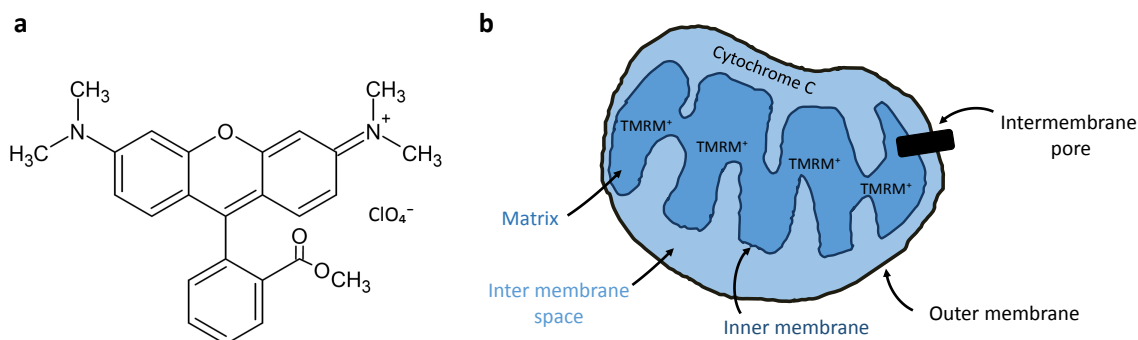


Figure 2.7: Tetramethylrhodamine (TMRM). a) Chemical structure of cationic TMRM. b) Accumulation of the TMRM⁺ fluorescence marker within the negatively charged mitochondria matrix.

The maximum in the absorptions spectra is 552 nm and the emission maximum is around 578 nm of the TMRM marker (Thermo Fisher Scientific). The lowest possible concentration of 10 nM was used, to avoid side effects such as phototoxicity and quenching effects, which were reported with a concentration from 50 nM on [47].

Active membranes in mitochondria of alive cells maintain a differential in electrical potential between the inner and the outer side of the mitochondria membrane, the so called membrane potential $\Delta\psi_M$. Under physiological conditions, the $\Delta\psi_M$ is between 120-180 mV and electronegative on the inter membrane side. TMRM is a cell-permeate membrane-potential sensitive dye, thus often used for live imaging, and is accumulating in functional negatively charged mitochondria (matrix) due to its positive charge (Figure 2.7b) driven by the $\Delta\psi_M$ and following the **Nernst equation** [48]. An insignificant amount of TMRM is also accumulating in the inter membrane space and the matrix spaces, but the volume of these spaces is negligible in relation to the volume of the matrix (and the outside of the mitochondria, where also some TMRM molecules stay) [48]. According to the Nernst equation, an increase of 61.5 mV in $\Delta\psi_M$ leads to a tenfold increase of monovalent cations in the matrix space [49].

$$\text{Membranepotential}(mV) = 61.5 \log_{10}(c_i/c_0)$$

with c_i as the concentration of cations inside the mitochondria and c_0 the concentrations of cations outside. Thus, usually a 100-1000 fold higher concentration of the TMRM marker can be found in the mitochondria (matrix) than in the cytosol [34, 49]. Hence, it shows a bright fluorescence signal in healthy mitochondria and is suitable for tracking the $\Delta\psi_M$. It is assumed that the accumulation of the dye also partly goes along with fluorescence quenching and a red shift, but the main part remains unquenched [48, 50].

Single-cell time traces showed a fluorescence decrease due to loss of mitochondria membrane potential, which was also previously described in [51]. MOMP is the result of the depolarisation of the mitochondria, whereby permeability transition pores

are opened, which is e.g. the case in the initiation phase of apoptosis. Thus, anions such as Cl^- , are released and also the concentration of TMRM inside the mitochondria (matrix) is decreasing. With the final MOMP, cytochrome *c* is released out of the inter membrane space, which is between the inner and the outer membrane, and triggers further apoptotic signaling [52].

In NP induced apoptosis, the TMRM intensity courses over time of single cells show a plateau phase after an increase in the beginning, which indicates a constant level of TMRM molecules accumulating in the mitochondrial matrix (Figure 2.8). The breakdown of the fluorescence signal, which is stated as t_{MOMP} , is assumed to go hand in hand with the opening of transition pores and the loss of the membrane potential and thus the release of the TMRM marker out of the mitochondria.

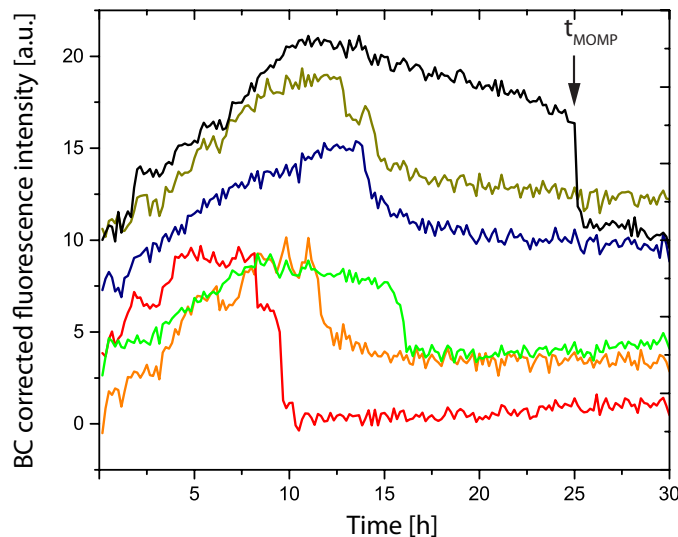


Figure 2.8: Exemplary 30 h single-cell time traces of the TMRM marker for the illustration of the mitochondria membrane permeabilization after apoptosis induction with $100 \mu\text{g mL}^{-1}$ PS-NH₂ nanoparticles in A549 cells.

The same breakdown is seen for combinatorial chemotherapeutic (etoposide, ps89 and in combination of both) induced apoptosis, although at later time points (Figure 2.9). And, it is important to mention, the first characteristic phase is different to the plateau phase in NP induced time traces. Here, we have a steep increase for the accumulation of the marker in the mitochondria, followed by a decrease in intensity, which can be more or less smooth. This drop in intensity is assumed to be correlated with the promptness of the depolarisation and the accompanying opening of the inter membrane pores of the mitochondria. The peak maximum, where the depolarisation is assumed to begin is indicated with $t_{\text{Depolarisation}}$. Further, the abrupt decrease of

fluorescence at later time points indicates the collapse of mitochondria membrane potential (t_{MOMP}). Both features were seen also recently in mouse cortical neurons after addition of a mitochondrial inhibitor [53]. The distinct peak, which is seen for chemostatic treated cells, was not observed for NP treated cells. Further, the NP induced apoptotic time traces are more noisy than in combinatorial chemotherapy since NPs show autofluorescence.

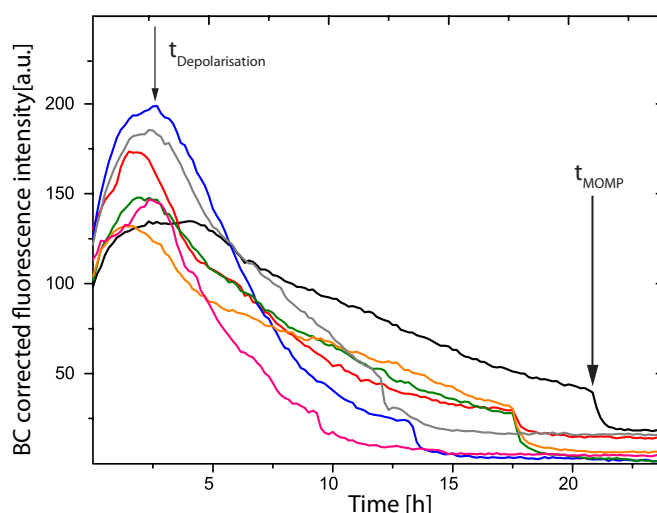


Figure 2.9: Exemplary 24 h time traces of the TMRM marker for mitochondria membrane permeabilization after apoptosis induction with the combination of 10 μM Etoposide and 25 μM PS89 in A549 cells. The distinct peak maximum ($t_{\text{Depolarisation}}$) and the subsequent decay at the beginning of the time trace is assumed to correlate with the depolarisation of the mitochondria. The event time of MOMP (t_{MOMP}) is also indicated with an arrow.

2.4.3 Reactive Oxygen Species Indicating Cellular Stress - CellROX

Reactive oxygen species (ROS) are important key players in many diverse apoptosis signaling cascades [54]. The involvement in different apoptosis pathways is discussed in Chapter 3.1. More general information about ROS as cellular stress indicator is given in Chapter 3.5.

To monitor ROS production, several fluorescence dyes are used in literature. $\text{H}_2\text{DCF-DA}$, the diacetate (DA) form of H_2DCF (2-7-dichlorodihydrofluorescein) is a cell-permeable marker, which allows the intracellular accumulation of the non-fluorescent H_2DCF . If oxidized by non-specific ROS, the fluorescent product, 2-7-dichlorofluorescein (DCF), shows bright fluorescence. But this widely used marker should not be used, due to its photo-oxidation and photo-bleaching. Additionally, this marker is

also catalyzed by cytochrome *c* (which is released from mitochondria during apoptosis), and, even worse, creates ROS by itself [55]. Also the prominent dihydroethidium (DHE) marker has several interferences, which are not suitable for multiplex time-lapse experiments in single-cells [55].

Therefore, for this study, the CellROX ROS detection reagents from Molecular Probes were chosen due to their photostability, ease use in complete growth media and their broad variability (available in three different colors). Moreover, they are suitable for multiplexing fluorescent probes, which is for example not possible with oxidized DHE due to its broad emission spectra. For the multicolor compatibility we used the CellROX green, the CellROX orange or the CellROX red dye, whichever the other used markers were combined, with a final concentration of 100 nM. However, the chemical structure of the fluorogenic probes are corporate secret and the exact mode of action is not revealed exactly. But, all three ROS detection agents respond to hydrogen peroxide, peroxyxynitrite, nitric oxide, tert-butyl hydroperoxide and hypochlorite anions and especially to hydroxyl radicals and superoxide anions. CellROX reagents are weakly or non-fluorescent in a reduced state and show bright fluorescence upon oxidation. The CellROX green reagent has an absorptions- and emission maxima at 485 and 520 nm and is a DNA binding dye when oxidized, so mostly localized in the nucleus and mitochondria. The CellROX Deep Red and the CellROX orange reagents are localized in the cytoplasm and have absorptions- and emission maxima at 644 nm and 665 nm or 545 and 565 nm.

All three reagents have the same characteristic phenomenological time course in principal, dependent on the exposure and the cell line. Exemplary single-cell time traces of CellROX after apoptosis induction with 10 μM ETO and 25 μM PS89 in A549 cells are shown in Figure 2.10. The increase of the fluorescence intensity, thus the slope, is assumed to correlate with the amount of ROS, accordingly the production rate of ROS and the stress level of the cell. After the increase, a sharp drop in intensity is detected. The breakdown of the fluorescence is termed t_{OxBurst} and presumably correlates with the oxidative burst caused by the destruction of the marker by an excess of produced radicals. The time courses are fitted with the same phenomenological mathematical functions as the LysoTracker. From these fits, the event times of the oxidative burst (t_{OxBurst}) are extracted.

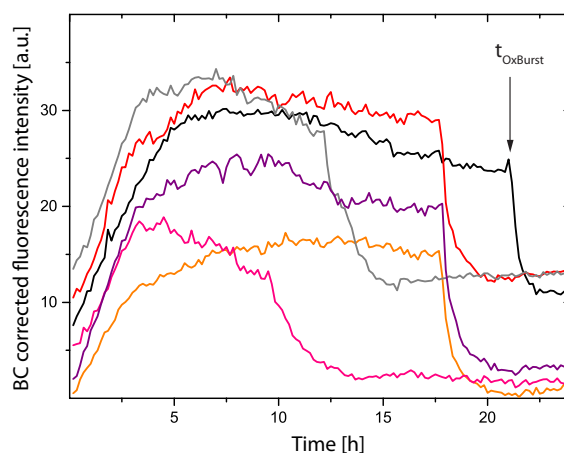


Figure 2.10: Exemplary 24 h time traces of CellROX ROS detection agent in combinatorial chemotherapy induced apoptosis. A549 cells were exposed to 10 μM etoposide and 25 μM ps89.

The typical time courses of the CellROX reagent for etoposide, PS89, the combination of both of them, STS and NP (Figure 2.11a) induced apoptosis in A549 cells show the initial slope and the sharp drop in fluorescence as described above. But in some cases, a very narrow peak in the beginning of the measurement after exposure to NP is seen (Figure 2.11b). This early change in intensity illustrates a fast response of the cells to the treatment. The higher susceptibility of the cells could be caused by the cell passage (assumed for higher passages) or the quality of the NPs (less agglomerates, thus faster engulfment).

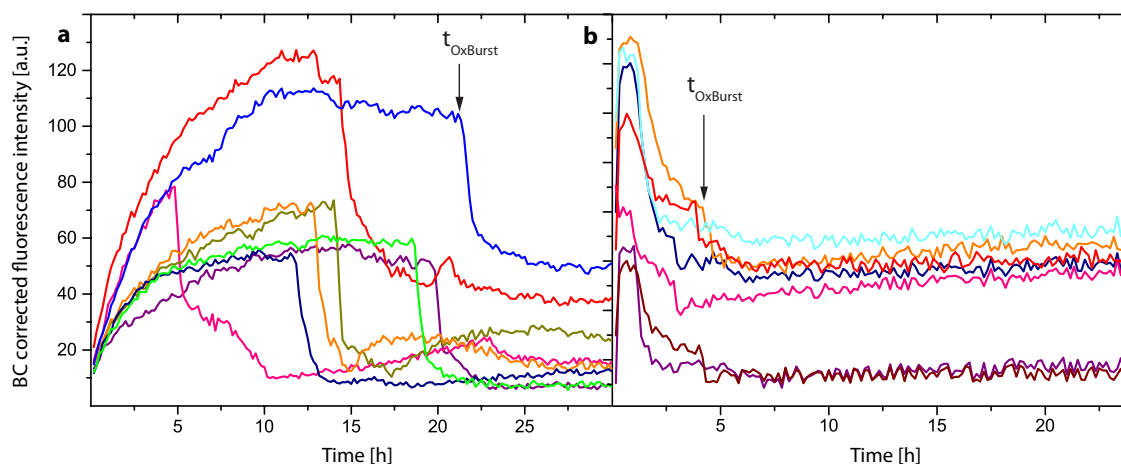


Figure 2.11: Exemplary time traces of CellROX ROS detection agent after exposure to 2 μM staurosporine (a) and apoptosis induced with 100 $\mu\text{g mL}^{-1}$ PS-NH₂ nanoparticles (b), both in A549 cells. Most time traces of NP and STS induced have the characteristic course of the left graph, but in some cases they show a fast-pasted response to the apoptosis trigger with a narrow peak (b).

2.4.4 Calcium Release out of the Endoplasmatic Reticulum - Calbryte

Calcium release is a result of endoplasmatic reticulum (ER) stress, and one of the main trigger in combinatorial chemotherapy of etoposide and the sensitizer PS89 induced apoptosis signaling pathways [42].

Calcium markers are usually acetoxymethylester (AM), which are non-fluorescent, but once hydrolyzed by (intracellular) esterases, they are converted into a activate state. Upon binding calcium ions, the marker shows bright fluorescence [56].

Usually, the fluorescence markers are added in combination with the apoptosis inducer at the same time and stay there for the whole experiment in a very low concentration. However, this approach did not work for the calcium marker. In our case, time-lapse measurements last for 24-30 h, which makes the use of FBS necessary to avoid side effects like starving of the cells. But FBS contents also esterases, which leads to cleavage of the fluorescence marker already outside of the cell, thus leading to a broad and diffuse signal outside and inside of the cell. This makes an incubation step inevitably, and preferably under serum-free conditions. Thus, the impact on the signal of FBS and the serum substitute Panexin NTA (PAN Biotech), which has defined components and is suitable for adherent cells, was tested in different concentrations (10%, 5% and 1%; (v/v)). In summary, the signal at the beginning was much better for NTA than for FBS, and the lower the NTA amount, the better was the signal during the first hours. But for all conditions, the signal disappeared after 24 h. The first reason for this is, that also NTA contents some esterases. Secondly, the widely used markers Cal-520 AM (AAT Bioquest) or Cal-590 AM (AAT Bioquest) show no retention inside the cells. The reason for the lacking retention could be that some cell lines, presumably also A549 cells, express organic anion transporter membrane proteins, which transport the marker from the inside to the outside of the cell. The use of probenecid, which could prevent the leaking of the cell-loaded dye out of the cells, should be avoided, since it has various effects on signaling pathways. Thus, the new Calbryte-520 and Calbryte-590 (AAT Bioquest) markers are used, which are developed for higher retention once inside the cells. According to the manufacturer, the indicator is a polar molecule in the active state and trapped inside the cells thus unable to diffuse through the cell membrane. The best results with a minimum but sufficient loading time, without affecting the cells too much, were gained with an incubation of Calbryte-520 (1 μ M) for 30 min in Hank's Buffer with 20 mM HEPES (HHBS). Note the low amount of HEPES, since HEPES in higher concentrations was seen to induce cytotoxicity upon light exposure.

The single-wavelength calcium indicator used here, is only for the detection of relative changes in the calcium concentration. The loading of the single cells can be different, thus a quantitative analysis of the calcium level per cell would require a single-cell calibration beforehand. The time courses of A549 cells after inducing apoptosis with

etoposide or PS89 show mostly in the very beginning a decrease in intensity, which is assumed to be bleached autofluorescence (Figure 2.12). Furthermore, very sharp onsets in the fluorescence signal and a very sharp signal decrease is observed to be characteristic for calcium time traces. The onset is correlated with the efflux of the calcium ions out of the stressed ER into the cytosol ($t_{\text{Calcium Release}}$) and binding to the marker molecules, which are predominantly localized in the cytosol. The drop in signal is rather not photobleaching as described in [57], but caused by the release of the marker out of the cell due to PMP, as seen in the analysis of the raw data. In literature, this typical peaks are called Ca^{2+} puffs or Ca^{2+} sparks [56, 58]. In some cases, also very broad peaks, plateaus, double peaks or a smooth decrease of signal are observed. In most traces, this does not affect the detection of the event times.

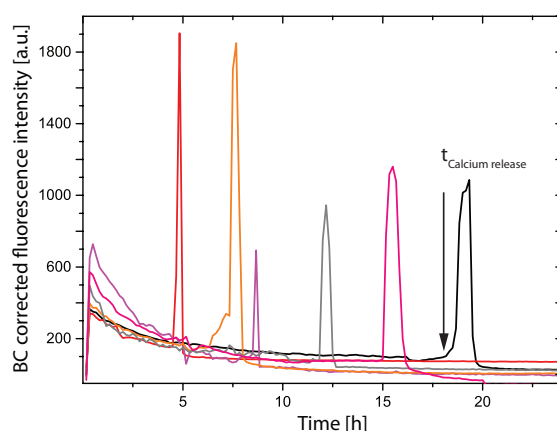


Figure 2.12: Exemplary 24 h time traces of Calbryte-520 after apoptosis induction with the combination of 10 μM Etoposide and 25 μM PS89 in A549 cells. The time point of calcium release out of the endoplasmatic reticulum ($t_{\text{Calcium Release}}$) is indicated with an arrow.

2.4.5 Caspase-3/7 Activation - CellEvent Caspase Marker

Most of the apoptotic signaling cascades are caspase-dependent, also the PS-NH₂ nanoparticle induced apoptosis pathways as described in Chapter 3.1.1.

Thus, to illustrate the activation of caspase-3 and -7, which is stated as the first event in the late phase of apoptosis, the CellEvent green Caspase marker (Invitrogen) was used. It was administered in a very low concentration (3%, (v/v)), since the marker stays in the cell media during the whole measurement without any washing step.

The fluorogenic reagent is a nucleic acid binding dye with a four amino acid peptide sequence (DEVD). The fluorophore is cell-permeant and non-fluorescent until the DEVD binding side is cleaved by activated caspase-3 or caspase-7. Once the cleavage is implemented, the dye binds to DNA and produces a bright fluorescence signal (Figure 2.13).

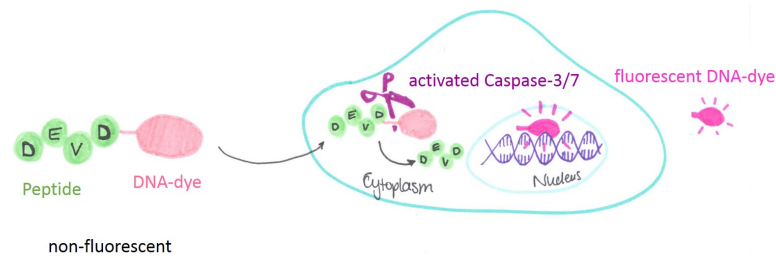


Figure 2.13: Mode of action of CellEvent green marker. The cell permeant DNA dye CellEvent green is non-fluorescent as the conjugated DEVD amino acid peptide inhibits the binding to nucleic acids. As soon as caspase-3 or caspase-7 are activated during apoptosis, the DEVD sequence is cleaved and a bright fluorescence signal results from the binding to DNA.

Exemplary time courses of caspase-3/7 activation during PS-NH₂ nanoparticle induced apoptosis can be seen in Figure 2.14. There, the activation (cleavage of the marker) can be seen as a sharp onset signal in the time courses ($t_{\text{CASP-3}}$) and is followed by a less abrupt decrease in fluorescence, caused by photobleaching. The onset of fluorescence is assumed to be delayed due to the enzymatic reaction. The fitting of the time traces for the late markers are described in Chapter 2.5.

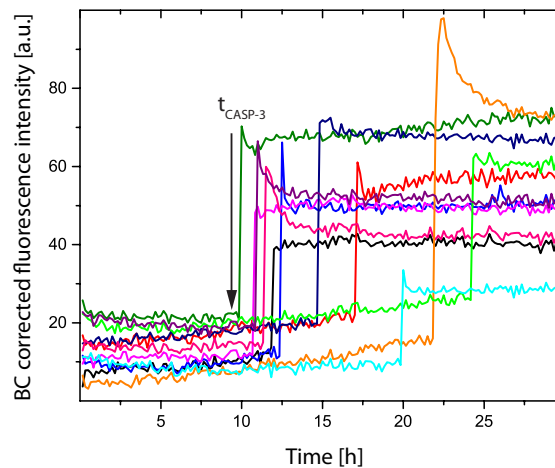


Figure 2.14: Exemplary 24 h time traces of CellEvent green to illustrate the activation of caspases-3 and-7 after apoptosis induction with 100 $\mu\text{g mL}^{-1}$ PS-NH₂ nanoparticles in A549 cells. The activation of caspase-3 and -7 ($t_{\text{CASP-3}}$) is indicated with an arrow.

2.4.6 Phosphatidylserine Flip to the Outer Membrane - pSIVA-IANBD

The second late event of PS-NH₂ nanoparticle induced apoptosis, which was analyzed in this study, is the phosphatidylserine (PhS) flip from the inner side of the plasma membrane to the outer side of the membrane. The membrane lipid PhS is mainly on the inner leaflet of the plasma membrane in viable cells, thus not accessible for the cysteine pSIVA-IANBD fluorophore, which is non-fluorescent at this stage. As soon as the cell is undergoing apoptosis, PhS is flipping to the outer leaflet and the polarity sensitive fluorophore can bind to the lipid (Figure 2.15). The excitation maximum of pSIVA is at 488 nm and the emission maximum at 530 nm. The pSIVA marker was used in a concentration of 3% (v/v) without any further washing step.

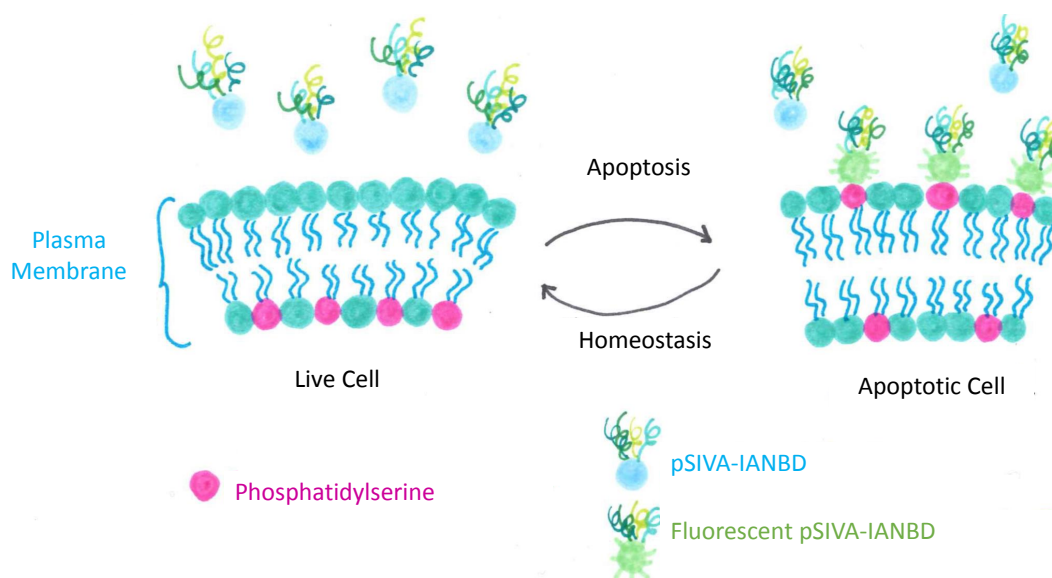


Figure 2.15: Mode of action of the pSIVA-IANBD marker. In live cells, phosphatidylserine (pink) is mostly on the inner leaflet of the plasma membrane. During apoptosis, the polar membrane lipid flips to the outer leaflet of the membrane and the pSIVA-IANBD marker can bind, which is leading to a bright fluorescence signal.

In single-cell time-lapse measurements, the translocation of the polar membrane lipid PhS on the non-polar lipid environment and the subsequent binding of the marker causes a sharp onset of fluorescence, indicated as $t_{\text{PhS-Flip}}$ (Figure 2.16). This translocation is reversible. The fluorescence decreases after the sharp maximum due to photobleaching.

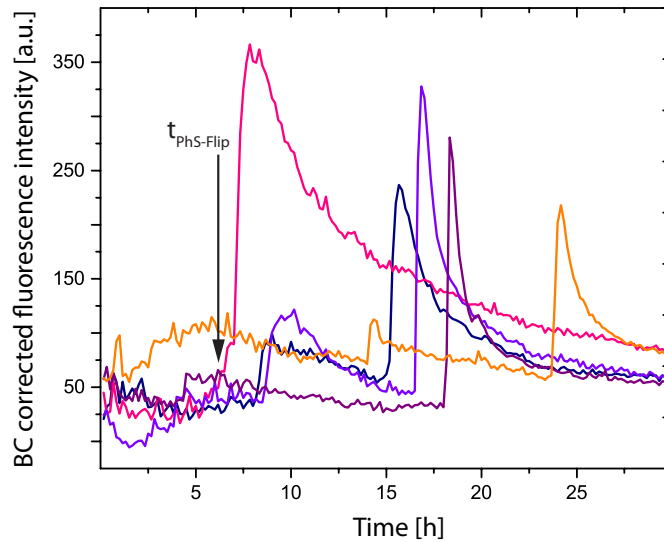


Figure 2.16: Exemplary 30 h time traces of pSIVA-IANBD showing the flip of the membrane lipid phosphatidylserine from the inner leaflet of the plasma membrane to the outer leaflet ($t_{\text{PhS-Flip}}$) after apoptosis induction with 2 μM staurosporine in A549 cells.

2.4.7 Plasma Membrane Permeabilization - Toto-3-/Propidium Iodide

The final stage of apoptosis includes the permeabilization of the plasma membrane. In this phase, cell-impermeant dyes such as Toto-3 and Propidium Iodide can enter the cell and bind or intercalate to the DNA (Figure 2.17).

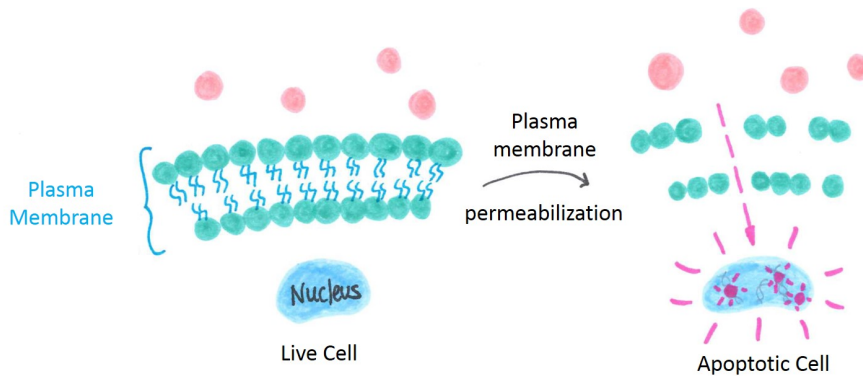


Figure 2.17: Propidium Iodide (PI) and Toto-3 Iodide (Toto-3) are both intrinsically non-fluorescent dyes, which are not cell-permeable. At the late phase of apoptosis, the plasma membrane is permeabilized and the reporter molecules can enter the cell. There, a bright fluorescence signal arises due to intercalation with DNA (PI) or external binding/bis-intercalation (Toto-3).

Toto-3 iodide (Invitrogen), a carbocyanine dimer, has several modes of action: it can externally bind, intercalate or bis-intercalate with either single-stranded or double-stranded DNA [59]. It has its excitation maximum at 542 nm and the emission maximum at 660 nm (Figure 2.18). Within this study, Toto-3 iodide was used with in a concentration of 1 μ M.

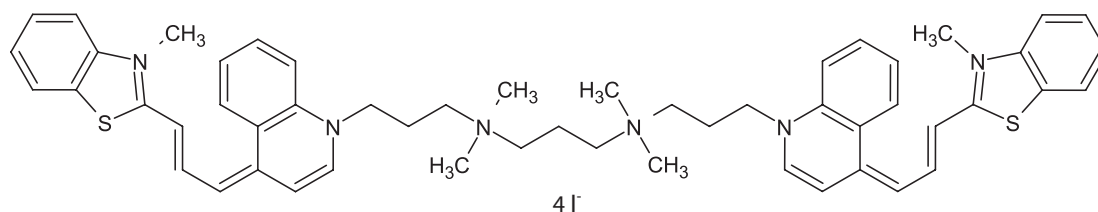


Figure 2.18: Chemical structure of DNA binding marker Toto-3 iodide.

Propidium Iodide is intercalating between the bases of DNA with a stoichiometry of 4-5 base pairs to one dye molecule. It also binds unspecifically to RNA. The excitation spectra shows a maximum at 535 nm and the emission spectra at 617 nm. Propidium Iodide (Imgenex) was used at a concentration of 1% (v/v). The chemical structure of PI is shown in Figure 2.19.

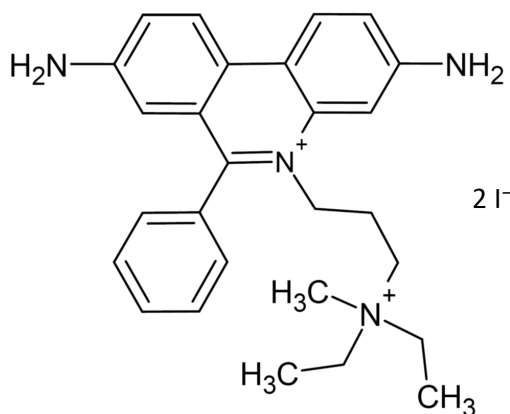


Figure 2.19: Chemical structure of intercalating cell death marker Propidium Iodide.

Exemplary time courses of the PI marker of A549 cells after exposure of 100 μ g mL⁻¹ PS-NH₂ nanoparticles show significant enhancement of fluorescence when reacting with DNA after PMP (t_{PMP}) and a slight and smooth decrease afterwards, which can be related to photobleaching (Figure 2.20). These features are also characteristic for Toto-3 Iodide.

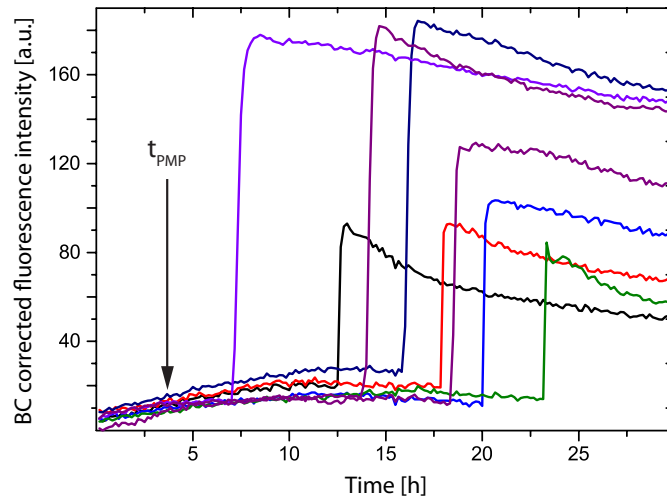


Figure 2.20: Exemplary 30 h time traces of Propidium Iodide to illustrate the plasma membrane permeabilization (t_{PMP}) after apoptosis induction with $100 \mu\text{g mL}^{-1}$ PS-NH₂ nanoparticles in A549 cells. The event PMP is indicated with an arrow.

2.5 Data Analysis

2.5.1 Maximum-likelihood Fitting and Extraction of Parameters

The single-cell time traces are saved as .csv files and are converted into .txt files using an in-house written Matlab macro (Peter Röttgermann). Therefore, a meta data excel file, which includes the experiment date, measured channels, used markers and status (signal yes or no) information, is needed.

Maximum-likelihood Estimation

The event times were extracted with the help of the so called Phenomenological Event Time Identification (PETI) analysis, which was custom written in Matlab by Daniel Wosché. The maximum-likelihood method was utilized to fit phenomenological functions to the fluorescence time traces to extract the event times of the fluorescent markers. The marker-dependent model functions characterize the time courses of the fluorescence markers. The markers were separated in two classes due to their characteristic behavior, the early phase apoptosis and the late phase markers. For both classes, the earliest time point of a change in the time course was chosen to be extracted as event time.

The time courses of the markers for the early phase of apoptosis show an increase in intensity which is described by a parabola (Figure 2.21). Further, a transition to

a constant level via a more or less steep decrease is observed. The model function $f_{\text{early}(t)}$ to reflect the time courses is

$$f_{\text{early}(t)} = \sigma(t)(a_{\text{const}} + s \cdot a_{\text{quad}} \cdot (t_{\text{vertex}} - t)^2) + (1 - \sigma(t)) \cdot b,$$

with the sigmoid function $\sigma(t)$

$$\sigma(t) = \frac{1}{1 + e^{-\gamma(t_{\text{step}} - t)}}$$

where the first summand describes the parabola and the second the transition to the constant level. The fit parameters a_{const} (constant ordinate offset), s (opening of parabola), a_{quad} (quadratic coefficient), t_{vertex} (vertex of the parabola), b (final saturation value), t_{step} (point of fluorescence breakdown) and γ (steepness) enable a well fit of the functions to the measured time traces [60].

In the following, exemplary single time traces are shown for the LysoTracker (a), the TMRM marker (b), the CellROX (c), and the Calbryte-520 marker (d) with the final fits (red lines) to extract the event time (vertical black dashed line) respectively. The dashed green line indicates the parabola and the green lines the asymptotes. For best fits, the event times are extracted or the time traces were discarded, if no event times could be identified. The noise is depicted as red dashed line.

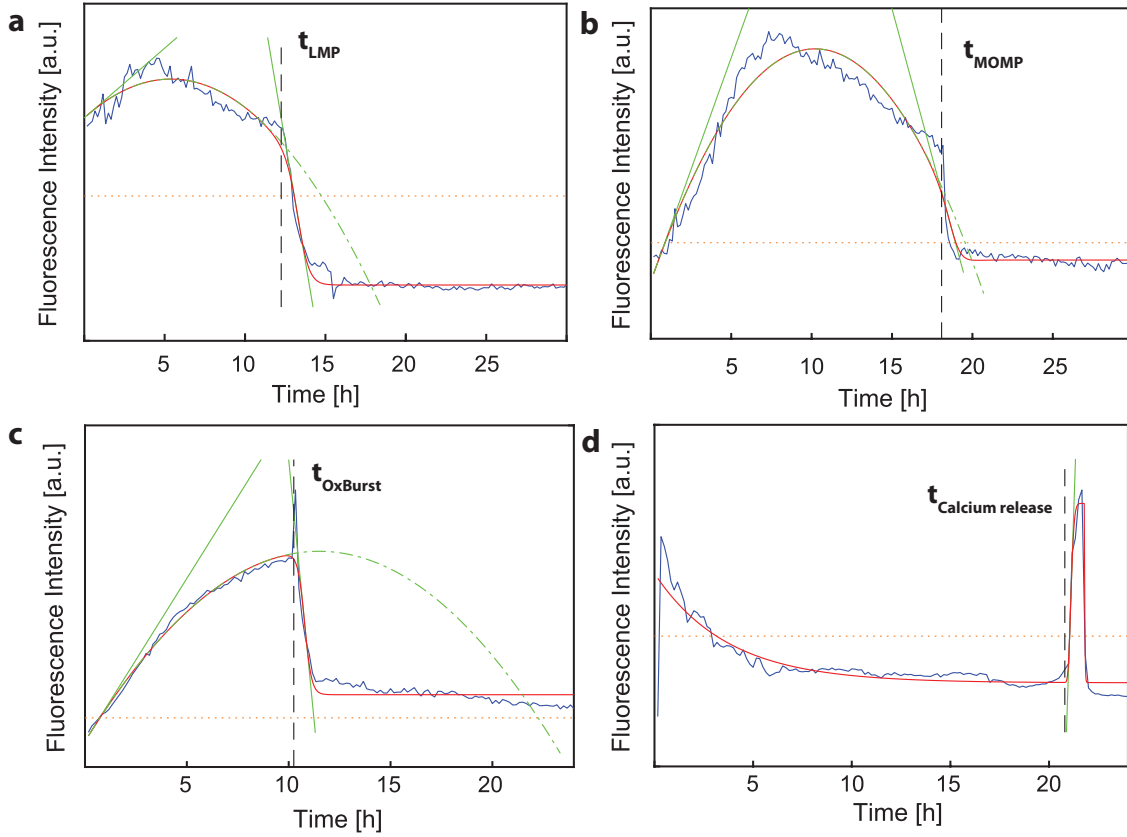


Figure 2.21: Time traces of early markers (blue) (a) LysoTracker, (b) TMRM, (c) CellROX, and (d) Calbryte-520 were fitted with mathematical functions. The indicated event times (vertical black dashed line) were extracted with the help of mathematical functions such as a parabola (dashed green line) and tangents (green lines). The final fit is shown as red line and the noise as a horizontal red dashed line.

For the late markers CellEvent green, pSIVA-IANBD and the PI/Toto-3 Iodide, a step increase in intensity follows a constant level (Figure 2.22). A more or less steep decrease, depending if the marker photobleaches or not, subsequents. The function f_{late} reconstructs the time traces

$$f_{\text{late}} = A + B \cdot \sigma(t) \cdot (b + e^{\gamma(t_{\text{step}} - t)}),$$

With

$$\sigma(t) = \frac{1}{1 + e^{-\alpha(t_{\text{step}} - t)}}$$

where α is the fit parameter steepness.

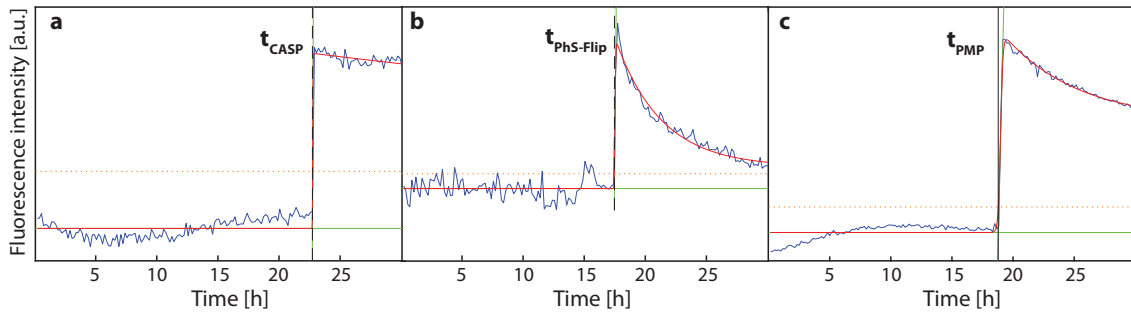


Figure 2.22: Time traces of late markers (blue): a) CellEvent green Caspase marker b) pSIVA-IANBD c) PI/Toto-3 Iodide were fitted with mathematical functions. Ascent tangents (green lines) were used to extract the indicated event times (vertical black dashed line). In red, the final fit is shown and the noise as a horizontal red dashed line.

The parameter event time, which is for the early markers $t_{\text{breakdown}}$ and for the late markers t_{onset} , as well as the ROS rate (slope of the increase in CellROX time traces), are then extracted from the fitted traces.

See further details in the Supplementary Information of Murschhauser et al. [36] or [60].

2.5.2 Interactive Fitting

For the data of the combinatorial chemotherapy, described in Chapter 4, an interactive fitting routine was designed. The need for the development was seen as the time traces of cells, which were treated with ETO, PS89 or the combination of both, showed new features (discussed in Chapter 2.4), and more variations between the traces within one marker were observed. Also the signal-to-noise ratio was slightly worse than for the NP induced apoptosis time traces. To ensure high quality results, which are guaranteed with accurate and precise extraction of the event times as well as the prevention of false negative and false positive outcomes, an user interface was operated to allow a manual correction for the fits. In short, since the so far developed mathematical functions can not reference the actual time traces, a manual interaction after the first rough fit is requested. Either, the event time can be directly changed manually and accepted afterwards. Or, the fittings parameters, such as the parabola or the exponential decay, can be adjusted as well as the fitting range of the time course can be minimized to allow a more precise fit. After these changes, the fitting routine is initialized again. The new fit can be accepted or changed once more.

2.5.3 Principal Component and Cluster Analysis

The plots with event or delay times were generated with custom written Matlab or Python macros (Daniel Woschée). The distribution of event times are visualized in one-dimensional histograms for each marker. The correlations between two measured fluorescence markers are presented in two-dimensional scatter plots. The position of the clusters were identified by mean shift clustering using a kernel density estimation. The clusters were illustrated by ellipses with asymmetric major semi-axes in order to consider anisotropic data scattering. The width and orientation of the clusters, which are determined Principal Component Analysis (PCA), indicate the strength of the correlations. The length of the major semi-axis shows the scattering of the events. The longer the axis is, the larger is the variance in scattering. Further, the minor semi-axis indicates the correlation of the events. Thus, the shorter this axis, the stronger is the correlation between the two events. The orientation of the ellipse and the major semi-axis in relation to the diagonal shows the time-dependence of delay time. If the cluster, and thus the major axis is parallel to the diagonal, no time dependence is detected, while the delay time increases or decreases with time, if no parallelization is shown. To account the time delay between apoptotic inducer administration and the start of the time-lapse, the time offset was added to the time traces. More details of the determination of clusters and ellipses can be found in the Supplementary Information of Murschhauser et al. [36]. All the used macros for analyzing and plotting the data are available with the following doi:10.5281/zenodo.1418465. For an overview, the workflow of data processing can be seen in Figure 2.23.

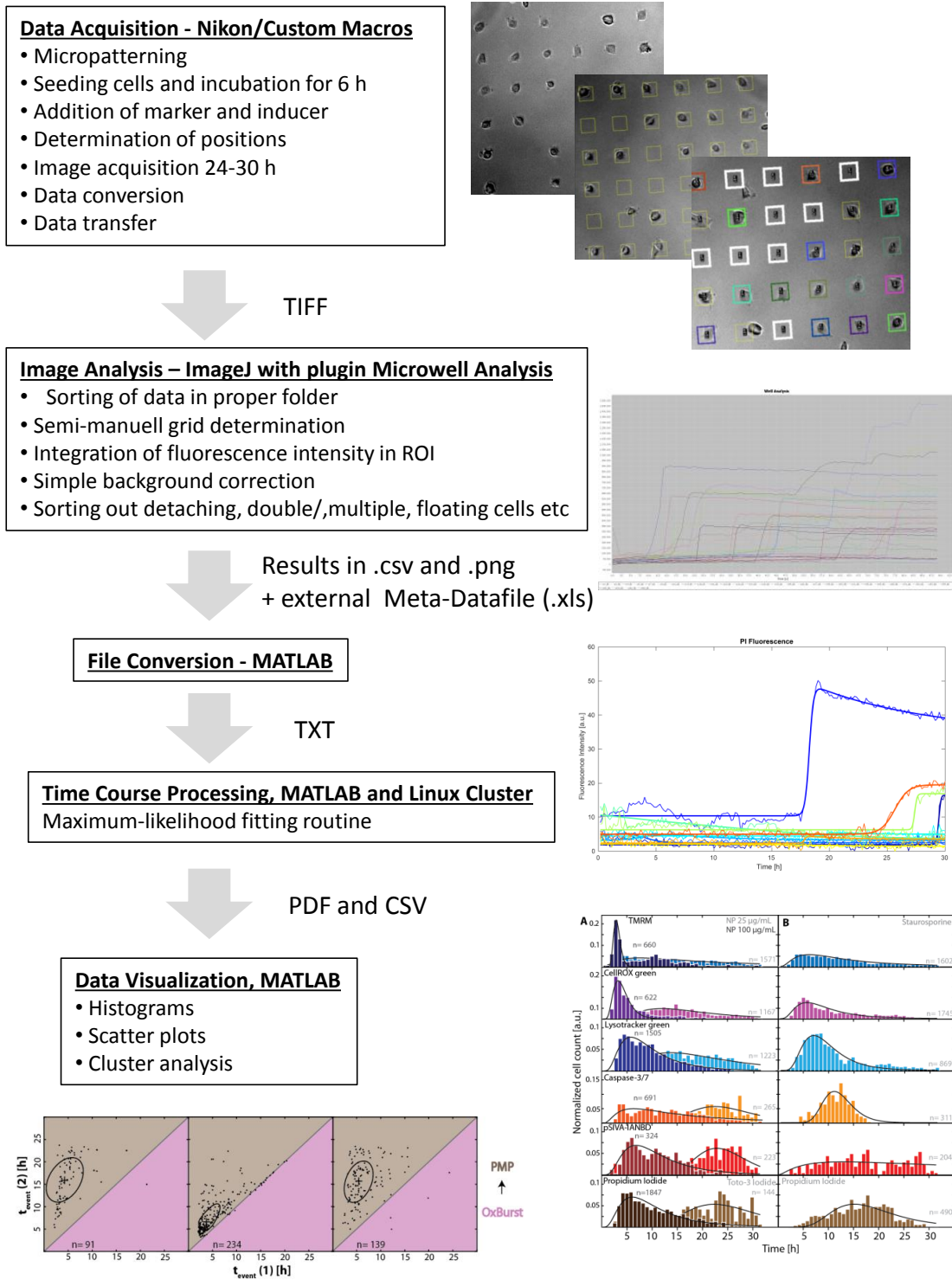


Figure 2.23: The present status of the workflow of data acquisition and data analysis.

Chapter 3

Event-Time Correlations in NP induced Apoptosis

3.1 State of the Art

Apoptotic signaling pathways are arbitrarily complex depending on the type, the concentration and the exposure time of the apoptosis inducer, the used cell line and experimental conditions (bulk or single-cell). Furthermore, especially the impact of nanomaterials, such as nanoparticles, varies a lot. It depends on core material, size, shape, coating, concentration, charge, stability in different solutions, method of production, purification grade as well as the experimental conditions such as pH, temperature and storage conditions. Particles in nanometer size gain new properties due to the increased ratio of volume to surface area, which leads to higher surface energy, compared to bigger bulk particles. Therefore, a nanoscaled material is not only more reactive, but also develops new chemical, magnetical, mechanical and optical properties. These interesting features have raised the common interest tremendously and the field of nanotechnology grew exponentially in production and application in the 21st century [61–63]. Besides all the positive benefits of such nanomaterials, also the risk and the impact on the environment and the human body have to be considered and characterized in a systematic and an exhaustive way. In the last decades various studies have characterized the effect of the above-mentioned properties under various conditions, see reviews [64–66]. Still, the underlying mechanisms and the induced signaling pathways of many nanomaterials are poorly understood.

In the following, different pathways are described. First, the PS-NH₂ nanoparticle induced apoptotic pathway, which was the main focus in this study. Further, the staurosporine (STS) triggered pathway, since STS was used as a positive control to compare with the NP pathway. And lastly, an external apoptosis pathway, the Fas-Ligand signaling cascade, is presented.

3.1.1 Signaling Pathways Induced by PS-NH₂ Nanoparticles

The focus of this short literature overview will be on apoptosis signaling cascades induced by PS-NH₂ nanoparticles (58 nm). The physico-chemical properties of PS-

NH₂ nanoparticles are well characterized as well as their trigger of apoptosis in cell culture [18, 41, 62, 67–71]. Thus, they were chosen as model particles to study the apoptotic signaling pathways with time-lapse measurements at the single-cell level. The A549 lung cancer cell line was selected, since it is frequently used in cytotoxicity studies of nanomaterials to mimic inhalation scenarios.

Cationic PS-NH₂ nanoparticles are known to induce cytotoxicity by apoptosis pathways [21, 41, 62, 67–70]. The toxicity is not due to the material per se, but due to the coating with -NH₂ groups. The effect was determined by comparison of different coated and non-coated polystyrene particles [67].

In the initiation phase, the particle up-take occurs actively via energy-dependent endocytosis. Once inside the cell, the particles accumulate in the lysosomes [41, 70, 72–74] (Figure 3.1). Inside the acidic lysosomes, some of the polycations get protonated (high proton binding affinity), which leads to a pH increase (alkalization), the amount of protons drops (buffering) and thus the cell is pumping actively protons inside the lumen to compensate this loss [62, 70]. To preserve the electrochemical and osmotic gradient, a subsequent water and ion (Cl⁻) flux inside the lysosomes is executed. The consequential osmotic swelling of the lysosomes causes the final lysosomal breakdown. During this lysosomal membrane breakdown (LMP), the membrane is first permeabilized until it ruptures and the lysosomal content, e.g. cathepsin-D, is released. The whole procedure is called the "proton sponge theory" [75] and is well described in [66]. Further, in the PS-NH₂ nanoparticles induced apoptosis signaling cascade the mitochondria are involved, observed in different cell lines [41, 62, 67, 69, 70]. Through the activation of the mitochondria, mitochondrial reactive oxygen species (ROS) are released and/or due to the mitochondria outer membrane permeabilization (MOMP), mitochondria content, e.g., cytochrome c, is streaming into the cytosol. Additional ROS is produced due to MOMP and/or LMP and also substantially involved in the downstream signaling [41, 69]. Wang et al. as well as Anguissola et al. proposed the sequence of LMP-MOMP [67, 69]. Further, in a more detailed study Wang et al. and also the group of Brunk, suggested the pathway LMP-MOMP-ROS [70, 76]. Furthermore, the group of Baumgartner et al. found additionally the event sequence MOMP-ROS-LMP, suggesting two potential pathways [77]. In summary, all findings come to terms that positive feedback loops, e.g., ROS-LMP-mitochondrial ROS-LMP, can not be excluded and crosstalk between the key player is highly probable. Thus, the involved key players are identified, but the timing of the events is still unclear.

After the initiation phase of apoptosis, the execution phase of apoptosis is provoked. In this final stage, caspases, especially caspase-9 through MOMP, as well as the effector caspases 3 and 7 are activated [41, 62, 67, 69, 70]. Next, the membrane lipid phosphatidylserine is flipping from the inside of the cell to the outer side of the membrane (PhS-Flip) [21]. Finally, the plasma membrane is permeabilized (PMP) and the cells are dying due to DNA damage [67].

Note that the detailed signaling pathways described above are only valid for cationic PS-NH₂ nanoparticles with a size of around 58 nm, observed in different cell lines. For other apoptosis inducers, various, more or less key players can be involved, also in a different sequence. Furthermore, the described cascade is only valid when the nanoparticles are added in combination with serum to the cells. In this case, the serum proteins and different molecules form the protein corona on the surface of the NP, the nanoparticles with this corona are endocytosed and accumulated in the lysosomes [71]. There, the corona is degraded. In contrast, in serum-free conditions the positive charge is not screened and thus leads within a short time directly to plasma membrane permeabilization and without initiating the various signaling pathways [69].

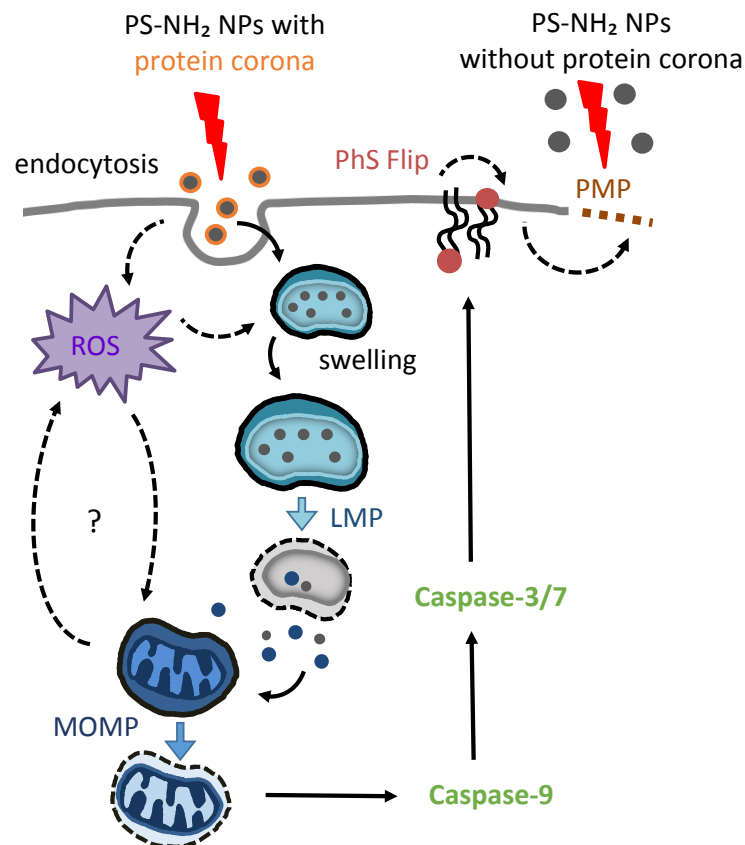


Figure 3.1: Overview of the apoptosis signaling cascade induced by 58 nm sized cationic amino-modified polystyrene (PS-NH₂) nanoparticles (NPs) coated with media proteins. ROS= reactive oxygen species; LMP=lysosomal membrane permeabilization, MOMP= mitochondria outer membrane permeabilization; PhS-Flip= Flip of phosphatidylserine from the inner side of the plasma membrane to the outer membrane side; PMP= plasma membrane permeabilization.

3.1.2 Staurosporine Induced Cell Death Pathways

Since many years, the bacterial alkaloid staurosporine (STS) is known for inducing cell death and is frequently used in apoptosis studies as a model inducer for analyzing signaling pathways [78–82]. Therefore, the broad-spectrum protein kinase inhibitor STS is used as a positive control for cell death in this study. Further, it is suited best as a positive control, since the pathways of STS induced apoptosis are very similar to the ones described above for PS-NH₂ nanoparticles. In the following paragraph, the known STS signaling cascades from literature are described in short.

In the early phase of apoptosis, the first point of action are the lysosomes. Johansson et al. showed in human foreskin fibroblasts that the inhibition of cathepsin D, which is released from ruptured lysosomes, also inhibits the release of cytochrome c [80]. Cytochrome c is usually set free out of the mitochondria, when the mitochondria outer membrane is permeabilized. Subsequently, a reduced caspase activity and thus a delayed cell death was detected in response to the inhibition [80]. Hence, in summary, the pathway is roughly the same as for NPs: LMP-MOMP-CASP-PMP. Also ROS and the calcium release seem to play a role in staurosporine-induced apoptosis [79]. Additionally, as a stage in between, the formation of the so called apoptosome was found to be an important step. When ATP binds to cytochrome c, the assembly of the apoptosome is realized with the composition of pro-caspase-9 and the apoptosis protein-activating factor-1 (Apaf-1) [80]. This formation of the apoptosome was not reported for PS-NH₂ NP induced apoptosis yet. Manns et al. also found an apoptosome independent pathway [78]. By the apoptosome, caspase-3 is activated via pro-caspase-3 and caspase-9. Also caspase-independent pathways were found for STS [80, 81].

3.1.3 Comparison to an External Apoptosis Trigger: the Fas-Ligand

Besides the intrinsic mitochondrial ROS induced apoptosis, also an extrinsic pathway, mediated by death receptors, exists. The binding of a ligand to the receptor initiates protein-protein interactions in the cell membrane and initiator-caspases are activated. The so called tumor necrosis factor (TNF) receptor superfamily of cytokines includes the death receptor activating ligands TNF α , the TNF-related apoptosis-inducing ligand (TRAIL) as well as the Fas-Ligand (FasL) [83, 84]. The FasL is expressed among others on tumor epithelium and can be membrane bound (mFasL, apoptotic) or soluble (sFasL), which has no apoptotic effects [85]. The Fas receptor is one of the major known receptors, also prominent as cluster of differentiation 95 (CD95) or apoptosis antigen 1 (APO-1). The Fas receptor is a 36 kDa transmembrane receptor [86], which is a pre-associated homotrimer [87]. Due to the binding of the Fas-Ligand, the receptor trimerizes via cross-linked disulfide bind-

ings. An overview of the FasL induced signaling pathways is shown in Figure 3.2. The clustering of FasL and the receptor is necessary for the receptors stabilization and activation [88]. Minutes after binding of the Fas-Ligand to the receptor, the Fas-Associated protein with Death Domain (FADD) and procaspase-8 are activated and the formation of Fas/FADD/caspase-8, the so called death-inducing signaling complex (DISC), is initiated [89]. If additional FADD and caspase-8 are recruited, resulting from the accumulation of released endosomal DISC in the cytosol, type I of the FasL induced apoptosis pathway is triggered [90–92] (Figure 3.2, left). In this pathway, caspase-3 is directly activated and the chromosomal DNA is degraded, which leads to apoptosis [93, 94]. However, with less activated caspase-8 and FADD, thus a low level of DISC formation, the caspase-3 activation is only possible with an amplification of caspase-8 through a loop in the mitochondria [92, 95, 96] (Figure 3.2, right). This alternative is the so called mitochondria dependent pathway type II, where the cleavage of Bid leads to the proapoptotic activation of the mitochondria and thus the release of cytochrome C. The apoptosome is formed and thereon caspase-9 triggers the executioner caspase-3 leading to apoptosis [92].

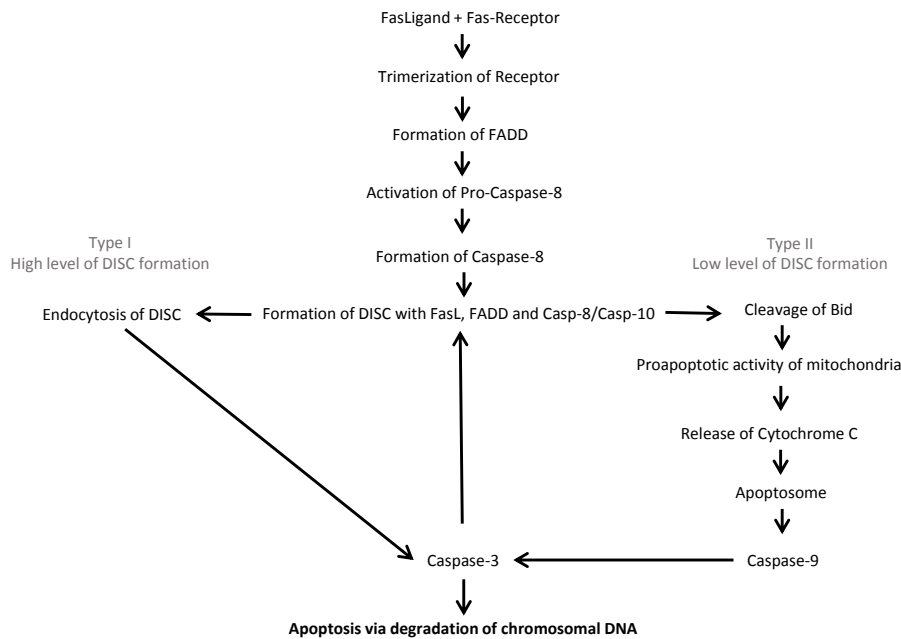


Figure 3.2: Overview of the pathways type I and type II in the Fas-Ligand (FasL) induced apoptosis. The assembly of the FasL in the Fas receptor is leading to the trimerization of the receptor and the Fas-associated Protein with Death Domain (FADD) is formed. Pro-caspase-8 is activated and subsequently is Caspase-8. The FasL, FADD and Caspase-8 and also Caspase-10 result in the Death Inducing Signaling Complex (DISC). With high levels of DISC formation, the type I pathway is triggered, where the Caspase-3 is directly activated, which finally is leading to cell death via the degradation of chromosomal DNA (left). The type II pathway is induced with low levels of DISC formation and via the activity of the mitochondria and the release of cytochrome c, the caspase-9 is triggered via the apoptosome and the cell is undergoing apoptosis (right).

3.2 Nanotoxicity Screening

Nanotechnology was identified as a key enabling technology of the 21st century [97]. The use of nanomaterials has the great potential to support challenges in health care and energy deficiencies. Nevertheless, the widespread use of nanomaterials in consumer products, such as cosmetics, food, medical applications, clothes and household products, points out that toxicological research and health risk assessment is inevitable, to analyze the impact on the environment and the human body. Risk assessment is a difficult task, since the impact of nanomaterial varies tremendously, depending on material, size, shape etc. . Also the method of choice and the cell line have consequences on the outcomes. To obtain insight in the various effects of manufactured nanomaterials (MNMs), a large-scale study was performed by two institutes (Karlsruhe Institute of Technology (KIT) and European Commission Joint Research Centre (JRC)), three universities (LMU Munich, University College Dublin and the University of Birmingham) as well as one industrial partner (Promethean Particles) [18]. This study was realized within the European Commission's 7th Framework Programme project NanoMILE.

The aim of the project was to get an overall inside view of different MNMs with different surface characteristics in various cell types (liver, lung, colon and the immune system). The experiments were performed with different techniques, mainly high-throughput/-content (HT/C) methods. Different end-points were examined such as cell count, mitochondrial membrane potential, lysosomal acidification, steatosis, cell membrane permeability and apoptotic cell death. The data was standardized using the Signal to Noise Ratio (SNR) to compare the results across the laboratories. The SNR is defined as the determined value subtracted by the mean of the background, and divided by the background standard deviation [18]. No additional information for significance is needed, since the SNR is providing it indirectly. All results can be read in Hansjosten et al. [18], in the following paragraph the results of experiments, done by LMU (P. Röttgermann and A. Murschhauser) are summarized.

14 soluble MNM were tested, ranging from SiO₂, TiO₂, CeO₂, ZnO and Ag with various coatings. PS-NH₂ (100 µg mL⁻¹) MNM was used as a positive control, whereas pure medium was taken as negative control. The concentrations exposed to A549 cells, seeded on microstructured surfaces (see the protocol in the Appendix A.2), were 1, 2, 3.9, 7.8, 15.6, 31.2, 62.5 and 125 µg mL⁻¹. These final concentrations correlate with surface area doses of 0.3, 0.6, 1.2, 2.4, 4.9, 9.8, 19.5 and 39.1 µg/cm². Nanoparticle solutions were prepared following standard operation procedures (SOPs) when not delivered already in solution. The fetal bovine serum (FBS) used for this study was centrally purchased as one lot (Gibco, Life Technologies, Darmstadt, Germany, Cat. Number 10270-106, LOT-Number 41G1931 K). The end-points chosen by LMU were cell death, imaged with the nuclear stain PI (2%, (v/v)) and Hoechst 33342 (25 nM), as well as cell viability, which was illustrated with the caspase-3/7 marker

CellEvent green (3%, (v/v)). The cells were exposed to the nanoparticles diluted in DMEM together with the fluorescence markers for 24 h, at 37°C. Phase contrast and fluorescence images (DAPI, PI and GFP) were taken after incubation. The data analysis was performed using the in-house written ImageJ plugin Microwell Analysis, as described in Chapter 2.3.2, as well as custom MATLAB codes (P. Röttgermann) to analyze the SNR. In our case, the SNR was calculated as the following:

$$SNR = \frac{X_c - \overline{NC_c}}{SD_{NC}}$$

where X_c is the average of the number of viable cells (X) for the concentration c , evaluated indirectly with the PI stain in different experiments, for each MNM and each concentration, NC_c is the average of dead cells in the negative controls (NC), SD_c the Standard Deviation (SD) of dead cells in the negative controls. The average number of viable cells was calculated by subtracting the ratio of dead cells (PI positive) and the total number of cells from one. The Null Hypothesis implies that no effect of the MNM compared to the negative control is detected. The threshold -2 would hint a downwards effect and +2 an upwards effect. The value 2 is retrieved from the hypothesis that the means of two normal distributed variables can be assumed to be equal, if the variables are received from different number of experiments and unknown, but similar variance [18]. The effect has to be observed for at least two subsequent concentrations to be significant.

In summary, we could observe that single A549 cells (LMU results, Figure 3.3, right column) were more sensitive than monolayer A549 cells (KIT/JRC/UCD, Figure 3.3, left column) in all conditions. Silica particles and also the CeO_2 particles, except for one outlier, had no toxic effects, neither in monolayer nor at the single-cell level, as indicated in green in the heat map. TiO_2 particles seem to be more toxic to single cells than to bulk cells, since the color code for bulk cells is green while for the single cells, especially the highest concentration of the hydrophobic and hydrophilic nanoparticles, the color is changing to red (toxic). Whereas ZnO particles only seem to be toxic to bulk cells in the two highest concentrations, single cells are dying after a treatment with the four highest concentrations. Furthermore, the toxicity of silver nanoparticles is increasing dose-dependently for bulk measurements, while for single cells silver nanoparticles were toxic in all concentrations. These outcomes clearly state that single-cell measurements have to be considered for future nanotoxicity studies, since the sensitivity of the cells is much higher at the single-cell level than in confluent monolayers.

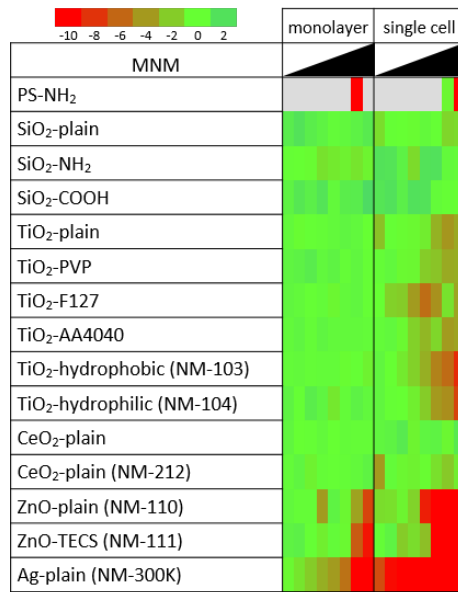


Figure 3.3: Heat map of Manufactured Nanomaterial (MNM) induced cell death readouts in monolayer and single cells. Monolayer cells (left column) and single cells (right column) were exposed to different MNM as indicated for 24 h in DMEM and 10% FBS (v/v) with the range of concentrations from 1 to 125 $\mu\text{g mL}^{-1}$. Dead cells were evaluated by the Propidium Iodide stain, indicating plasma membrane permeabilization, and the total number of cells with Hoechst 33342. The number of viable cells was calculated by subtracting the ratio of dead cells and the total number of cells from one. The Signal-to-Noise-Ratio (SNR) is calculated by subtracting the dead cells of the negative controls from the number of viable cells and normalizing the difference by the standard deviation of the negative controls. The SNRs are illustrated as heat map, where the color code is ranging from dark green (more viable cells than the negative control) to red (decrease of viability). Reprinted from Supplementary Information of [18] with permission from Springer Nature.

3.3 Correlations in the Initiation Phase: LMP, MOMP and ROS

The need of further detailed investigation of nanoparticle impact on the single-cell level was shown in the preceding broadly based study as well as described in Chapter 2.1. Single cells are more sensitive to nanomaterials than cells in bulk measurements. Thus, single-cell time-lapse measurements with the model PS-NH₂ nanoparticles were performed in A549 as well as in Huh7.

The following chapter is based on the publication Murschhauser et al. [36].

Hereafter, the distribution of event (offset) times of the three early markers (LysoTracker, CellROX and TMRM), measured in A549 cells after apoptosis induction with 25 and 100 $\mu\text{g mL}^{-1}$ PS-NH₂ nanoparticles or 2 μM STS, were analyzed (Figure 3.4). A549 cells were seeded onto micropatterned surfaces (see protocol in the Appendix A.2) and automated live-cell imaging on single-cell arrays (LISCA) was

performed to obtain single-cell time traces. The event times were extracted with the maximum-likelihood routine and only cells were included, which showed both marker signals. The data from up to 600 cells per marker are pooled from different marker combinations. Approximated log-normal distributions are indicated with a black line in each plot. By comparison of the NP exposures, a dose-dependent timing of the events is observed. The maxima for the lower concentration of NPs ($25 \mu\text{g mL}^{-1}$ NPs, brighter colored distributions), namely 11-13 h, are shifted towards later time-points than the ones for the higher concentration ($100 \mu\text{g mL}^{-1}$ NPs, darker colors), which are observed between 5-9 h. The time and dose-dependent cytotoxicity of amino-modified nanoparticles is in good agreement with literature [21, 62, 67]. The event time distributions of staurosporine treated cells show a timing in between the two NP concentrations, namely between 8-10 h. To exclude the suspicion of side effects caused by the fluorescence markers, negative controls, where only media and the markers without apoptosis trigger were added to the cells, were performed. Experiments, which showed more than 20% double positive cells, were excluded from analysis. Also the dependency of marker-combinations was examined, and found to be present in some combinations, causing slight shifts (see data in Supplementary Material of Murschhauser et al. [36]). Furthermore, the day-to-day variance was evaluated by comparing identical marker combinations measured on different days. The scattering of the events was justifiable (Supplementary Material Murschhauser et al. [36]). In the Supplementary Material all the statistics of the histograms and the following plots can be found as well [36].

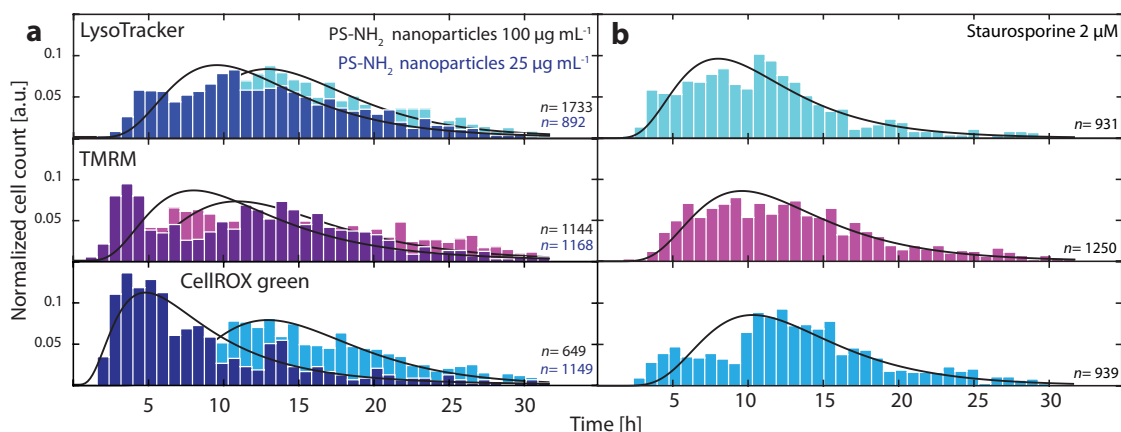


Figure 3.4: Event time distributions of early markers in A549 cells over 30 h. Cells were exposed to $25 \mu\text{g mL}^{-1}$ (brighter colors) and $100 \mu\text{g mL}^{-1}$ PS-NH₂ nanoparticles (darker colors, a) or $2 \mu\text{M}$ STS (b) and the event times are illustrated for the fluorescence markers LysoTracker, Tetramethylrhodamine (TMRM), CellROX green. Each graph consists of a set of pooled experiments with different marker combinations. Only cells with both marker signals are shown (n). Log-normal distributions are fitted to the distributions (black line). Adapted from [36], licensed under a Creative Commons license [39].

Nevertheless, the aim to clarify the sequence of events during NP induced apoptosis could not be accomplished with the histograms, since the broadness of the distribution width is too large compared to the shifts of the maxima for the different markers.

Thus, to unravel the order of events, pairwise correlations of the events (1) and (2) of one marker combination were investigated, instead of averaged event times. Therefore, $t_{\text{event}}(1)$ was plotted against $t_{\text{event}}(2)$ in scatter plots for the three different exposures 25 and 100 $\mu\text{g mL}^{-1}$ PS-NH₂ nanoparticles (Figure 3.5a, d, g and 3.5b, e, h) and 2 μM STS, respectively (Figure 3.5c, f, i). The different marker combinations were plotted per row for each treatment. The scatter plots are divided in two halves, to identify the chronological order of events. For example, if the single-cell data points are in average above the diagonal, event (2) follows event (1). If the average of event time points are directly on the diagonal, the events happen simultaneously. Event clusters are identified by mean-shift clustering. The ellipses shown are gained with Principal Component Analysis (PCA) and illustrate the centers and widths of event time distributions. The length of the semi-axes of the ellipses, rising from the center of the ellipse and oriented along the two components respectively, visualize the mean square displacement of events. The PCA is a powerful tool to unravel the average timing of events, thus the order and the delay time between two correlated events (see more details in Chapter 2.5.3).

For PS-NH₂ NP induced apoptosis, the lysosomal pathway LMP-MOMP-OxBurst was identified in both NP concentrations. The outcomes suggest that the lysosomal breakdown is triggering the permeabilization of the outer mitochondria membrane and the following increase in ROS level. Also here, the higher NP dose shows a higher impact and the event times shift to earlier timing. Furthermore, for the higher NP dose, a bimodal behavior could be observed, indicated by data points underneath the diagonal. In summary, the event time points of all marker correlations hint the existence of a second pathway, in fact a mitochondrial pathway. The sequence of events is MOMP-OxBurst-LMP, showing that with the breakdown of the mitochondrial potential the cellular stress level is increasing, indicated by the oxidative breakdown, followed by the lysosomal leakage. For the staurosporine induced apoptosis, similar scatter plots to the ones of the high NP dose are obtained. Also here, both pathways, the lysosomal signaling cascade as well as the mitochondria triggered pathway, are shown in the two-dimensional marker correlations.

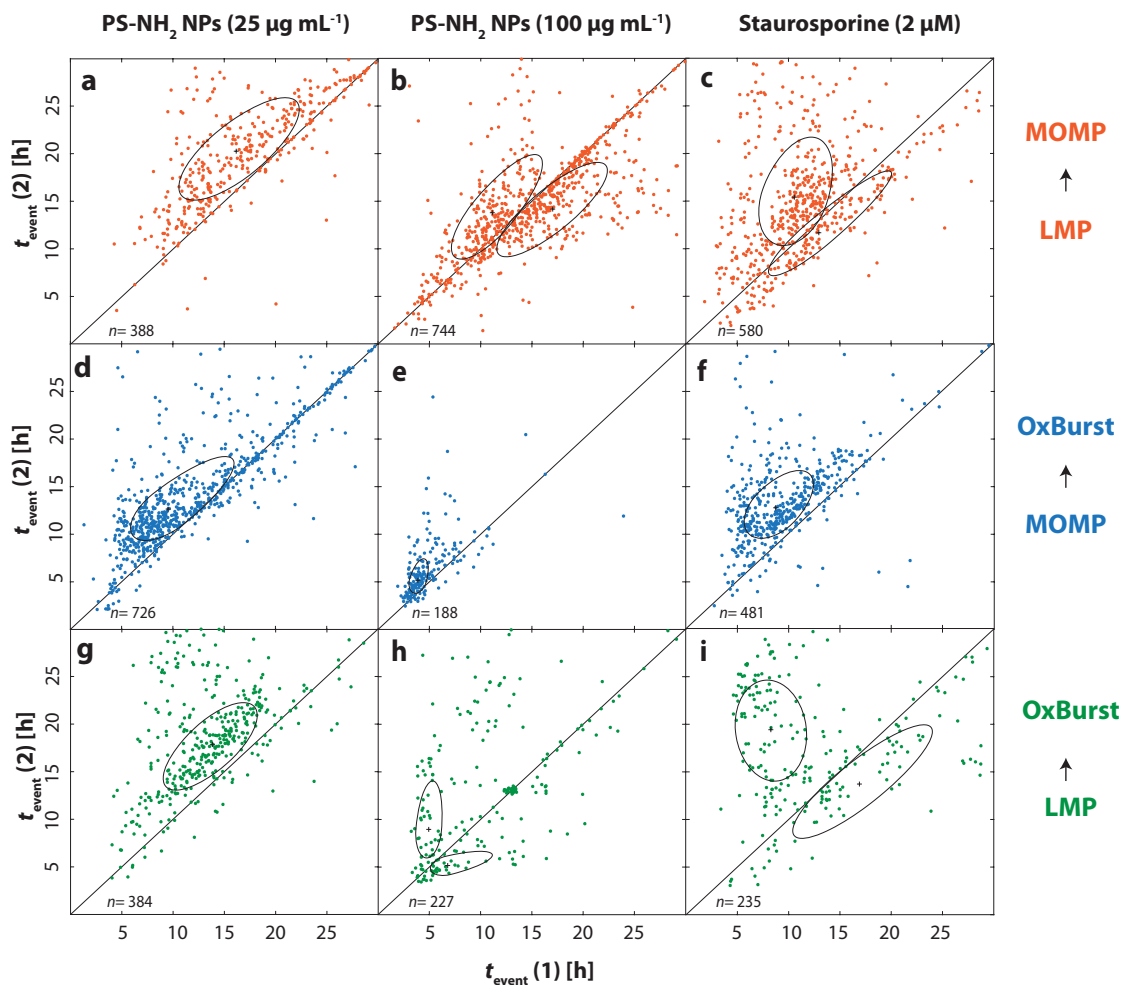


Figure 3.5: Two-dimensional scatter plots of event times obtained by pairwise-marker correlations measured in A549 cells. Pairwise correlations of event times $t_{\text{event}}(1)$ and $t_{\text{event}}(2)$ of fluorescence markers are shown in each scatter plot. Apoptosis was induced with the treatment of cells to $25 \mu\text{g mL}^{-1}$ nanoparticles (left), $100 \mu\text{g mL}^{-1}$ nanoparticles (middle) or STS (right). MOMP was correlated with LMP (a, b, c) as well as with OxBurst (d, e, f). Moreover, LMP and OxBurst were correlated with each other (g, h, i). n is the number of depicted cells. Adapted from [36], licensed under a Creative Commons license [39].

The A549 cell line was used as a lung cancer model system, which is often used in cytotoxic studies to investigate the inhalation pathways. Additionally, NPs are uptaken by the intestine and accumulate in the liver [18]. Thus, the Huh7 human hepatocarcinoma cell line was a suitable second model system for comparison. Interestingly, also in the liver cancer cells the dominant pathway with the mitochondria as key player was seen, even though with longer delay times than examined for A549 cells (Figure 3.6). Furthermore, the dose-dependent shift to earlier time points for the higher NP dose, which was observed in A549 cells, could be reproduced with

Huh7 cells. However, the second pathway, observed for the high dose in A549 cells, was not evident for Huh7 cells.

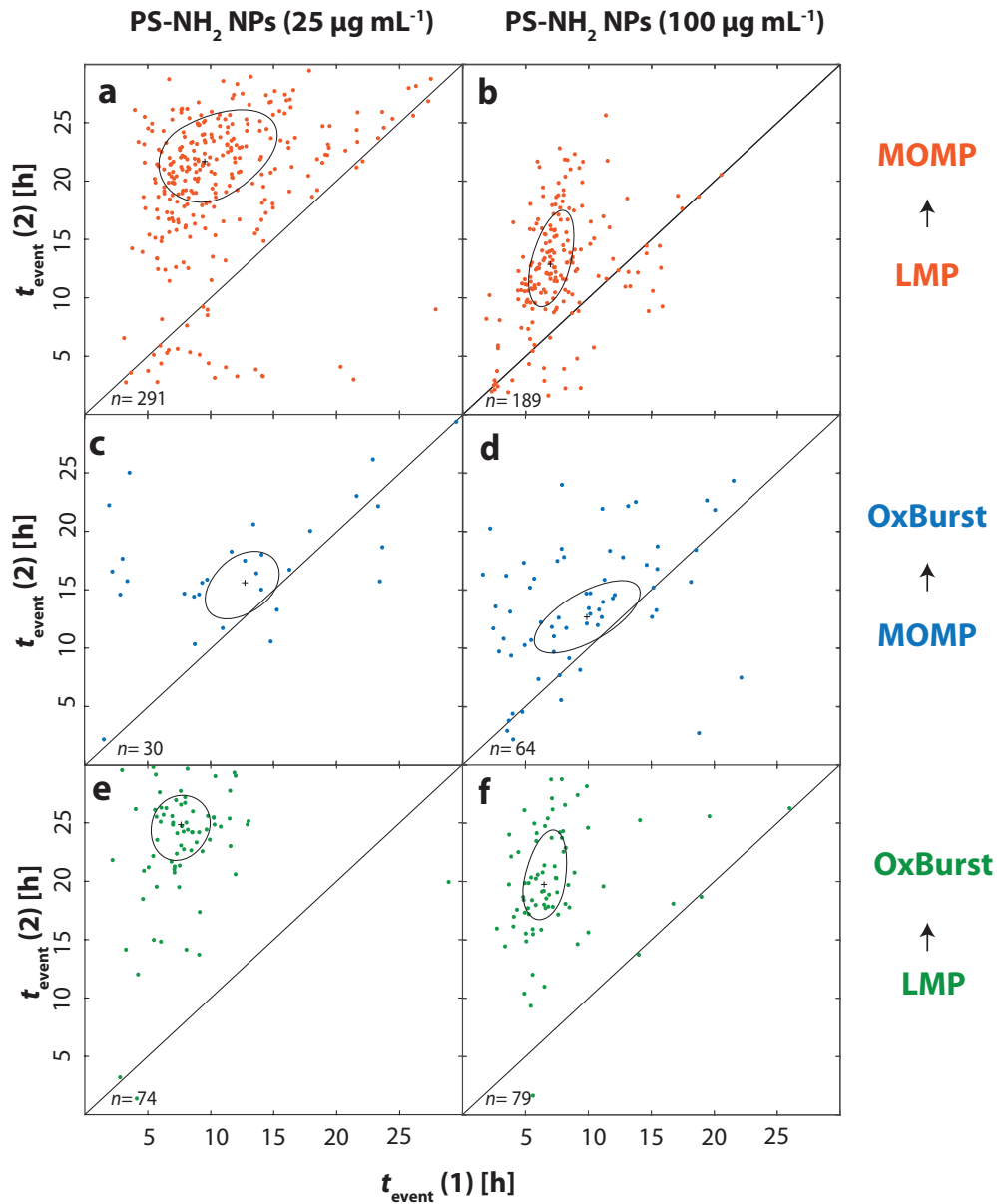


Figure 3.6: Pairwise marker correlations of single-cell event times in Huh7 cells. Scatter plots were obtained by correlation of $t_{\text{event}}(1)$ and $t_{\text{event}}(2)$ of one marker combination respectively. Namely, MOMP was combined with LMP (a, b), and OxBurst (c, d) as well as LMP was correlated with OxBurst (e, f). Huh7 cells were exposed to $25 \mu\text{g mL}^{-1}$ nanoparticles (left column) or $100 \mu\text{g mL}^{-1}$ nanoparticles (right column). n indicates the number of cell shown. Adapted from [36], licensed under a Creative Commons license [39].

Figure 3.7 summarizes the findings of 58 nm PS-NH₂ NP induced apoptosis in A549 cells in one scheme. The nanoparticles trigger cell death via the lysosomal pathway, which is in good agreement with literature [41, 62, 69]. The breakup of the lysosomes triggers the permeabilization of the mitochondria and the ROS level is increasing. This sequence of events was detected and is indicated as LMP-MOMP-OxBurst in the scheme. Additional to the mitochondria triggered pathway, which was observed for both the low (25 $\mu\text{g mL}^{-1}$) and the high concentration of NPs (100 $\mu\text{g mL}^{-1}$), an additional mitochondrial cascade was observed, which seems to be directly activated via the mitochondria. This branch pathway was observed for the high concentration of nanoparticles (100 $\mu\text{g mL}^{-1}$), as well as for staurosporine. The MOMP-OxBurst-LMP pathway (right side of Figure 3.7) is in good agreement with the findings of Baumgartner et al., who suggest also the presence of two signaling pathways [77]. But only the powerful tool of pairwise marker correlations of single-cells achieved with time-lapse measurements have the capability to unravel such bimodal behavior directly and in parallel. However, it should be kept in mind that the event correlations do not imply causal relations between the correlated events. Finally, both pathways lead to cell death, indicated by the plasma membrane permeabilization (PMP), via activation of caspases-3 and -7 and the consequent flip of phosphatidylserine from the inner to the outer leaflet of the plasma membrane (see following Chapter 3.4).

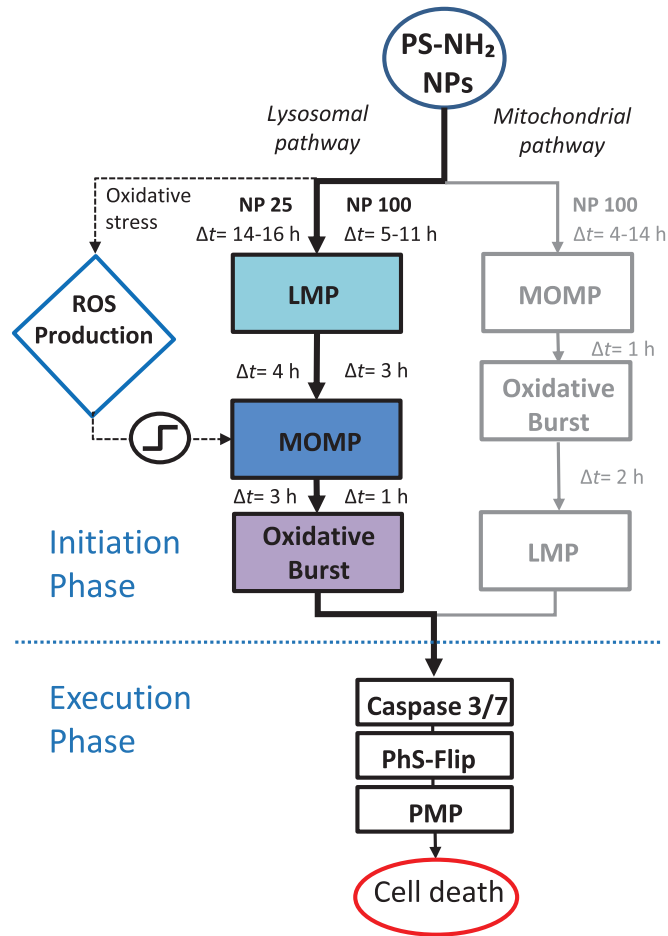


Figure 3.7: Schematic model of lysosomal and mitochondrial pathways in NP induced apoptosis in A549 cells. On the left hand the lysosomal pathway is indicated, which is triggered by the addition of $25 \mu\text{g mL}^{-1}$ and $100 \mu\text{g mL}^{-1}$ amino-modified polystyrene (PS-NH₂) nanoparticles. The nanoparticles are uptaken and accumulate in the lysosomes, thus leading to swelling and lysosomal rupture. Lysosomal content is released, resulting in MOMP and oxidative Burst (OxBurst). A critical threshold in ROS production is influencing MOMP, but not LMP (blue framed rhombus). Furthermore, for the higher concentration of nanoparticles, a second, mitochondria provoked signaling cascade is observed. OxBurst is following MOMP and leads to LMP. Both pathways, analyzed in detail in the initiation phase, drive the cell to cell death, indicated by the plasma membrane permeabilization (PMP), via activation of caspase-3 and -7 and via the flip of phosphatidylserine from the inner to the outer side of the plasma membrane (PhS-Flip, execution phase). The delay times between the measured events are indicated as Δt . Adapted from [36], licensed under a Creative Commons license [39].

3.4 The Execution Phase: Caspases, PhS-Flip and Final Cell Death

The execution phase is the second phase in apoptosis, following the initiation phase. After the lysosomal breakdown, the cathepsin D release followed by the mitochondrial collapse and a significant increase in ROS level, taking place in the first stage of programmed cell death, executioner caspases, namely caspase-3 and 7 are activated. The activation leads to the flip of phosphatidylserine from the inner to the outer leaflet of the plasma membrane. Finally, the plasma membrane is permeabilized and the cell death programme is completed. But, also in this phase, the chronological order and the timing in between the events is still not fully understood.

Therefore, late marker combinations were analyzed. Firstly, the distributions of event times in late marker combinations were investigated (Figure 3.8). A549 cells were exposed to $25 \mu\text{g mL}^{-1}$ nanoparticles (Figure 3.8a, bright colored distributions) or $100 \mu\text{g mL}^{-1}$ nanoparticles (Figure 3.8a, darker colors) and $2 \mu\text{M}$ staurosporine (Figure 3.8b). The data was pooled from different marker combinations measured in different experiments. The number of cells is given by n and only cells with both marker signals are shown.

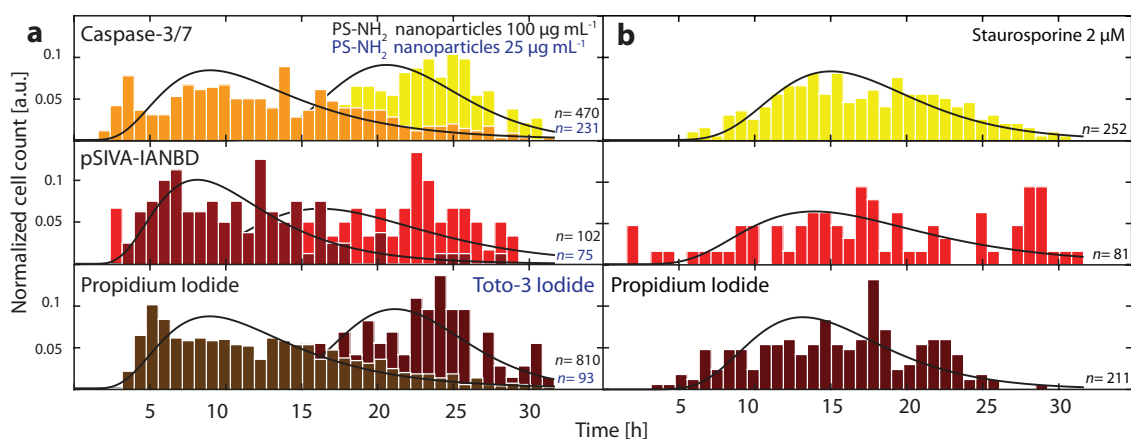


Figure 3.8: Distribution of event times for late markers Caspase-3, pSIVA-IANBD and Toto-3 Iodide or Propidium Iodide after apoptosis induction with $25 \mu\text{g mL}^{-1}$ nanoparticles (a, bright colors), $100 \mu\text{g mL}^{-1}$ nanoparticles (a, darker colors) or $2 \mu\text{M}$ STS (b) in A549 cells. The number of cells is indicated with n , which is gained from different experiments and different marker combinations. Only double positive cells are shown. Adapted from [36], licensed under a Creative Commons license [39].

As seen for the early marker combinations, the timing of the event times, thus the maxima of distributions shifted to earlier time points for the high dose of NP in comparison to the low dose of NP. In numbers, the maxima for the low NP dose are between 16-21 h and for the high dose between 8-9 h. Furthermore, also here,

as seen for the early marker combinations, the STS induced apoptosis shows event times in between the two NP concentrations (13-15 h).

To examine the sequence and timing of events in the execution phase of NP induced apoptosis, different marker combinations were tested. First of all, the correlation of the oxidative burst (OxBurst), indicating preceding intracellular stress, and the final event, the plasma membrane permeabilization (PMP), which is accompanied with cell death, was investigated. As expected, PMP is following OxBurst (Figure 3.9). Further, the events for the higher dose (Figure 3.9b) are evidently earlier than for the lower dose (Figure 3.9a) and STS (Figure 3.9c). Moreover, the events for the 100 $\mu\text{g mL}^{-1}$ nanoparticles point out a higher correlation, indicated by a more narrow ellipse, than the other two exposures.

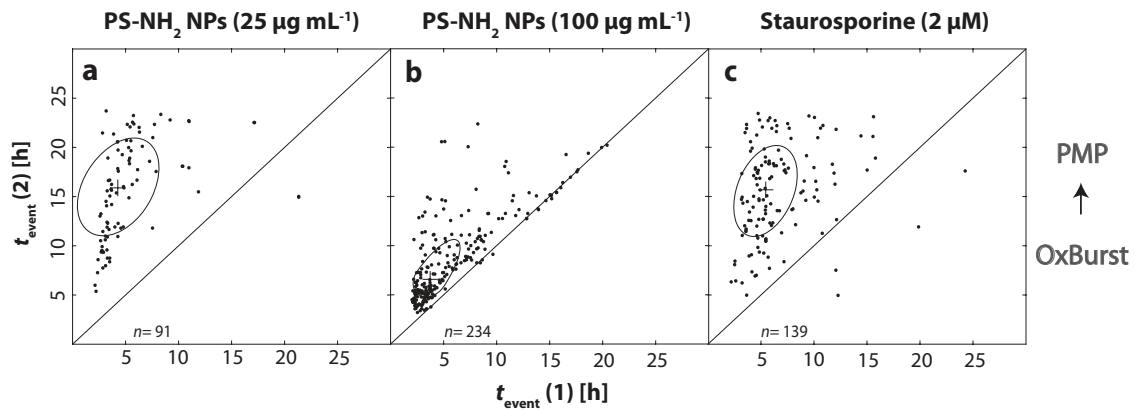


Figure 3.9: Two-dimensional scatter plots of event times for OxBurst and PMP correlations. A549 cells were treated with 25 $\mu\text{g mL}^{-1}$ nanoparticles (a), 100 $\mu\text{g mL}^{-1}$ nanoparticles (b) or 2 μM STS (c). Adapted from the Supplementary Information of [36], licensed under a Creative Commons license [39].

Finally, it was recognized that the noise in the scatter plots is mainly descending from events of the apoptosis initiation phase. This was proven when comparing correlations between an early with a late marker as well as the comparison between two late marker combinations (Figure 3.10). The first combination (Figure 3.10a) shows more distributed data points, thus more scattering, whereas combinations between late markers yield more narrow correlations (Figure 3.10b). This is indicating that the noise of the heterogeneous signals has its origin in the early phase of apoptosis.

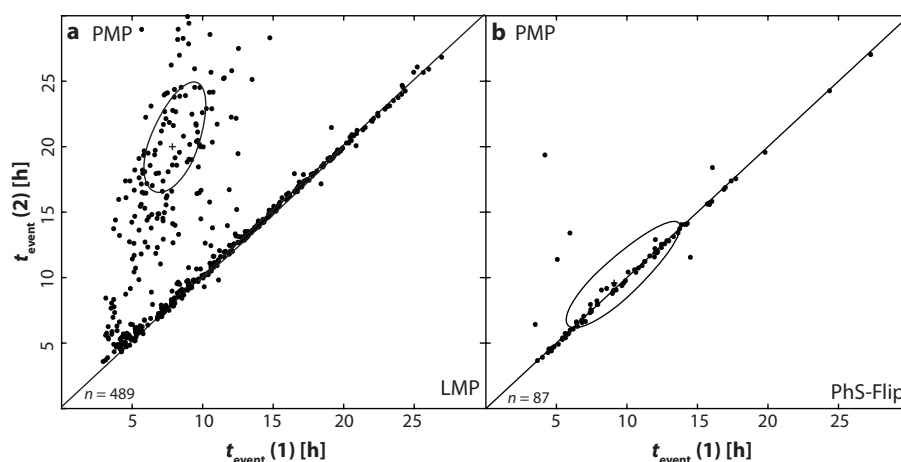


Figure 3.10: Correlation of PMP with (a) LMP and (b) PhS-Flip. A549 cells were exposed to $100 \mu\text{g mL}^{-1}$ nanoparticles. Correlations between late markers show narrow timing (b), whereas correlations of late markers with early markers show broader scattering, indicating that the noise stems from early events. n is the number of shown cells. Adapted from the Supplementary Information of [36], licensed under a Creative Commons license [39].

3.5 Correlation between Reactive Oxygen Species and LMP or MOMP

What are ROS?

ROS can be superoxide anions ($\text{O}_2^{\circ-}$), hydroxyl radicals (HO°), peroxy (RO_2°), alkoxy (RO°), nitroxyl radicals (NO°) or other non radical oxygen derived radicals, such as hydrogen peroxide (H_2O_2), organic hydroperoxides (ROOH) or hypochlorous acid (HOCl) [83].

Reactive oxygen species (ROS) are necessary in the cell as redox messengers in intracellular signaling and cellular regulation. ROS is known to be mainly generated in mitochondria due to incomplete reduction of oxygen during oxidative phosphorylation during ATP production. Defects in mitochondrial function e.g., inefficient oxidative phosphorylation and MOMP can direct increased ROS levels [98]. As soon as ROS are not only byproducts of cellular oxidative metabolism, but produced in higher concentrations due to cellular stress, the redox functions are not maintainable and unregulated signaling, cytotoxicity, DNA damage and apoptosis can occur [61]. Further, ROS seem to be particularly involved in degenerative diseases such as arthritis, Alzheimer's disease, diabetes, Parkinson's disease and cancer [61]. Thus, on the one hand, ROS can be beneficial for the cell and essential for survival, but on the other hand also fatal. Furthermore, ROS can induce cancer, then again ROS can also be introduced as cancer therapy in the sense that ROS can trigger apopto-

sis in cancer cells. Thus, ROS plays in both, cancer and apoptosis, a role. In this study, the aim was to understand the down-stream signaling connected with ROS in apoptosis signaling cascades. Especially the strong evidence for a link between ROS and LMP as well as the relation between ROS and MOMP was scope of this investigation.

What is the source and the cause of ROS?

The main source of ROS is the mitochondria, which is at the same time also target of ROS [54]. Also the endoplasmatic reticulum is an important source of ROS [99]. ROS can arise from lipid peroxidation, increasing activity of enzymes, such as NADPH oxidase, xanthine oxidase, myeloperoxidase and flavoprotein oxidases, but also from transient metals, hemoglobin, riboflavin, catechol amines and particularly from the electron transport chain in the mitochondria [100].

In general, any external trigger, which is causing cellular stress, can increase the ROS level. Chemotherapy, radiation, inflammatory cells and also nanomaterials can induce apoptotic concentrations of ROS. In this study, the impact of nanoparticles, namely amino-modified polystyrene (PS-NH₂) nanoparticles were investigated.

ROS in non physiological concentrations was shown to cause the permeabilization of lysosomes as well as the breakdown of mitochondria [43, 101]. Thus, in our study, not only the event time of ROS was extracted from the single-cell time traces, but also the increase in CellROX intensity. The slope of the curve, examined with the maximum-likelihood fitting routine, is assumed to represent the production of ROS, thus the ROS rate. For the analysis whether the ROS rate correlates with MOMP or LMP, the production of ROS was plotted against the event times of MOMP (Figure 3.11a-c) and LMP (Figure 3.11d-f). A549 cells were treated with 25 $\mu\text{g mL}^{-1}$ 58 nm PS-NH₂ nanoparticles (Figure 3.11a and d), 100 $\mu\text{g mL}^{-1}$ PS-NH₂ nanoparticles (Figure 3.11b and e) and 2 μM staurosporine (Figure 3.11c and f). In the case of the correlation of ROS with MOMP, a critical threshold of ROS presumably exists, which is inducing MOMP. Thus, when the rate of ROS is higher than this threshold, MOMP supposedly occurs earlier (Figure 3.11a-c), indicated with Pearson Correlation Coefficient (PCC) values of -0.18, -0.26 and -0.17, respectively. This inverse correlation was not observed when ROS was correlated with LMP (Figure 3.11d-f). In this case, very low PCC values were evaluated. Details on the PCC are explained in the Supplementary Information of Murschhauser et al. [36].

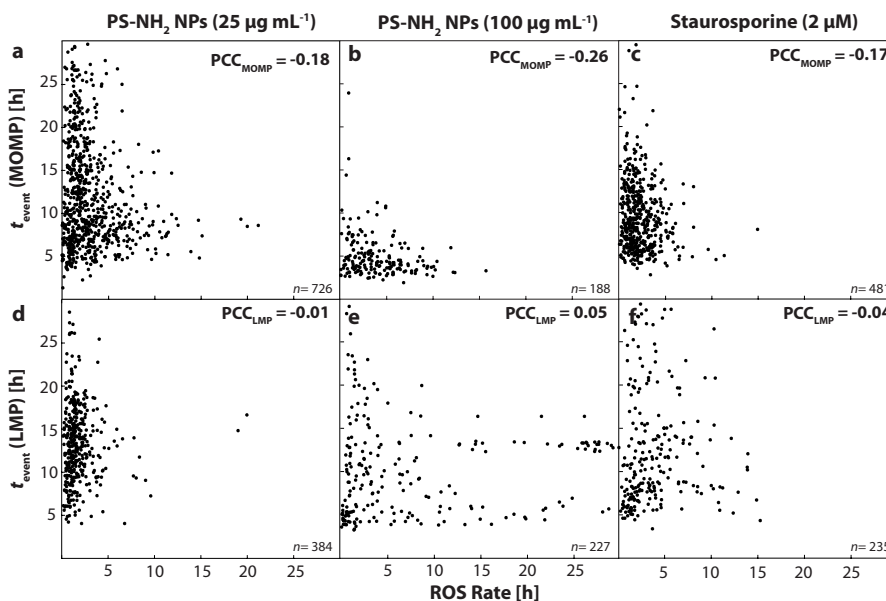


Figure 3.11: A549 cells treated with 58 nm PS-NH₂ nanoparticles at 25 µg mL⁻¹ (Fig. 3.11a, d) or 100 µg mL⁻¹ (Fig. 3.11b, e) and staurosporine (Fig.3.11c, f). The ROS rate correlates with MOMP, but not with LMP. The linear increase of the CellROX fluorescence time traces was assumed to correlate with the amount of ROS (ROS rate). The ROS production rate was plotted against the event times of MOMP ($t_{\text{event}}(\text{MOMP})$) and LMP ($t_{\text{event}}(\text{LMP})$), respectively). The higher the ROS production, the earlier the event MOMP was detected (Figure 3.11a-c), but no correlation between the ROS rate and LMP was seen (Fig.3.11c-f). The Pearson Correlation Coefficient (PCC) is shown in the upper right corner for each sub graph. n is the number of analyzed cells shown in the graph. Adapted from [36], licensed under a Creative Commons license [39].

3.6 Cathepsin Inhibition with Pepstatin A

The involvement of lysosomes in apoptosis was already discussed in detail in Chapter 3.1. In short, after addition of an apoptotic stimuli, e.g. staurosporine, the lysosomes are permeabilized (LMP), which leads to the release of cathepsin D into the cytoplasm, where further down-stream signaling is activated. Various signaling pathways can then be mediated via caspases or the release of pro-apoptotic factors like the protein cytochrome *c* from the mitochondria (after MOMP) into the cytosol. Mitochondrial ROS is leading to a positive feedback loop, triggering again LMP [43, 76, 102, 103]. In this chapter, the effect of cathepsin D is discussed, since it seems to play a crucial role in the apoptotic signaling cascade. Especially, its inhibition is interesting, and we investigated the question whether the following events in the pathway can be blocked without influencing the signaling cascade itself.

Cathepsin D belongs to the class of proteases, enzymes which hydrolyze peptide bonds, and is the only aspartic protease in the lysosomes [104]. The term 'cathepsin' stands for 'lysosomal proteolytic enzyme' [105] and cathepsins are the largest group

of proteolytic enzymes in the lysosomes. Pepstatin A is shown to inhibit [105, 106] or delay apoptosis [70, 107]. In the latter study, PS-NH₂ NP induced apoptosis was delayed, but the inhibition could not protect the cells from damage, suggesting that the activation of caspase-3/7 was not affected. The authors suggest that cathepsin D does not play a major role in caspase-dependent apoptosis. But, that is in contradiction with literature [43, 77, 80, 105]. More likely, pepstatin A may not have inhibited the release of cathepsin D completely, even though they used a relatively high concentration (50 μ M) and a long incubation time (16 h), or alternative signaling pathways were leading to apoptosis. Since cathepsin D is also involved in ROS dependent apoptosis [102, 103, 108, 109], the events MOMP, LMP as well as OxBurst were measured in all possible combinations (LMP-MOMP, MOMP-OxBurst and LMP-OxBurst). Apoptosis was induced with 2 μ M staurosporine, since cathepsin D release was detected as event in STS triggered cell death and is well known in literature [80, 110, 111]. The concentration used by Wang et al. was relatively high (50 μ M) and the incubation time quite long (16 h) [70]. These experimental settings might have been too invasive, thus potentially triggering side effects or initiating other signaling. Thus, a lower concentration of 1 μ M pepstatin A was chosen and the A549 cells were only incubated with pepstatin A for 2 h before the addition of STS, presenting non-invasive conditions to avoid impacts on the complex signaling cascade or on the sensitive events. In these conditions, no evident effects of inhibition were recognized (Figure 3.12).

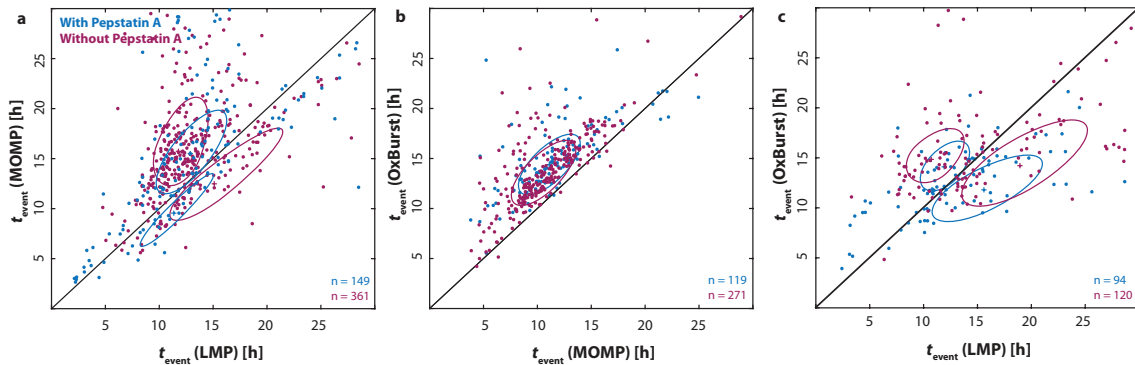


Figure 3.12: Correlations of single-cell events for A549 cells, triggered with 2 μ M staurosporine and incubated for 1 h with pepstatin-A (1 μ M), which forms 1:1 complexes with Cathepsin-D (blue) and without Pepstatin-A (magenta). Three different marker combinations were measured: LMP-MOMP (a), MOMP-OxBurst (b) and LMP-OxBurst (c).

The center of the clusters of pairwise marker combinations for cells treated with or without pepstatin A were not clearly distinguishable from each other in timing, neither in the marker combination of LMP-MOMP (Figure 3.12a) or MOMP-OxBurst (Figure 3.12b), nor for LMP-OxBurst (Figure 3.12c). The events for cells, which were inhibited with pepstatin A, were expected to be delayed in timing or even to be

blocked. Further, no increase in the number of double positive cells is evident; the number of cells exposed to the inhibitor were expected to be lower, if the inhibition would have been successful.

For further measurements, a longer incubation time as well as a higher concentration of pepstatin A is recommended, but still in a non invasive regime. Then, even more attention has to be payed to side effects, which could be followed with different controls, e.g. for morphology, doubling time, migration and detachment from the substrate.

3.7 Comparison with an External Cell Death Inducer: the Fas-Ligand

The analysis of the effects of FasL at the single-cell level in a dynamic manner is still under-researched and rarely shown before. Most of the bulk measurements are evaluated with single microscopy images or with end-point readouts. Thus, the temporal context of FasL cascades has been little studied so far. A greater understanding of the underlying processes and pathways can potentially overcome the resistance and increase the tumor cell response by addressing events more specifically. Brunk et al. found that also lysosomes are involved in FasL induced apoptosis [112]. It was also discovered that cathepsin D, which is released from leaking lysosomes, seems to play an essential role [113]. Further, the number of intact lysosomes depends on the time of exposure to anti-Fas antibody indicating that apoptosis is caused via lysosomal breakdown [110]. Moreover, Bojic et al. analyzed amongst others the events MOMP and LMP after induction with 200 ng mL^{-1} anti-Fas antibody (in combination with $1 \text{ }\mu\text{g/mL}$ chlorhexidine) in an end-point readout setup (flow cytometry) [114]. They found that the number of intact mitochondria decreased after 3 h and a considerable amount of damaged mitochondria was detected after 11 h. More than 30% destabilized lysosomes were seen 15 h after apoptosis induction. These results suggest that MOMP as well as LMP is involved in FasL induced apoptosis, even though at very late time points, suggesting the pathway type II. The Annexin cell viability stain showed double positive cells 15-18 h after apoptosis induction in very low numbers [114].

In our experiments, the A549 cell line was resistant to the TRAIL ligand, but not to the FasL, thus being a suited cell line as model system. Our results for single A549 cells after induction of apoptosis with 200 ng mL^{-1} FasL measured in time-lapse experiments, show also the event sequence of MOMP-LMP, although at even later time points (Figure 3.13a). Most of the cells show both signals after 22-23 h (center of the clusters with standard deviation: MOMP: $22.52 \pm 1.29 \text{ h}$, LMP: $23.83 \pm 1.18 \text{ h}$) with a time delay of $1.31 \pm 1.75 \text{ h}$. Note, that the statistic of 18 cells is low and allows only rough estimations. Further, the PhS-Flip is following MOMP (Figure 3.13b),

which is in agreement with Bojic et al. [114], even though at later time points. The shift to later time points could be due to the addition of chlorhexidine in the study of Bojic et al. [114]. In our case, most of the events are detected between 25 h (24.77 ± 0.87 h) and 27 h (27.06 ± 0.81 h), thus with a time delay of 2.29 ± 1.19 h. For reliable statements more cells need to be analyzed.

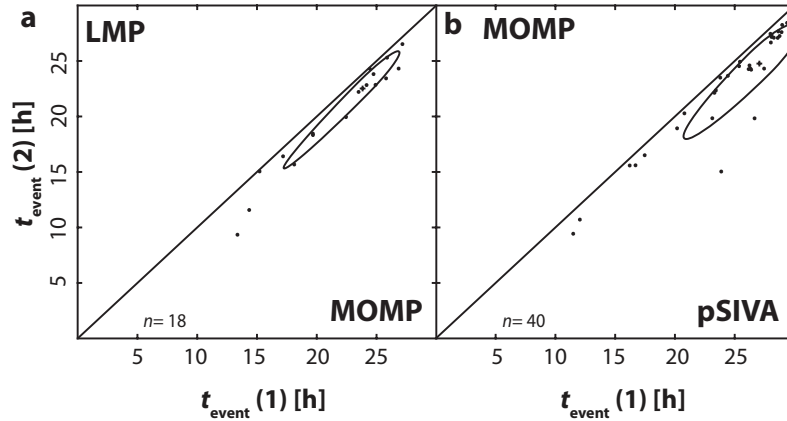


Figure 3.13: Pairwise fluorescence marker correlations of event times in single A549 cells. Two-dimensional representation of event times $t_{\text{event}}(1)$ and $t_{\text{event}}(2)$ of correlated markers induced by exposure of 200 ng mL^{-1} Fas-Ligand to cells. The center of the ellipses for LMP-MOMP are located at earlier time points (a) than for the correlation between MOMP and pSIVA-IANBD (b). n is the number of double positive cells plotted.

Overall, also our results hint for the pathway type II, since MOMP is involved and the timing of the events is quite late, which could emphasize that more processes are included, which is more time elaborative. Also the broad scattering of the events, seen in both marker correlations, could give indication for type II. It is noteworthy that the amount of cells, which are double positive comparing to the total amount of cells measured is quite low (max. 20%). The reason for this could be that many cells are detaching during the experiment and have to be sorted out, even when they showed apoptosis before detachment, since the decrease in intensity of the MOMP signal cannot be distinguished by the decrease in intensity caused by detachment. This is creating a slight bias, which could not be avoided in this case. A lower concentration of FasL (100 ng mL^{-1}) did not show significant apoptosis. Also a concentration of 500 ng mL^{-1} FasL was tested to increase the number of apoptotic cells but the detachment of cells was even worse. Thus, 200 ng mL^{-1} was chosen as a reasonable compromise. The FasL apoptosis induction is a surface phenomenon and the first steps, the ligand to receptor binding and receptor trimerization, take place on the cell membrane, which could explain the increased detachment, compared to STS or NP triggered apoptosis.

In future, the statistic could be improved with more experiments using a higher concentration of the FasL. Therefore, 3D environments could counter act the de-

tachment of the cells (Chapter 5). Further, more marker correlations, which would support a deeper insight into the signaling cascades. Especially, the involvement of caspases and cellular stress (ROS) are of interest.

3.8 The Delay Time Distribution Function

So far, we investigated pair-wise event-time correlations, which allow to distinguish between signaling cascades. In this chapter, deeper analysis of the event correlations in the early phase of apoptosis in A549 cells, induced with 25 $\mu\text{g mL}^{-1}$ 58 nm PS-NH₂ nanoparticles, is provided. This chapter is based on a manuscript of *Daniel Wosch e, Alexandra Murschhauser, Helmut H. Strey, Joachim O. R adler, 'Modeling signaling cascades based on single-cell event-time correlations'*, which is currently in preparation.

We discovered that the low concentration of amino-modified polystyrene nanoparticle triggers only the lysosomal signaling cascade, for which the three combinations of early markers were measured: LMP–MOMP, MOMP–OxBurst and LMP–OxBurst. The delay times between subsequent events were estimated for hundreds of single cells, namely A549 cells (Figure 3.14a) and Huh7 cells (Figure 3.14b). As signaling cascades in cells are chains of stochastic events, we assumed gamma-distributed delay times for the partial event chains (LMP–MOMP, MOMP–OxBurst). Visually, we can draw the relation between the events as connection series:

$$A \xrightarrow{P_{AB}(t)} B \xrightarrow{P_{BC}(t)} C$$

where P is the probability, event A is LMP, B is MOMP and C is OxBurst in this case. The gamma functions can be convolved and the sum of the delay times of A→B and B→C correlates with the delay times of A→C and can be calculated with the following equation:

$$P_{AC} = \int P_{AB}(\tau)P_{BC}(t - \tau)d\tau$$

In this case, the distribution of the total event chain (LMP–OxBurst) was shown to correspond to the convolution of the events of the partial chains (LMP–MOMP and MOMP–OxBurst) (Figure 3.14). The estimated gamma distributions are illustrated as blue lines on the histograms of the measured time delays. The parameters of the gamma distributions, κ for the number of processes and θ for the decay rate, as well as the number n of cells is indicated in each plot. The mean time delays $\mu = \kappa \theta$ of the path between LMP and MOMP and the path between MOMP and OxBurst sum up to the mean time delay of the path between LMP and OxBurst. The fits show that the measured data are described best by this model when the path between LMP and OxBurst involves two intermediate processes (for A549) or six subprocesses

(for Huh7), each having a duration around 7 or 16 h, respectively. However, visual inspection shows that the gamma distribution is merely a rough approximation to the data. The assumption that the intermediate processes are exponentially distributed might not suit the data perfectly, especially since the statistics for Huh7 cells is quite low. More likely, it might be a distribution with its maximum after a certain lag time. Hence, the number of intermediate processes indicated by κ is rather a nominal number representing a model parameter than the real number of biological processes.

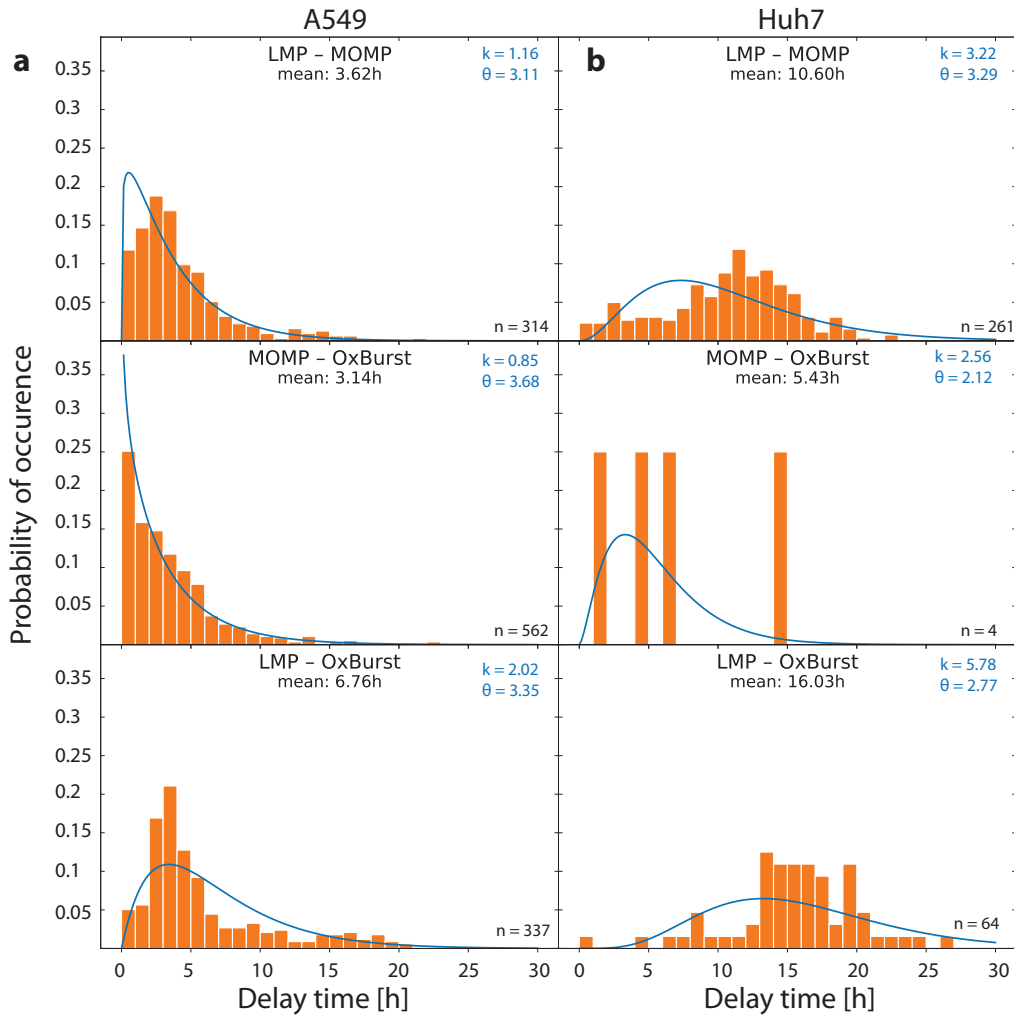


Figure 3.14: Gamma distributions for the early events LMP, OxBurst and MOMP measured in A549 (a) and Huh7 (b) cells after apoptosis induction with $25 \mu\text{g mL}^{-1}$ 58 nm PS-NH₂ nanoparticles. The measured delay times (in h) are plotted as orange histograms for the combinations LMP and MOMP, MOMP and OxBurst and LMP and OxBurst and are fitted by gamma distributions (blue lines). The estimated parameters κ and θ of the gamma distributions, n as the number of single cells and the calculated mean values of the gamma distributions, are indicated. The mean time delays of the two subpaths (first and second row) sum up to their concatenations (third row).

Chapter 4

Correlation Analysis in Combinatorial Chemotherapy of Etoposide and PS89

4.1 State of the Art

The following results are summarized in the manuscript Murschhauser A., Wosché D., Braig S., Angelika M. Vollmar, Rädler J. O., Targeting the ER-Mitochondria Interface Sensitizes the Leukemia Cells towards Cytostatics, which is currently in preparation.

Topoisomerase II Inhibitor Etoposide

The chemical structure of the anti-neoplastic reagent (neoplasm, abnormal growth of tissue) Etoposide (ETO), an epipodophyllotoxin (extracted from the root of the indian podophyllum plant), which inhibits the enzyme topoisomerase II (TOP2), is shown in Figure 4.1.

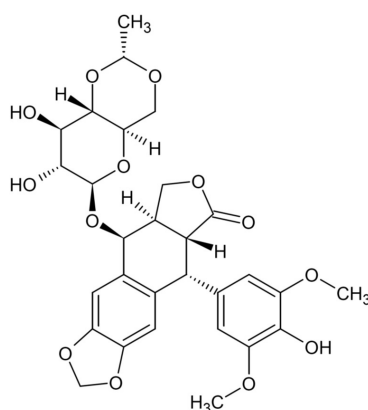


Figure 4.1: The chemical structure of the anti-neoplastic agent Etoposide, which is inhibiting the topoisomerase II.

TOP2 is a DNA unwinding enzyme, and essential for DNA replication, transcription, chromosomal segregation and DNA recombination [115]. The mode of action to inhibit TOP2 can be executed in two different ways: on the one hand, the activity of TOP2 can be inhibited directly, which is done by the so called TOP2 catalytic inhibitors, and on the other hand there are the TOP2 poisons, which include ETO, forming covalent complexes of TOP2 and DNA [116] (Figure 4.2).

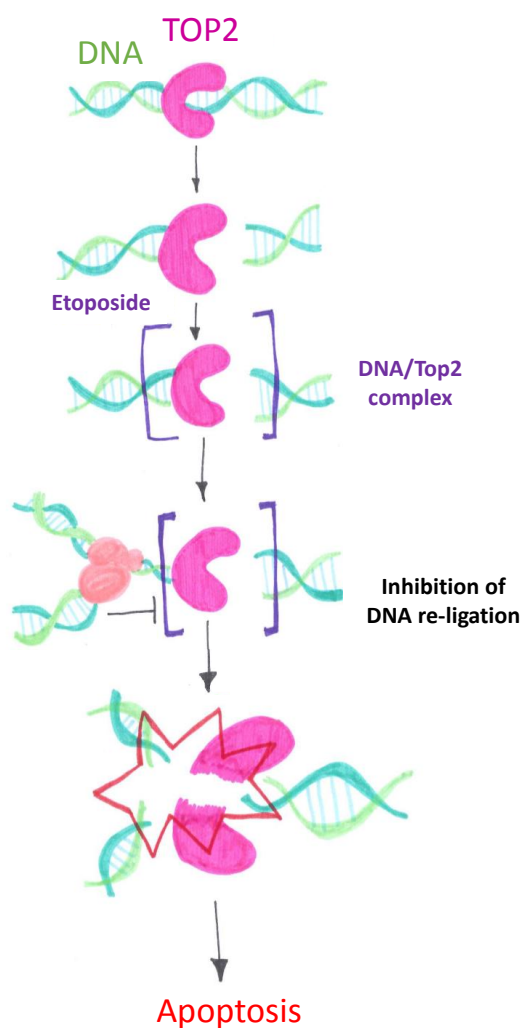


Figure 4.2: Mode of action of the chemotherapy agent etoposide. Topoisomerase II (TOP2, pink) is an enzyme which unwinds the double stranded DNA. By the addition of Etoposide (purple), a covalent complex of DNA and TOP2 is formed, which inhibits TOP2. Further, the re-ligation is inhibited and DNA breaks lead to apoptotic cell death.

ETO belongs to the non-intercalating TOP2 poisons. After 12 years of clinical trials, ETO was approved by the Food and Drug Administration (FDA) in 1983. ETO can

be applied for lung cancer, lymphoma, germ cell tumors, soft tissue sarcomas, ovarian cancer, breast, melanoma and renal cancer either via transfusion (intravenous) or oral, which is then a long-term administration with no need for hospitalization. It was found that an application for 2 h over 5 days is more effective than a continuous application for 24 h, even when the same dose was administered at the end [115]. Thus, the timing of administration is important, since TOP2 is only expressed in cells during selected mitotic cell cycle phases. Standard applications are lung, testicular and melanoma cancer. It was found that etoposide phosphate is less toxic and shows less variability than ETO [115].

Unfortunately, tumor cells develop resistance through alterations or mutations in winding sites of TOP2. Further, slowly growing tumors have less TOP2 due to lower proliferation rates, which makes the therapy with ETO less effective. Also the side effects are tremendous. Healthy cells have not the same uncontrolled growth as cancer cells, but still they divide and thus provide targets for chemotherapy. For example, secondary malignancies and cardiotoxicity are recognized as side effect of ETO. Thus, ETO was frequently used for apoptosis studies in the past [117] and is still an interesting chemotherapeutic model substance, especially to analyze it in a combinatorial chemotherapy approach to overcome the resistance and the side effects.

Network Pharmacology

The 'one-drug one target' therapy revolutionized medicine as single-target drugs offer tremendous effects by triggering one specific check point [118]. However, this monotherapy concept is not applicable for complex diseases such as cancer or pathologies with multiple targets or pathways. Further, deficient efficacy and resistance of cells to chemostatic agents are common reasons for relapse and high mortality rates for some cancer types [118]. Thus, the approach of *combinatorial chemotherapy*, a promising concept to improve efficacy and to overcome resistance as well as side effects and toxicity of anti-neoplastic agents, was established in the 1960s [13]. Novel multi-target mechanisms, in which multiple targets are affected simultaneously, are more effective than single-target drugs - the biological system is seldom able to react to two or more agents with different target sides synchronously. Thus, the efficacy is increased on the one hand, and on the other hand less resistance to the drugs can be developed. To address these two issues, specific drug design has to be considered thoroughly. Network pharmacology, which includes systems biology, network analysis, connectivity, pleiotropy and redundancy, is a powerful strategy for innovative drug discovery by understanding the kinetic and biological characteristics of the drug [119]. Several drug combinations were shown to be more than additive (synergistic) [120]. In summary, to tackle specific diseases by addressing local targets, the whole underlying cellular network, conditioned by the genome, proteome, the environment

and the pathophenome, has to be understood. Barabasi et al. reflect the paradigm of network medicine appropriately: 'Think globally, act locally' [121].

The Chemosensitizer PS89

As explained above, one main problem of cancer therapy is the resistance of cancer cells and the side effects. To overcome this resistance in the case of ETO, a new T8 compound class was developed to increase the vulnerability of cancer cells [122]. For the survival of cancer cells, a balanced homeostasis in the endoplasmic reticulum (ER), which is guaranteed by ER chaperons (assistant proteins for non-covalent folding/unfolding of proteins), is essential. One of such chaperons is the protein disulfide isomerase (PDI), responsible for the reliable folding of proteins in the ER. If the folding is not processed completely, the cell undergoes cell death. Thus, PDI is the perfect target to sensitize cancer cells towards apoptosis. The study highlighted that the PDI inhibition mechanism of the T8 derivatives is based on binding in close proximity of the catalytic center of PDI. The reversible PDI inhibitor T8 family showed dose-dependent increase of apoptosis in leukemia and breast cancer cells in combination with sub-toxic concentrations of ETO. The mode of action was observed to be synergistic and the long-term survival of leukemia cells was suppressed. As the protein synthesis in cancer cells is significantly higher than for healthy cells, non-cancerous cells did not respond to this chemotherapy approach [122]. Within these T8 compounds of PS83-PS89, PS89 (Figure 4.3) showed to be the most sensitizing activity and was thus chosen for further biological and mechanistic investigations [42].

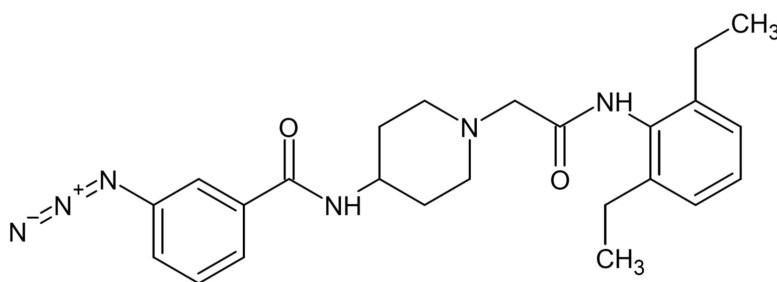


Figure 4.3: The chemical structure of the chemosensitizer PS89.

Signal Transduction induced by Etoposide and the Sensitizer PS89

The pharmacological profile of the combinatorial chemotherapy of the cytostatic ETO and the chemosensitizer PS89 at the ER-mitochondrial interface was established by the group of Prof. Angelika Vollmar (Pharmaceutical Biology) [42].

In short, the apoptotic machinery is initiated by the cleavage of the B-cell receptor associated protein 31 (BAP31), a key communicator in this network of cell death, into p20BAP21. Subsequently, caspase-8 is activated and ER stress is triggered as a consequence. Further, calcium ions are released from the ER in high levels. Accordingly, in the phase of ER-mitochondrial crosstalk, the pro-apoptotic proteins Bak and Bax form oligomeric pore complexes, which lead to the permeabilization of the outer membrane of the mitochondria (MOMP). The breakdown of the mitochondria is accompanied with the release of cytochrome c out of the inter-membrane space. As a result of MOMP, also the level of reactive oxygen species (ROS) increases and again triggers ER-stress and the release of calcium ions out of the ER. With the elevated rate of ROS, the feedback loop of signals in the pathway, triggered by ETO and PS89, is presumably closed.

This target network analysis was revealed with single-cell techniques such as flow cytometry, fluorescence-activated cell sorting (FACS) as well as confocal microscopy accompanied with immunostaining. These powerful tools give a good understanding of key events in the signaling network. However, these methods are limited to end-point readouts, giving just information about selected time points. To follow the whole dynamics of the underlying processes during cell death, for example the evolution of MOMP via opening inter-membrane pores, depolarisation and final breakdown of mitochondria, time-lapse measurements enable the possibility to follow the whole kinetics within the signaling cascades. Furthermore, pair-wise marker correlations pave the way for the analysis of relationships between different events within one and the same cell. In this study, single-cell time-lapse measurements were performed to unravel more details about the effects and timing in signaling cascades of ETO and PS89 as well as pathways triggered by the combination of both, with the focus on the early events MOMP, oxidative burst/increase in ROS level and the endoplasmic release of calcium ions (Figure 4.4). Additionally, triple combinations of markers were realized to give hints about the correlations between the mentioned early events and the final stage of cell death, namely the permeabilization of the plasma membrane.

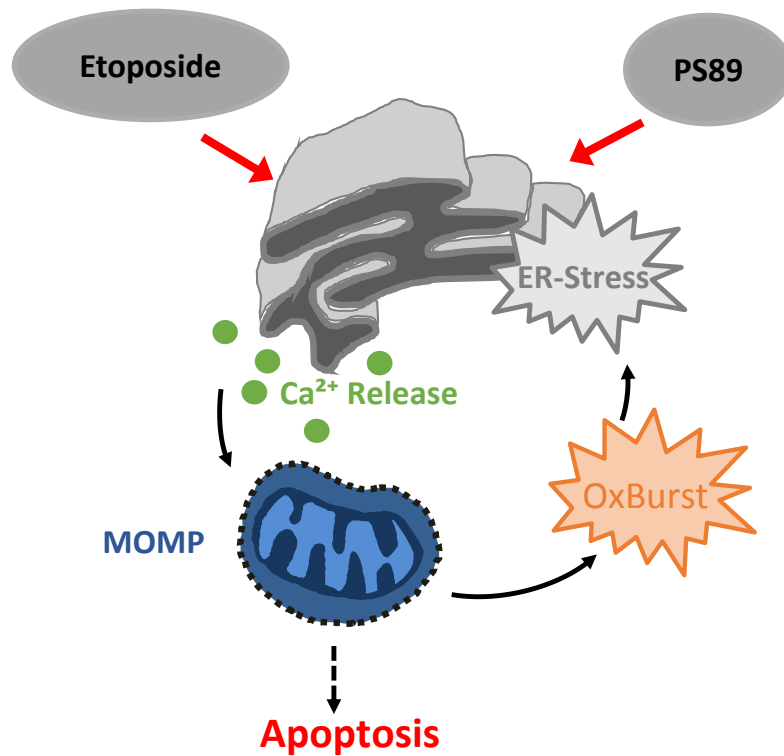


Figure 4.4: Illustration of the hypothetical pathway induced by Etoposide (ETO) and PS89. The combination of ETO and PS89 triggers the endoplasmic reticulum (ER) and a calcium release evolves. This endoplasmic stress leads to the permeabilization of the outer membrane of mitochondria (MOMP). MOMP induces further the increase of the reactive oxygen species (ROS) level and the oxidative burst (OxBurst). The oxygen radicals again provoke ER stress and the feedback loop is likely closed. Finally, the signaling cascade terminates in apoptosis.

4.2 PS89, a Potential Effect Enhancer of Etoposide

4.2.1 Analysis of the Signaling Cascade

High-Throughput Microscopy Method for the Assessment of Single-Cell Time Traces

This project was realized in collaboration with the group of Prof. Vollmar, who analyzed the PS89 target network recently [42]. The aim is now to follow up with these findings and set the focus on the three early events of calcium release, mitochondria membrane permeabilization (MOMP) and ROS levels. The calcium release out of the stressed endoplasmic reticulum was detected with the calcium indicator

Calbryte-520, MOMP via the mitochondrial membrane potential dye TMRM and the reactive oxygen species (ROS) levels were tracked with the oxidative stress agent CellROX orange. More details about the photochemistry and characteristic fluorescence time courses of the staining reagents are given in Chapter 2.4. For this study, A549 lung cancer cells were chosen as model cell line, since ETO is also applied in lung cancer therapy as described above. For the high-throughput assessment of single-cell time traces microstructured arrays were used, which were fabricated with the established technique *Microscale Plasma-Initiated Protein Patterning* (μ PIPP), described in Chapter 2.3.1.

Sequence and Timing of Events in Etoposide and PS89 Induced Apoptosis at the Single-Cell Level

In the work of Koczian et al. the key players in the combinatorial chemotherapy of the chemosensitizer PS89 and the cytostatic ETO were analyzed [42]. The effect enhancement of the chemosensitizer PS89 and time-dependent dose effects were examined with the end point readouts of the cytosolic calcium level, the dissipation of mitochondria and the intracellular ROS level. However, this work was performed with end-point assays in separate experiments. It is therefore interesting to follow the whole dynamics of the underlying processes during the termination of the signaling cascade and set the order of events with the help of time-lapse measurements. So far, the sequence of the key players was adopted from literature and no relations between the key players have been established. Thus, the time-correlations between the events were investigated in this study, to follow the time intervals in which the processes take place.

The temporal evolution of single-cell event times was assessed. In Figure 4.5, the distributions of event times were plotted per exposure. The order of the three markers per column was set by the maxima of the distributions. The maxima, shown with its standard deviation, are gained by fitting a log-normal distribution to the distribution of event times. Note that only the event times of cells are plotted which showed both signals (n) and the data is pooled from different marker combinations. Both, the single PS89 and the ETO exposure, as well as the treatment with the combination of PS89 and ETO showed the sequence of OxBurst, MOMP and calcium release, wherein the maxima of OxBurst and MOMP event time distributions are very close. Hence, the histograms indicate that the calcium release out of the ER is a result of the increase in ROS level and the subsequent depolarisation and permeabilization of the outer mitochondrial membrane. Due to the similarity of the log-normal distribution maxima of the OxBurst and the MOMP events, a close relation of the mitochondrial breakdown and the oxidative burst is evident.

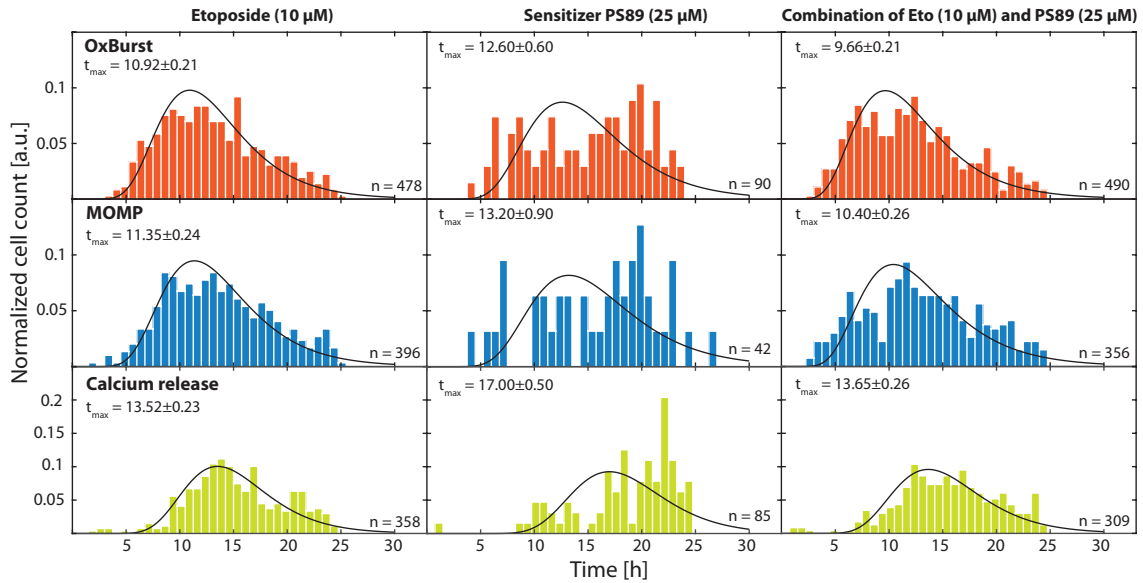


Figure 4.5: Histograms of event time distributions. A549 cells were exposed to Etoposide, PS89 and the combination of both. Event time distributions are shown for OxBurst, MOMP and the calcium release respectively. The maximum of the log-normal distribution is indicated as t_{\max} with its standard deviation. n is the number of shown cells.

However, the average event times are not sufficient enough to determine the exact sequence of events. The relative shifts in the maxima of the event time distributions are too small in comparison to the width of the distributions. Additionally, the log-normal distributions fitted to the event times seem not to reflect the actual distributions. Especially in the case of PS89, where the statistics is quite low due to the marginal cytotoxicity effect of PS89, which causes less double positive cells, the log-normal fits deviate from the event time histograms.

Thus, two-pair correlations of different markers were used to unravel the order of events. In Figure 4.6, a 3x3 scatter plot matrix of event time correlations is shown.

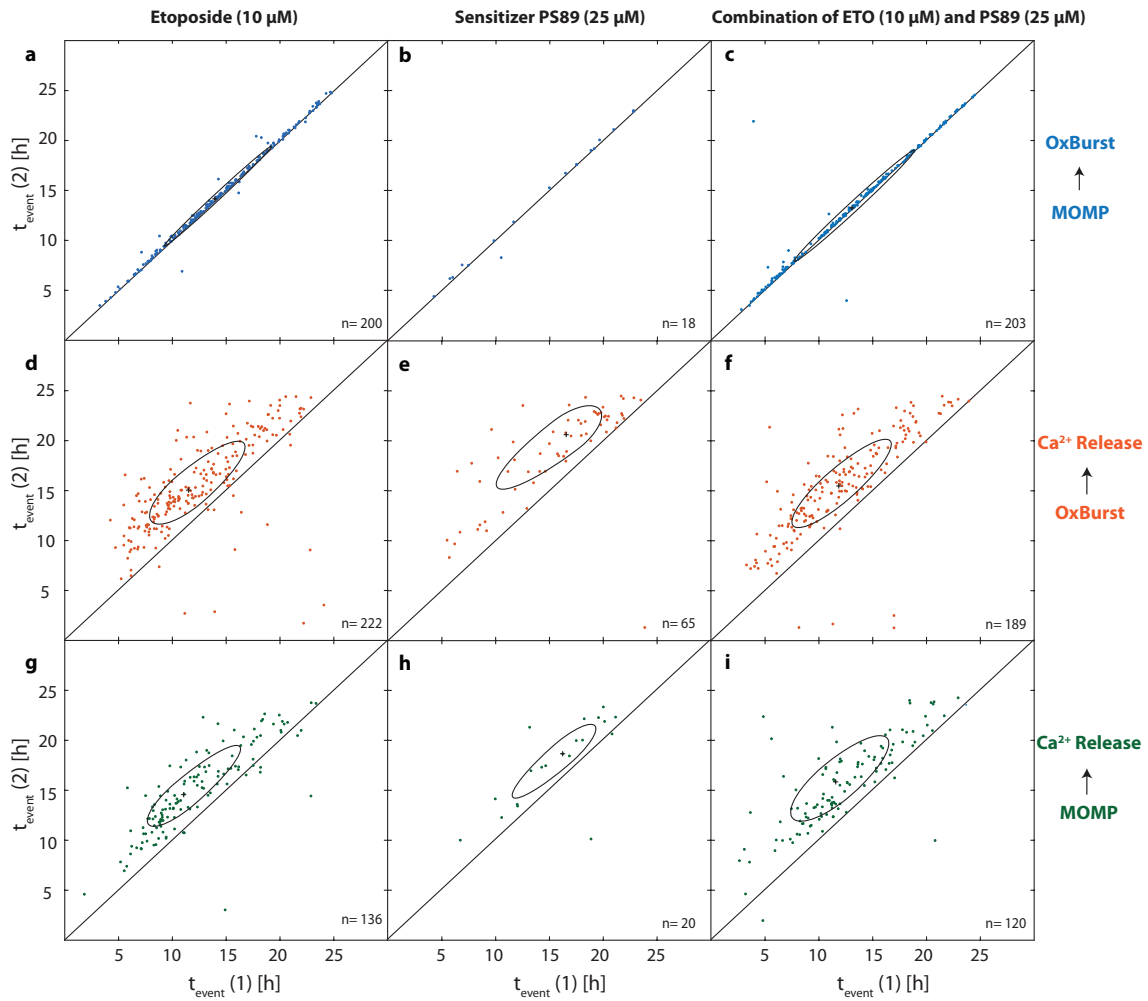


Figure 4.6: Two-dimensional scatter plots of pairwise marker correlation of event times $t_{\text{event}}(1)$ and $t_{\text{event}}(2)$. Apoptosis was triggered with 10 μM ETO (left column), 25 μM PS89 (middle column) or the combination of both (right column). MOMP was correlated with OxBurst (a, b, c) as well as with Ca^{2+} release (d, e, f). Moreover, MOMP and Ca^{2+} release were correlated with each other (g, h, i). n is the number of shown cells.

The exposures, namely Etoposide 10 μM (Figure 4.6a, d, g), PS89 25 μM (Figure 4.6b, e, h) and the combination exposure of both (Figure 4.6c, f, i) are illustrated per column, whereas the different event time correlations MOMP-OxBurst, OxBurst- Ca^{2+} release and OxBurst- Ca^{2+} release are depicted per row. In each scatter plot, the event times of the first marker ($t_{\text{event}}(1)$) are plotted against the event times of the second marker ($t_{\text{event}}(2)$). Every single data point depicts a single cell that showed both events. In this case, the events of the x-axis are the ones labeled in the legend at first (e.g. MOMP in the first row), and the events of the y-axis are the second one of the legend (e.g. OxBurst for the first row). The diagonal is illustrated

as a measure of the location of the ellipses. The *positions* of the clusters, which have been determined by mean shift clustering using an Epanechnikov kernel density, provides the desirable insight into the order of events. The *width and orientation*, which have been determined by Principal Component Analysis (PCA, see details in Chapter 2.5), indicate the strength of the correlation.

Our data shows that in the case of the MOMP-OxBurst correlations, almost all data point are positioned on the diagonal, which means a coincidence of these events. Further, all clusters of the scatter plots of MOMP- Ca^{2+} release and OxBurst- Ca^{2+} release correlations are located above the diagonal. This means that the second event ($t_{\text{event}}(2)$) follows the first event ($t_{\text{event}}(1)$).

In summary, our results of the two pair-correlation of events show the sequence of **MOMP-OxBurst- Ca^{2+} release** (Figure 4.7), whereas MOMP and OxBurst are correlated so closely that one can assume that these two events occur almost at the same time. These outcomes are in good agreement with the results of Koczian et al., who assumed the same order of events [42]. In addition, they proposed that the Ca^{2+} release triggers MOMP, whereas we did not see the cluster of events for Ca^{2+} release-MOMP. So far, no conclusive reason for the absence of the cluster is found.

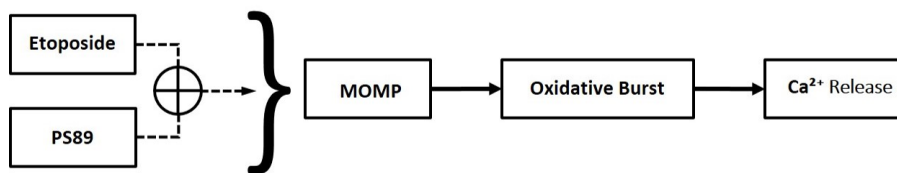


Figure 4.7: Signaling cascade induced by ETO and PS89 as well as for the combination of both was found to be MOMP - oxidative Burst - calcium release in A549 cells.

Further, a significant effect enhancement of ETO triggered by the chemosensitizer PS89 was detected for the different end-point readouts in Koczian et al. [42]. In detail, the combination of ETO and the chemosensitizer PS89 induces significantly higher cytosolic Ca^{2+} concentrations in Jurkat cells, illustrated by increased Cal-520 fluorescence, than for the ETO or PS89 single exposure. Further, when analyzing the mitochondrial damage, a PS89 mediated amplification in mitochondrial apoptosis was recorded in combi treated cells in comparison to the single ETO exposure. Moreover, the intracellular ROS level, the third apoptosis indicator analyzed there, was increased with the combinatorial treatment and even higher levels were gained after 48 h. The outcomes of the PS89 single treatment were comparable to the negative control in all three readouts.

Accordingly, our results are shown in Table 4.1. The percentage of cells with double positive signals for the combinations MOMP-OxBurst, MOMP- Ca^{2+} release and

OxBurst- Ca^{2+} release in all three exposures (ETO, PS89 and Combi) was analyzed. In agreement with Koczian et al. [42], the effect of the PS89 single treatment is negligible low (max. 12%) and comparable to the negative controls (between 1% and 6% in different marker combinations). Further, we see a slight increase in effect with the combination treatment (9%, 1%, 5%) in comparison to the ETO single treatment, which indicates the chemosensitizing effect of PS89. Similarly, the flow cytometry results show a minor increase of cytosolic calcium level and ROS level after 24 incubation by the additional administration of PS89 with ETO. The doubling of dissipated mitochondria from 10% to over 20% could not be observed directly, due to the fact that we only analyze cells with both the MOMP and the OxBurst or the Ca^{2+} release signal. Furthermore, the different cell line (Jurkat vs A549) can cause slight differences.

Marker Combi/Exposure	ETO	PS89	Combi
MOMP-OxBurst	32%	3%	41%
MOMP- Ca^{2+} release	30%	5%	31%
OxBurst- Ca^{2+} release	30%	12%	35%

Table 4.1: Analysis of PS89 Effect Enhancement. The percentage of cells with double positive fluorescence signal is shown for each exposure and the three marker combinations MOMP-OxBurst, OxBurst- Ca^{2+} release and OxBurst- Ca^{2+} release.

Besides the combi effect, also a time-dependent effect was recognized by flow cytometry and the calcium level increased especially after 48 h compared to 24 h. Also the number of cells with dissipated membrane potential was almost as triple as high after 48 h of incubation than for the 24 h incubation. Additionally, the intracellular ROS level was observed to be elevated for ETO after 48 h exposure compared to 24 h [42].

In contrast, the single-cell event time correlations provide a more differentiated output (Table 4.2). The centers of the clusters, which are shown as crosses in the ellipses of the scatter plots in Figure 4.6, depict the average timing of the event times (shown with its standard deviation). In comparison, the centers of the first as well as of the second cluster of ETO and combi treated cells are similar, whereas the centers of the event times of PS89 exposed cells are shifted to later time points, which is in agreement with the fact that PS89 alone is not harmful to the cells (see Table 4.1., low percentage of double positive cells). The center of the event times for the correlation between MOMP-OxBurst in PS89 treated cells is not available (n.a.), as the event times are scattered along the whole diagonal and only low statistics are available.

Furthermore, the delay times between the two correlated markers are examined (last column, (Δt in hours)). For the correlation between MOMP-OxBurst, very short delay times (< 1 h) were calculated for both ETO and combi treated cells. This quantification supports the narrow ellipses of event times directly on the diagonal of the scatter plots and the assumption that MOMP and the oxidative burst are closely related and occur almost coincidentally. Accordingly the fact that the centers

of the makers for ETO and combi treated cells are similar, also the delay times are comparable. Also the fact that the delay times for the correlations MOMP-Ca²⁺ release and OxBurst-Ca²⁺ release are very close to each other (for ETO) and analogical (for the combi), is another strong argument for the coincidence of MOMP and OxBurst.

ETO 10 μ M	Center of 1 st M. [h]	Center of 2 nd Marker [h]	Δ t [h]
MOMP-OxBurst	13.86 \pm 0.35	14.10 \pm 0.35	0.24 \pm 0.49
MOMP-Ca ²⁺ release	11.11 \pm 0.38	14.58 \pm 0.35	3.47 \pm 0.52
OxBurst-Ca ²⁺ release	11.50 \pm 0.30	14.97 \pm 0.28	3.47 \pm 0.41
PS89 25 μ M	Center of 1 st M. [h]	Center of 2 nd Marker [h]	Δ t [h]
MOMP-OxBurst	n.a.	n.a.	n.a.
MOMP-Ca ²⁺ release	16.32 \pm 0.96	18.62 \pm 0.90	2.3 \pm 1.32
OxBurst-Ca ²⁺ release	16.52 \pm 0.63	20.57 \pm 0.53	4.05 \pm 0.82
Combi	Center of 1 st M. [h]	Center of 2 nd Marker [h]	Δ t [h]
MOMP-OxBurst	13.12 \pm 0.39	13.25 \pm 0.39	0.13 \pm 0.55
MOMP-Ca ²⁺ release	11.85 \pm 0.42	15.77 \pm 0.39	3.92 \pm 0.57
OxBurst-Ca ²⁺ release	11.86 \pm 0.34	15.45 \pm 0.33	3.59 \pm 0.47

Table 4.2: Analysis of PS89 time-dependent effect enhancement. The centers of the first and the second marker (M.) with standard deviation in hours are tabulated for ETO, PS89 and the combination of both (Combi) for the three marker combinations MOMP-OxBurst, MOMP-Ca²⁺ release and OxBurst-Ca²⁺ release. The delay times with the standard deviation in hours between the two centers are depicted in the last column (Δ t). n.a. = not available.

Depolarisation Lag Time of Mitochondria

The mitochondrial membrane permeabilization due to the opening of inter membrane pores is a consequence of mitochondrial depolarisation. As described in Chapter 2.4.2, a peak was observed for the time traces of ETO, PS89 and the combination of both. The maximum of the peak was set as the time point of the beginning of the depolarisation, which is assumed to be described in the subsequent decay of fluorescent intensity. As additional information, the time delay between the maximum of the peak ($t_{\text{Depolarisation}}$) and the breakdown in intensity (t_{MOMP}) was analyzed to examine the lag time of depolarisation.

In Figure 4.8, the histograms of the depolarisation lag time are shown for the three exposures ETO (Figure 4.8a), PS89 (Figure 4.8b) and the combinatorial therapy of both (Figure 4.8c). As expected, the highest mean lag time of depolarisation was recorded for the chemosensitizer PS89 (Mean = 11.5 \pm 6.9 h), since also no major effects of single PS89 treatment were detected in the correlation analysis. Further, cells treated with ETO show mostly a lag time between 0-12 hours with a mean lag time of 8.3 \pm 5.7 h, while the mean lag time for cells exposed to the combination treatment is shifted to later time points (Mean = 10.0 \pm 5.9 h).

The reduction in lag time of depolarization, thus decreasing the time between the beginning of depolarisation and final mitochondrial breakdown, would lead to earlier cell death and could help to increase the efficacy of drug treatment.

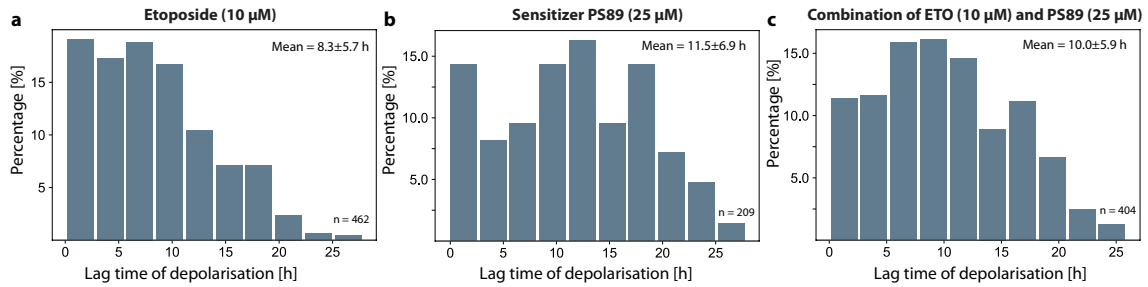


Figure 4.8: Lag time of depolarisation analysis. The distributions of time delays between the activation of depolarisation ($t_{\text{Depolarisation}}$) and mitochondria membrane permeabilization and breakdown (t_{MOMP}) is shown in the histograms for ETO (a), PS89 (b) and the combination of both (c).

4.2.2 Quantitative Noise Analysis of Heterogeneity in Cell Response

Noise in biological context describes the variability in data when experiments are reproduced or a background signal interferes with the desired signal [123]. However, in biological systems random noise can be beneficial, since it leads to an increase in signal transmission and is thus a 'noise benefit'. An intermediate noise magnitude provides an optimal performance. This phenomenon is defined as *stochastic resonance* [123]. Further, noise is essential for mutation and evolution to ensure individuality of cells [124]. Moreover, cell fate decisions and population heterogeneity are noise-driven processes. Nevertheless, Rao et al. stated that also heterogeneous processes need order in a certain way; if a cell fate decision is done, the down-stream signaling is strictly regulated [124]. But how the order emerges from disorder remains still a triggering question.

Non-genetic heterogeneity in cell response can have two causes, the intrinsic and the extrinsic noise [16, 125]. The intrinsic noise is caused by molecular fluctuations and can be modeled with stochastic methods [124, 125]. Intrinsic noise can be moderated by negative and integral feedback loops, gene dosage, parallel cascades and regulatory checkpoints ensuring the completeness of the separate steps before proceeding with the signaling pathways [124]. Extrinsic noise can arise from external factors [125] and is intracellular uniform but shows varieties between cells [7].

Apoptosis shows often cell-to-cell-heterogeneity and heterogeneity in response. Single-cell measurements enable to follow noise directly and are key to analyze heterogeneous responses [126]. Thus, to guarantee a high quality of the single-cell data from which reliable statements can be drawn, a careful data analysis as well as thorough noise analysis (cell-to-cell-variability) is essential. Despite the very clear order of events, which was revealed with the definite clusters of correlated events in the scatter plot analysis, the data gives more information. Not only the signals which

were shown are interesting, also one can challenge the data why some cells did not response. In particular, during data analysis it was recognized that a considerable percentage of cells did not show any signal or only the one or the other signal. Thus, the following questions popped up: How many cells showed just the one or the other signal? Is there a mechanism or a scheme behind these signal patterns why only the one or the other marker is shown? Can we find a biological reason for this? In the following, these questions were attempted to answer with the single-cell data.

The analysis of the heterogeneous response of the cells revealed that in average around 50% of the cells treated with ETO in single and combi treatment showed no signal at all. These results are in good agreement with the outcomes of Koczian et al., who showed for three different cell lines an increase of the apoptosis rate up to 40-50% by the combination of different chemotherapeutics with PS89 [42]. The PS89 single treated cells evinced in average 82% no signal, which was expected, since the chemosensitizer should have no effect, comparable to the negative control [42].

In Figure 4.9, an exemplary pie chart of heterogeneous response is depicted. The cells were treated with the combination therapy and the events MOMP and OxBurst were correlated. Almost half of the cells show no signals (gray), while only a small portion of cells is present, which showed only the one or the other marker. Additionally, around 3% show the order OxBurst-MOMP, but almost 40% (38.6%) shows the preferential sequence MOMP-OxBurst. The cells with the sequence OxBurst-MOMP are assumed to be detected falsely in the analysis.

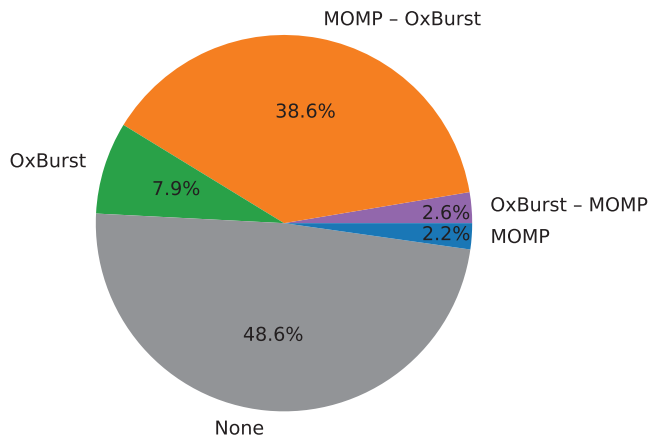


Figure 4.9: Exemplary pie chart of the division in cellular response in the MOMP-OxBurst correlation, measured in A549 cells after treatment with 10 μ M ETO and 25 μ M PS89.

To evaluate the reason for the high no-signal response, single-cell traces were screened thoroughly. Heterogeneity and ambiguity were recognized in the fluorescence traces and limit the possible accuracy of the fitting routine used before. Thus, the MOMP and OxBurst data is fitted with the interactive fitting (see Chapter 2.5.2). Hence,

an higher quality and accuracy of the event time determination is given and false positive or false negative event times negligible. But still, the data is challenging to analyze. In fact, there may be several reasons for the 'low' susceptibility of the cells to the combinatorial chemotherapy. First, the cells can be resistant to a certain extent, and thus show no apoptotic signaling [127]. Second, the observation period of 24 h could be too short, since a evident increase in response was recorded after 48 h in the case of Jurkat cells [42]. For a closer assessment of this parameter, further experiments for over 48 h should be performed. Moreover, the responsiveness to an apoptotic inducer varies from cell line to cell line. Further, the concentrations of the markers are low due to the fact that the marker are in the medium for the whole experiment, but still in a sufficient range. Thus, the missing signals should not be caused by lacking fluorescence marker molecules. Additionally, the effect of ETO was found to be highly dose and time schedule dependent [128]. In accordance to this, the low concentration of etoposide could be the reason for the moderate response value, but on the one hand, the concentration of chemostatics should be kept as low as possible due to the side effects in the patient. And on the other hand higher concentrations of ETO favor the detachment of the cells off the microstructured surface. A lower concentration of ETO was tested (2.5 μM , data not shown) and with the now used concentration of 10 μM already an increase in detachment of cells was recognized. With a further increase in concentration even more cells would come off presumably.

In conclusion, the three questions asked before can be answered with the following achievements: The number of cells with double or only single response could be quantified and analyzed in detail, which is not possible with end-point bulk measurements. The percentage of cells, which show only the one or the other marker is not higher than 30% in all conditions. Interestingly, the number of cells, which show no signal is in the same range for ETO as well as for Combi treated cells, which was expected to differ from each other (a higher impact of the combination was assumed). The biological reason for this behavior could be the low concentration of ETO (10 μM) and an interplay with potential resistance of the A549 lung cancer cell line. For further experiments, the most promising approach to increase the percentage of cells, which response to the combination of ETO and PS89, would be to increase the time of administration up to 48 h.

In addition to this, the data was scrutinized more precisely in terms of differences in single and double signals given by the cells for the the first analysis of the effect enhancement of PS89 (Chapter 4.2.1) and the calculation of the Bliss level (next Chapter 4.2.4). In Figure 4.10, one exemplary distribution is shown for the marker combination OxBurst- Ca^{2+} release. The A549 cells were treated with the chemosensitizer PS89 and the event times per marker were plotted. The upper panel shows the OxBurst events and the bottom panel the ones for the Ca^{2+} release. The bins in orange show cells, which demonstrated both signals, the blue bins illustrate cells with only the OxBurst events and the green columns depict cells with only the Ca^{2+}

release signal. By comparison of the upper and the bottom panel it is observable that for the OxBurst event it makes no significant difference if the cells showed both signals or only one signal. However, for the Ca^{2+} release, the gap in response is significant between double and single responses. While the distribution of only Ca^{2+} release events shows most events between 0-5 hours, the cells which showed both events are shifted to later time points (around 20 h).

Due to this differences in response, the more restrict criteria was chosen that only double positive cells were taken for the effect analysis as well as for the determination of the Bliss level.

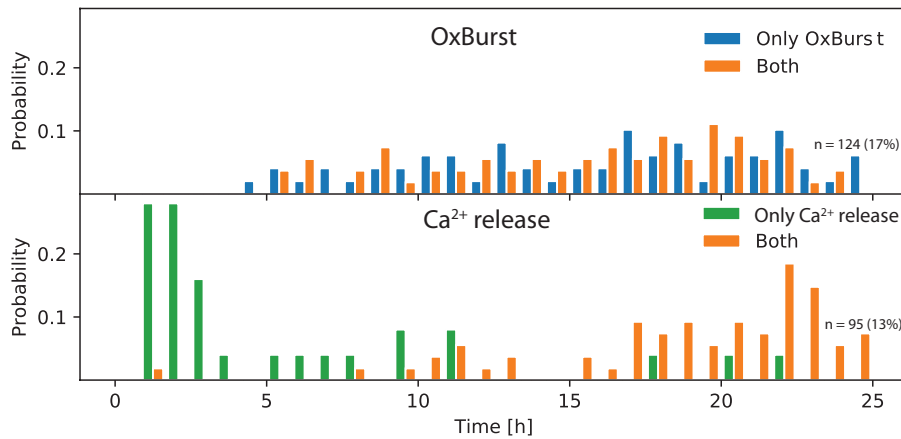


Figure 4.10: Exemplary distribution of event times for the combination OxBurst-Calcium release in PS89 treated cells. While the OxBurst marker (CellROX) shows negligible differences in response between cells with only the OxBurst signal and cells with both signals, the Calcium indicator (Calbryte-520) shows significant differences in single and double response. While the distribution of both signals is shifted to later time points (around 20 h), the calcium events only show most events at earlier time points (0-10 h).

4.2.3 The Distribution Function of Delay Times

Next to the distribution of event times, the distribution of the delay times between the events was analyzed. It is assumed that the signaling cascade is a chain of stochastic events and the events are happening consecutively and independent, thus we can fit the distributions of delay times with gamma functions. The distribution of the total event chain is the convolution of the partial chain events. More details can be found in Chapter 3.8.

In Figure 4.11, the distribution of delay times (orange) is shown with the fitted gamma distributions (blue lines) for ETO, PS89 and the combination of both (per column). The marker combinations MOMP-OxBurst, OxBurst- Ca^{2+} release and MOMP- Ca^{2+} release are illustrated per row.

A strong correlation between MOMP and OxBurst has been discovered. In all three

exposures, MOMP and OxBurst happen nearly simultaneously, MOMP leading for only a few minutes (median ≈ 0.2 hours). However, the median of delay times for OxBurst- Ca^{2+} release is slightly higher in each exposure than the median for MOMP- Ca^{2+} release. This was not expected since the sum of delay times between MOMP-OxBurst and OxBurst- Ca^{2+} release should be the delay time of MOMP- Ca^{2+} release or even higher than the sum. As explanation, the ambiguity of the time traces can cause inconsistency during the interactive fitting. In detail, the fluorescence traces of different markers have been analyzed independently. If the event time of one marker was ambiguous, the earliest event time was chosen. However, this determination might cause shifts in timing, if the event time could not be detected correctly. Even if the interactive fitting increased the accuracy and quality of the event time detection tremendously, especially the OxBurst time traces remain challenging to analyze. Probably Machine Learning is a good approach to tackle this problem, which is discussed in the Outlook Chapter 6.2.

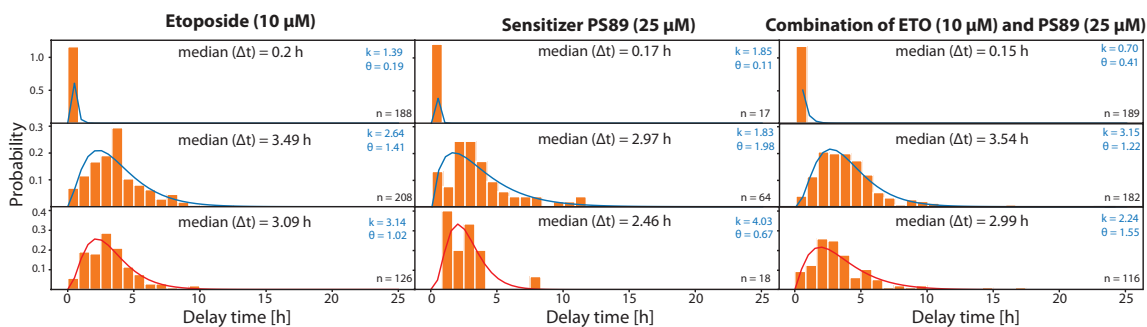


Figure 4.11: Gamma fits to distributions of delay time evolution in Etoposide, PS89 and combination treated A549 cells. The measured orange histograms show the distribution of time delays (in h) for the combinations MOMP-OxBurst, OxBurst- Ca^{2+} release and MOMP- Ca^{2+} release. The blue lines depict the gamma distribution fits. The estimated parameters k and θ of the gamma distributions, n as the number of single cells and the calculated mean values of the gamma distributions are indicated. In this case, the mean time delays of the two sub-pathways (first and second row) do not sum up to their concatenations (third row).

4.2.4 Quantitative Evaluation of Synergistic Effects of PS89

Chemosensitizers such as PS89 are developed to increase the effect of the cytostatic, which is given in combination with the chemosensitizer. In best case, the effect of the combination is higher than only the sum of both (additive effect). If the effect is more than additive, a so called *synergy* is given for the two combined drugs.

This statistic (in)dependence test for the description of two drugs, which have different target sites and different mechanisms of action, was described first by C. I. Bliss in 1939 [129]. Accordingly, the combined effect P_{12} of independent drugs in

a specific effective concentration with effects P_1 and P_2 can be calculated with the following equation:

$$P_{12} = \frac{P_{1+2}}{P_1 + P_2 - P_1P_2}$$

where P_{1+2} is the measured effect of the combination. Is P_{12} more than one, the combined effect of the two agents is synergistic. When P_{12} is one, the variables are independent and the effect is additive. The two combined drugs are antagonists, if P_{12} is less than one.

In our work, the percentage of double positive cells (of total cells) for the marker combinations MOMP-OxBurst, OxBurst- Ca^{2+} release and MOMP- Ca^{2+} release were tested for synergy. While the combination of ETO and PS89 in the correlations of OxBurst- Ca^{2+} release and MOMP- Ca^{2+} release indicate no synergistic effects (0.93 and 0.91), synergy was presumably detected for the MOMP-OxBurst correlation (1.2 > 1). When testing the synergy for a late marker combination, OxBurst-PMP, a synergistic effect might be determined (1.7). Note that the outcomes of the Bliss independence test can vary depending on the readout parameter. The group of Prof. Vollmar found synergistic effects in the combination therapy for the readouts ROS level, cytosolic calcium level and dissipated mitochondria membrane potential. The cell death assay where the PMP is detected as indicator for apoptosis showed synergy for the combination treatment, as our results did.

Next to the Bliss level calculated with the percentage of double positive cells, a dynamic Bliss level was analyzed. Therefore, a kernel density of the event time distributions was compared to a dynamic Bliss level. The Bliss level was calculated for each time point separately. In Figure 4.12, the event time distributions (histograms) for the three events MOMP, OxBurst and Ca^{2+} release are plotted with the kernel density (black line) and the Bliss independence level (black dashed line) for the combination. By comparison of these two fits, no synergy was evident.

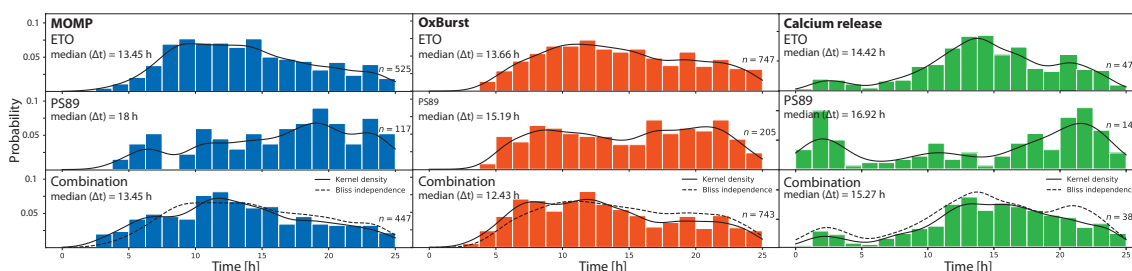


Figure 4.12: Dynamic Bliss Analysis of the events MOMP, OxBurst and Ca^{2+} release for ETO, PS89 and combi treated A549 cells. The event times were pooled from the correlations MOMP-OxBurst, OxBurst- Ca^{2+} release and MOMP- Ca^{2+} release. By comparison of the kernel density (black line) and the Bliss level (black dashed line), no obvious synergistic effects were indicated.

Further, the last event in the apoptosis signaling cascade, the plasma membrane permeabilization (PMP) was analyzed. In Figure 4.13, the kernel density distribution (black line) and the Bliss level of the event time distributions (black dashed line) for PMP are shown. For the combination, a slight shift of the calculated Bliss level to later time points in comparison to the kernel density is recognized. This shift could indicate a synergistic effect of the chemosensitizer PS89 in combination with ETO. In summary, we could analyze the Bliss independence in a quantitative as well as in a dynamic way for better understanding of the drug synergy between ETO and PS89. The data indicates synergistic effects in some marker correlations. The assessment of the effect dependence of two drugs was shown to hinge on the analyzed event.

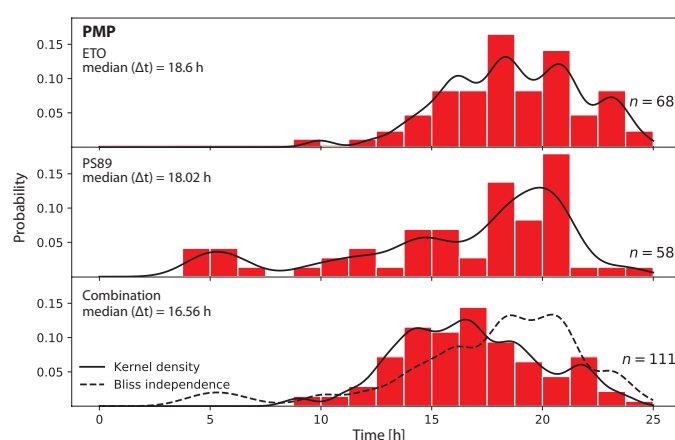


Figure 4.13: Dynamic Bliss Analysis of the plasma membrane permeabilization (PMP) for ETO, PS89 and combi treated A549 cells. The PMP event times were received from PMP-OxBurst correlations. The Bliss level (black dashed line) shows a shift to later time points than the measured kernel density (black line), indicating presumably synergy.

4.2.5 Triple Marker Correlations

So far, linear signaling pathways were investigated with the help of pairwise marker combinations. Therefore, two markers were added to the cell and the order of two events can be determined. Further, with the examination of different double correlations the whole cascade of the correlated events can be composed. However, for the estimation of crosstalk or a network of signals, the parallel tracking of more than two markers is essential. If one could analyze three or more markers per cell at the same time, more information about the fate decisions, the cell has to make during apoptosis, could be gained. Moreover, multiple correlations could finally lead to information about causation. If, for example, three markers are measured and the cell shows one signal only with the one but not with the other signal beforehand, this could mean that the following signal is induced by the one signal. For instance, one

could image the following hypothetical example: the cell is not dying, thus showing no plasma membrane permeabilization (PMP) and the oxidative burst is occurring, but not the calcium release. But if the cell shows both signals, the oxidative burst and the calcium release, the cell is dying (positive PMP signal). Thus, cell death is a result of the combination of the calcium release and the oxidative burst. Such indication about causation, thus information beyond correlations, would further help for specific targeting key players in the cell death signaling cascade. Mostly, not only one key event is responsible for the final cell death, but the interaction between the apoptosis actors.

Therefore, three markers were added to A549 cells to investigate the network signaling. In addition to the marker combinations already measured before, the cell death indicator Toto-3 Iodide was supplemented. All other experimental conditions were kept as for the measurements before. The negative controls (markers only, no apoptosis inducer), which were performed in each experiment, were as low as for double correlations (between 0-4%) and also cell morphology was not different. Thus, negative effects or influence due to an overload of fluorescence markers can be excluded. All three markers were used in such low concentrations that they are not harmful to the cells, even when they were kept in the media for the whole measurement without a washing step.

Interestingly, the main section of cells showed no signal at all. For the ETO treated cell in average 54%, for PS89 exposed cells 80%, and for the cells treated with the combination of both in average 56% showed no signal. In all three triple marker combinations (MOMP-OxBurst-PMP, OxBurst-Ca²⁺ release-PMP and MOMP-Ca²⁺ release-PMP) the rest of the cells show a broad and almost even distribution with only one or two of three signals. In the same range the cells show all three signals, thus a very low amount (5-16%). The low percentage of triple signals and the high amount of cells with no signal can be due to resistance of the A549 cells and the low concentration of ETO, as discussed for the double marker correlations.

Moreover, the A549 cells show only for the MOMP-OxBurst-PMP correlation a higher percentage of triple signals for the combination treatment than for ETO alone (Figure 4.14a). For the other two correlations (OxBurst-Ca²⁺ release-PMP and MOMP-Ca²⁺ release-PMP), the effect for the combination exposure of ETO and PS89 was lower than for ETO only (Figure 4.14b and c). Further investigations would be necessary to clarify the cause of the depressed effect in the combination.

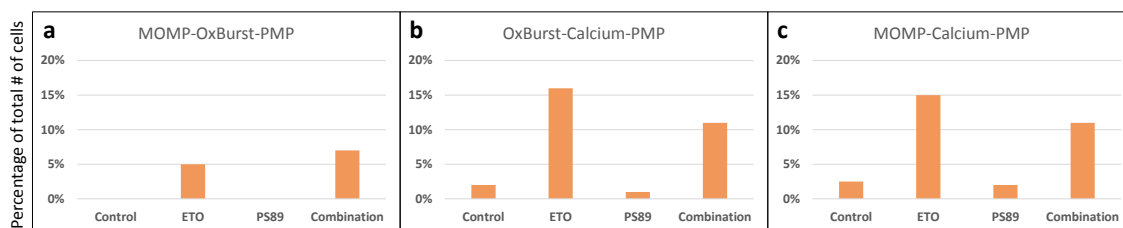


Figure 4.14: Analysis of triple combinations. Double positive cells plotted per exposure: negative control, Etoposide (ETO), PS89 and the combination of both.

This first attempt of triple correlations was technically performed successfully, since some cells did show all three signals. However, further investigations with different marker combinations have to be carried out to gain more insight about the signaling network. For example, triple correlations with a higher ETO concentration over a longer period (e.g. 48 h) could be measured to examine whether the low percentage of triple signals is limited due to the measurement interval of 24 h or the low concentration of ETO. Further, another late marker, such as pSIVA-IANBD, could be used to examine which events or event combinations are leading to cell death.

4.3 Discussion and Outlook

In summary, our results of the two pair-correlations of events showed the sequence of **MOMP-OxBurst- Ca^{2+}** , which is in good agreement with the findings of Koczian et al. [42] as well as literature: the connection between Ca^{2+} levels, mitochondria and ROS during apoptosis was reported frequently [45, 130–133]. For example, Rizzuto and co-authors described that waves of mitochondrial Ca^{2+} control cell fate [134]. Further, they report that apoptosis might be triggered by non-physiological concentrations of intracellular Ca^{2+} by opening the permeability transition pores of the highly transport regulated inner membrane of mitochondria (see Figure 2.6). Calcium was reported to be the messenger of the crosstalk between the ER and the mitochondria [135]. Further, ROS may induce unbalanced redox and triggers the unfolded protein response (UPR) [136], supporting our result of the correlation between ROS and Ca^{2+} release, which is an indirect consequence of UPR and ER stress.

The order of events published in Koczian et al. were assumed on the base of literature, but the actual sequence of events could not be determined with the endpoint readouts of the different approaches (e.g flow cytometry) [42]. With single-cell time-lapse measurements, we succeeded to determine the definite order of events and record the delay times between the events. However, the increase in effect enhance-

ment was not as evident as for Koczian et al. [42], which could be due to the pair-wise readout.

In future, the time dependent effects arising after 24 h seen in Jurkat cells, could be assessed with 48 h time-lapse measurements to analyze whether the steep effect increase also shows up after 48 h in the single-cell setup.

Also, the events leading compulsorily to cell death are intriguing to study. Triple correlations between events could help to understand direct relationships, in the direction of causal relations. Thus, triple measurements with a different endpoint marker than Toto-3 Iodide, e.g. pSIVA-IANBD, could help to gain further insight in the signaling networks. Consequently, the specification of key players, which are directly responsible for the absolute induction of apoptosis pathways as well as the establishment of cause-and-effect-relationships are providing new target sides and possibilities for innovative chemotherapeutic approaches.

Furthermore, the analysis of functional correlations could improve the investigation of the dependency of the events. Then, the Bliss level could be calculated from more quantitative valuables. So far, the Bliss level was examined with the percentage of double positive cells or the dynamic course of the event times probability.

In future, the Area Under the Curve (AUC) of a calcium marker time courses as well as the slope of the OxBurst time traces could be correlated with the event times of MOMP, OxBurst and Ca^{2+} release, respectively. The AUC could give a hint on the amount of the released calcium out of the stressed endoplasmic reticulum and would be a more quantitative parameter than the event time of Ca^{2+} release. Note, that for a quantitative analysis, a ratiometric (dual-wavelength) fluorescence marker has to be used rather than the single-wavelength calcium indicator Calbryte-520. The marker used in this study is only suitable for the detection of relative calcium concentration changes, not for a quantitative analysis.

Further, the slope of the fluorescence intensity in the OxBurst time traces, which correlates presumably with the ROS rate, could be analyzed. Both parameters are probably more suitable for the calculation of the quantitative Bliss level than the percentage of double positive cells.

Chapter 5

Investigation of a 3D Environment For Single-cell Applications

5.1 State of the Art

In times of personalized medicine and personalized health care the importance of high-throughput methods and platforms, where hundreds to thousands of cells can be observed in parallel to test different combinations of drugs or administration time intervals with a low volume of test sample, is significantly increasing. Especially for stem cell research, where the access or availability of samples is strongly limited, the miniaturization and dense packaging of test arrays, so called *microwells*, is an urgent need. Furthermore, the observation of a high number of single-cells in parallel has gained more interest in the last decade, since the heterogeneity in cellular response and the presence of sub-populations was recognized. So both, cell-based and single-cell chip research grew in the last years, indicated by sextubled number of publications within 6 years (2002-2008, [27]). Therefore, high statistics, gained with such arrays, are inevitable for reliable and reproducible results. Some researchers had set the number of 10 000 cells, which have to be observed for credible statements and up to 1000 cells for the development of general single-cell arrays [27]. Further, a dense packed and miniaturized array has the advantage of automated analysis. In consequence, in 2006 the term *Lab-on-a-chip*, the idea of a small lab on a chip with all needed instrumentation's for the whole workflow, was established by the group of Manz [137]. Meanwhile, a own field of research with it's own journal, named also Lab-on-a-chip, with thousands of applications, not only biological implementations, has developed.

Various assays can be performed on such cell-based arrays: culturing, adhesion, migration, electroporation, separation, protein-localization, live cell imaging, drug screening, sorting, patterning, trapping, transfection, lysis etc [27]. Microwells, one can say the successful miniaturization of standard microwell plates, can be designed for single cells in a size of roughly double the cell size (30-50 μm to 100 μm), to observe for example cell fate, proliferation, drug response, cytotoxicity etc. Or, the microwells are in the range of a few hundreds of μm (200-500 μm) to host more than one cell, to study for example cell-to-cell communication or spheroid formation.

Microwells can be used for adherent cells, but especially for non-adherent cells, the local confinement is beneficial for observing and tracking single cells, since otherwise they diffuse out of the field of view during the experiment. Additionally, no further coating or surface treatment is required, which is essential for most adherent cell lines. Next to the size, also the height of the microwell walls has to be considered. When cells are observed over days, a sufficient supply with media has to be guaranteed. Thus, higher walls for more volume or a volume of media, which covers all wells above, has to be considered. Note, that the exchange of media with the above basin is not fully guaranteed with the combination of very high walls and narrow wells. Furthermore, depending on the size of the microwells, the seeding density is determining the occupancy of all wells. Additionally, the seeding density depends on the intention of single or multiple occupancy per single well. Cells are usually seeded in solution, and after some incubation time, where the cells can settle down to the bottom of the wells by gravity, the wells are washed to remove extensive cells, which have not sedimented, and probably another seeding step is performed to adjust the number of cells. Technically, an overall occupancy of around 70% would be desirable, to make the data analysis be worth it. In fact, studies have shown that the single occupancy of microwells follows a Poisson distribution and only around 30-40% of the microwells are occupied with a single cell [138].

Furthermore, it is a note worth to say that not all cell lines are suitable for the use of microwells. In the course of this work, the human T cell leukemia Jurkat cell line was tested, which would have been the perfect model system for the combinatorial chemotherapy project with Etoposide and the sensitizer PS89 (Chapter 4). But, even though several materials, sizes and coatings were tested, the non-adherent Jurkat cells were all dead at the end of the experiments, the latest after 48 h of incubation with only media in microwells. In short, Jurkats were incubated in PEG-DA microwells (35 and 50 μm length) or PEG-DA trenches (120 μm length), a setup, which has already been used for other studies [139–141] with (microwells) and without fibronectin (FN) coating (trenches and microwells). Fibronectin, an adhesive extracellular matrix protein, should in principle increase the biocompatibility to the surface. Furthermore, in-house made liquid glass microwells (with and without FN coating) were checked for cell survival. In addition, Jurkat cells were seeded in in-house made PDMS microwells (35x35 and 50x50 μm squares), which were also coated with FN or not. In summary, nine different conditions were measured with the help of time-lapse experiments for at least 24 h and mostly with the CellROX marker green, indicating cellular stress and the PI marker, which illustrates cell death by plasma membrane permeabilization. The intracellular stress signal was in most of the experiments visible (or rather the breakdown in intensity showing oxidative burst) and the PI signal was evident in most cases at the end of the experiment. In the best case only 11% of cells were dead after 48 h, but not in a reproducible manner. The results show that neither the material, nor the size were the cause of cytotoxicity. Also the coating with FN could not avoid cell death. Further, the access

and supply with media and nutrients was guaranteed, due to testing the structures in different sizes and setups such as dishes or 8-well slides. In the end, we came to the conclusion, that this type of cell line is not suitable for a confinement in microwells. The cause of cell death could be microinjuries, induced by hitting the walls during stage movement, mechanical stress through the confinement itself (both necrotic cell death) or chemical secretion of stress or cell death signals, which are additionally accumulating in the confined environment (apoptosis). No correlation between single occupied or multiple occupied wells could be observed, both conditions were leading to cell death. One could explain these outcomes of limited viability of single Jurkat cells in a microwell with the fact that Jurkat cells have the tendency to aggregate in healthy cell cultures (see pictures in the Appendix of standard protocols A.1). If neighboring cells are missing in single occupied wells or the neighbor cells are too far away in bigger microwells, the formation of groups is hindered and the viability decreases, which finally could lead to cell death.

In the past, the first tested materials for such arrays were glass, silicon and silicon-based materials, due to the origin of semi-conductor industry of such chips [27], but due to the better transparency and lower expenses, polymers have gained more widespread application [142, 143]. Polyethyleneglycol (PEG), poly(methylmethacrylate) (PMMA), polyurethane (PU), polystyrene (PS) or photo resists such as SU-8, are used amongst others. But the most common polymer is polydimethylsiloxane (PDMS) [27]. It addresses all the requirements as a microwell material for a fast, easy, inexpensive and feasible fabrication of microwell arrays, thus accessible even for standard equipped laboratories [144, 145]. PDMS can be sterilized, it is temperature resistant in the range of cell experiments as well as suitable for microscopy, due to optical transparency [27, 146–148]. One can even microscope directly through a certain height of PDMS layer. Further, it can be bonded to microscopy slides or microscopy foils and is gas permeable [149, 150].

But most important, PDMS exhibits a low autofluorescence [151] and a high biocompatibility [152]. To which extent this is valid, also in comparison to other microwell materials, will be described in detail in the following chapter. Seven different materials were tested for autofluorescence, the nature emission of light, and biocompatibility, in this case defined as the tolerability of biological organisms (cells) with the tested material. At the end of this chapter, a summary of conclusions and an outlook concerning the tested materials and properties is given. Further, an application of PDMS microwells, namely a proliferation study of stem cells, is described in detail. For a start, the individual materials are introduced in short.

Polycarbonate

Polycarbonate (PC) was found 1898 by Alfred Einhorn and is a synthetic thermoplastic polymer, namely a polyester of the carbonic acid ($[\text{ROCOO}]_n$). In most polycarbonates, bisphenol A (BPA) is the dihydroxy component and reacts in a surface condensation with phosgen. PC is relatively expensive in comparison to other polymers due to its extraordinary properties such as dimension stability, transparency, scratch-resistance, high hardness and stiffness, impact strength and chemical resistance to many mineral acids and aqueous solutions of oxidizing agents or neutral salts. In combination with polyurethan it can be turned even into an UV resistant material. Polycarbonates are amorph and show high biocompatibility. Many applications in industry are on the market: spectacle lenses, optical lenses, windows for airplanes and police cars, CDs, DVDs, LEGO, solar panels and medical disposables.

Here, a polycarbonate foil was tested (300MICRONS GmbH), which contained microwells of 300 μm in diameter and 300 μm depth. Since the microwell foils were produced by hot-embossing, the pore sizes can range from nm to μm following the information of the manufacturer. Brightfield images of the foil were taken with a 10x objective and 50 ms exposure time (Figure 5.1). The pores were identified as exclusion criterion for the use in single-cell measurements. The pores are in the size range of suspension cells and thus the identification and tracking of single cells would be impossible due to the indistinguishability to the pores. Despite the perfect size of the microwells, the easy use and low autofluorescence (Chapter 5.2), the polycarbonate foils were excluded as single-cell assay platform.

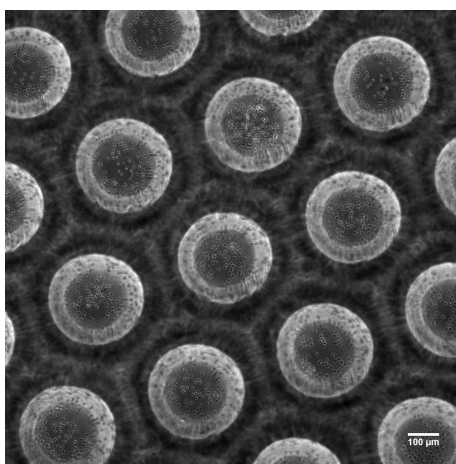


Figure 5.1: Brightfield image with 10x magnification of a polycarbonate foil with microwells of 300 μm diameter and 300 μm depth, fabricated by hot-embossing. Pores are visible due to production processes in hot-embossing.

Polyethyleneglycol diacrylate (PEG-DA)

Polyethyleneglycol diacrylate (PEG-DA) or polyethyleneglycol dimethacrylate (PEG-DMA) are two polymers, which were used in our chair already for different single-cell 3D applications. On the one hand, we used the material for so called microtrenches to follow the cell division and apoptosis of a whole family [140] and on the other hand, as microwells for progenitor cell division [141]. The structures were produced using soft lithography [144], namely the technique of micromolding in capillaries (MIMIC) [153]. More details about the material and the platform can be found in [154, 155]. In the past, the material was mainly used for label-free applications, but in this study, the focus was on fluorescence purposes such as signaling cascades and thus the material was again analyzed for autofluorescence (see results Chapter 5.2).

Furthermore, another idea was to spin-coat PEG-DA on a silane-treated glass slide and expose it to UV via a mask to create structures (photolithography). This less manual and less time consuming approach was promising, since also there the bio-compatible, well-known PEG-DA could be used in principle in combination with glass surfaces, which is well compatible for microscopy and further surface modifications. This approach was published several times by the group of Revzin et al. [156–160]. However, we were not able to reproduce their so called hydrogel microstructures even when using the same molecular weight (MW) of PEG-DA (575, the PEG-DA with MW of 258 is not too viscous), similar photoinitiator and silanes for silanization of the glass substrates. Further, different spinning speeds and times were tested, but none of the different parameter and setup changes could improve the adhesion of the polymer onto the surface, not to mention the height of the PEG-DA layer. So in the end, no proper coating thickness could be gained for the exposure to UV to cross-link the polymer via free-radical polymerization. In principle, after the UV exposure, the non treated areas, which were covered by the mask, can be dissolved in DI water after the development. But the descriptions given in the papers of Revzin et al. [156–160] were quite contradictory and ambiguous. The spinning speeds and times were quite different among the papers or not indicated at all, silanes used for silanization and the silanization process itself were varying. Lastly, the heights of the structures as well as the exposures times were just described in ranges, not with precise values. In summary, if this approach should be further developed, PEG-DA with a significant higher molecular weight (e.g. 4000), which is very costly, should be used.

Indexed-matched fluoroacrylate polymer MY-134

The fluoroacrylate polymer MY-134 is an patented and undisclosed elastomer (MY Polymer, Israel), since it has the unique property of a refractive index (1.34), which is matching the refractive index of cell culture medium ($n = 1.338$) [161]. This would be advantageous for the data acquisition and analysis of time-lapse measurements

for adherent as well as for non-adherent cells, since the microwells itself would not distract the tracking algorithm, which is for example the case with PEG-DA structures, which are causing fringes. The commercially available polymer can be cured under UV and is biocompatible, but only under some circumstances. Namely, the polymer has to be cured under argon atmosphere for 15-20 min, further under pure oxygen for 15 min to bleach the photoinitiator and afterwards the photoinitiator has to be removed by incubation in pure ethanol for 4-6 days. Only with this procedure the biocompatibility is given, otherwise it is a cytotoxic material. No information concerning the autofluorescence is provided by the manufacturer, but material fluorescence can be decreased by UV exposure in pure oxygen for 15 min [161].

Another alternative could be the MY-133 MC, which is also patented and undisclosed, fabricated by MY Polymer. But this amorph polymer is not acrylate based but a polyurethane prepolymer with an isocyanate term and designed to cure with ambient water (moisture-curing). Also this MY polymer has an interesting refractive index, in fact close to the one of water in a cured state ($n = 1.33$). Cell based applications are not published so far, but one for a calibration slide for the characterization of the TIRF excitation field [162]. Following the manufacturer instructions, 200 μm layers can be cured in 20-60 min under ambient conditions and have to be baked for 1 h at 80-100 $^{\circ}\text{C}$. Ambient conditions depend on the thickness of the layers, thick layers take longer curing while high humidity accelerate the curing.

SU-8

SU-8 (glycidyl ether of bisphenol A (BPA)) is a negative photoresist epoxy novolack with exceptional properties such as thermal and chemical resistance to many solvents. Further, excellent mechanical, physical and optical properties are the reasons that SU-8 is a frequently used material in the semi-conductor industry and is often used in microfabrication techniques (microchips, microfluidics etc) due to the ability to form structures with high aspect ratio. However, the high autofluorescence [163], the highly hydrophobic surface [163] as well as the low surface energy was experienced as a major problem. Especially for biological applications, such as cell-based assays, the lacking adhesion of cells to the surface poses a problem. Further, the antimony salts, which are present in the material as photo acid generator, and their potential toxicity are still under debate [164]. The antimony levels could be reduced by an increased UV exposure and additional baking time or baking steps [165]. In general, the biocompatibility of SU-8 structures and their applicability in biomedical implementations or use *in vivo* is questionable [166]. For example, the results of a broad-scale devised study to evaluate the biocompatibility *in vitro* and *in vivo* must be questioned, since only the leachates were analyzed with the help of an end-point bulk assay (MTT assay) [165]. Thus, the studied 9L rat glioma cells were never in direct contact to the SU-8 structures and the used biological assay just provides an averaged signal, not considering sub-populations or heterogeneity in cellular re-

sponse. Further, the dynamics were speculated, which could be a crucial point in biomedical applications, which are potentially exposed for long times to the body. Moreover, it is questionable, whether the examined muted immune response in mice is acceptable and especially whether the recommendation as an implant material is justified. Also the study of Stangegaard et al. shows double-edged outcomes [167]. On the one hand, the chemical surface procedure (HNO₃-CAN) increases the growth rate and morphology of cells in comparison to untreated structures, but on the other hand, around 200 genes show differences in gene expression profiling. One reason for the ambiguous biocompatibility could be the component bisphenol A (BPA), which is also educt in polycarbonate production (see above). Depending on the involved processes and the final concentration in the end polymer, BPA could be more or less toxic. But as such, BPA was shown to be toxic for flora [168], fauna [169] and humans [170].

However, SU-8 arrays were seemingly successful applied to investigate stem cell fates [171], which is in general a difficult and sensitive task. Overall, it was shown that the biocompatibility of SU-8 structures can be enhanced with surface treatment. For example, oxygen plasma treatment, which is shown to be stable over weeks [172], enhanced cell proliferation in comparison to untreated SU-8 surfaces [164]. Further, coating with PEG can increase the biofunctionality [173].

Prototype Resist from Microresist Technology

The prototype resist from Microresist Technology GmbH is a photocurable polymer, which is not commercially available yet and was tested as prototype. It can be used for molding techniques (MIMIC) and NanoImprint Lithography (NIL). Thus, the material is comparable to PEG-DA in principle, only that the quality is reproducible (photoinitiator has not to be mixed manually), it is more viscous, thus suitable for spin-coating (which is not possible with low MW PEG-DA) and the curing has to be performed without O₂, thus under inert gas atmosphere. It is clarified as biocompatible resist, as all components are biocompatible. The resist has the ISO 10993 certificate for biocompatibility of medical devices classification; therefore, the supernatant, which was exposed to the resist, has not to be harmful to the cells to receive this commendation. The autofluorescence is quite low, comparable to ibidi foils (data not shown, measured by C. Leu).

Liquid Glass

Glass is ubiquitous in our everyday lives and also in industry as well as in science a widely used material due to its excellent properties such as optical transparency, thermal and chemical resistance, inertness and biocompatibility. However, the classical techniques to structure glass are hazardous (due to the necessity of HF), time-consuming and expensive or rather impossible for most laboratories due to the need

of clean room facilities. Thus, glass is not suitable for rapid prototyping or for example stereolithography or 3D printing. Also the fabrication of microfluidics remains challenging since multilayer components are needed and the bonding between glass layers is problematic [174]. Thus, polymers have turned out to be the golden standard.

However, two commercially available glass structures, which were fabricated by etching, were tested for comparison. On the one hand, etched glass wafers (Schott) from QUALCOMM with lines of 60 μm depth (which were not homogeneously etched) and a total thickness of 300 μm were tested for almost 24 h with the CellROX green marker (indicating cellular stress) and the PI marker (cell death marker). In short, the results of the first test done by E. Chatzopoulou the MOLM-13 cells seem to survive, but are stressed (high signal from CellROX green).

On the other hand, the Licarda CC 384 well MicroplateTM made out of high-quality glass bottom with 150 spherical subwells per microwell (etched into the glass surface) was tested. The microwells were 3.2 mm in diameter and the subwell diameter was 200 μm with a depth of 100 μm . The thickness of the etched glass in total remained unclear in the manufacturer instructions. MOLM-13 were seeded after the tedious removal of air bubbles in two different seeding densities and twice replicates per density. Both densities were tested with or without fluorescence marker (CellROX and PI). A time-lapse of 24 h showed that in all conditions apoptosis started after 24 h, and after 50 h all cells were dead. The reason for cell death could be the roughness of the glass surface. Furthermore, the autofluorescence in the GFP and DAPI region was not negligible. The increased autofluorescence in the DAPI channel was also observed by E. Chatzopoulou for the etched glass wafer.

Recently the group of Bastian Rapp from Karlsruhe Institute of Technology (KIT) established a sintering method from photocurable components to form the so called *Liquid Glass* [174]. The liquid photocurable amorphous silica nanocomposite overcomes the three main drawbacks of microstructuring of glass: since the prepolymer can be structured at room temperature using PDMS molds, the disadvantages of the isotropic properties of the usually applied etching process are passed over. Secondly, the manufacture was turned into a replication process. Finally, the bonding on surfaces of the structures is not a problem anymore, since the photocured composite is a polymer. A thermal binding and sintering process step is following, which is converting the cured polymer into glass, and comparable to fused silica glass concerning physical and chemical properties [174]. The complete protocol for the fabrication of Liquid Glass structures can be read in [174]. In general, it has to be mentioned that the group of Rapp creates mostly bigger structures of some cm or more simple designs. Also in the follow up paper from 2017, the shown examples, which were printed with stereolithography 3D printers, are rather big or simple in design when microscaled [175]. However, when reproducing this technique in our laboratories and adapting the process to our needs (microwells in the range of 30-50 μm and 30 μm depth), we faced some serious issues. In the following, the work mainly done by C.

Leu and P. Altpeter is described.

As a first approach, the Micro Molding in Capillaries (MIMIC) technique [153], which was used with PEG-DA and PEG-DMA in the past [140, 141], was tested with the nanocomposite. However, the viscosity of the polymer is too high, air is entrapped during the process and the wetting is insufficient. Next, the Solvent Assisted Microcontact Molding (SAMIM) [144] method showed also some drawbacks. When squeezing the PDMS mold onto the polymer, a residual layer on the bottom is present and as the material is pressed to the edges, an edge bead is created. Further, in the next step of sintering, thermal stress is created and the structures bend clearly, delaminate or even break. The most promising attempt, was the micro Transfer Molding (μ TM) technique [144], where the polymer is casted on a PDMS mold and excess material is removed. This sandwich is flipped onto a substrate, thereafter the PDMS mold can be removed. After curing, the Liquid Glass polymer is as a structure on the substrate. This approach shows only a thin layer of remaining material on the bottom, less entrapped air and thermal stress, as well as only small edge beads. Also the stress related effects are reduced and in total, the method shows a higher reproducibility than the other two approaches. But still, only small areas with certain designs can be produced due to the thermal stress and the bending of the structures, if they are too large or too thin. Entrapped air leads to the break of the structures during molding. Further, the manufacture of Liquid Glass is not as time efficient and low cost as expected, even when the structures are re-used, since the process takes full two days with a existing design and 5 days for a new design (fabrication of a new Si-master included). In summary, the properties of the material speak for themselves (high transparency, low autofluorescence), but further development would be necessary for structured surfaces in microscopy slide size and small microwell designs.

Polydimethylsiloxane (PDMS)

Poly(dimethylsiloxane) (PDMS) is an elastomeric organosilicon and has the chemical formula $\text{CH}_3[\text{Si}(\text{CH}_3)_2\text{O}]_n\text{Si}(\text{CH}_3)_3$, where n is the number of monomers. In general, the base and the curing agent react with cross-linking via hydrosilation. In our lab, PDMS from Sylgard 184 (Dow Corning) is used. Dimethylsiloxane oligomers with vinyl-terminated end groups function as the base and a hexachloro platinum catalysator catalyses the reaction. Dimethylvinylated and trimethylated silica acts as a filler and the curing agent has a cross-linking agent (dimethyl methylhydrogen siloxane) and the inhibitor tetramethyl tetravinyl cyclotetrasiloxan [152]. A Si-C bond is formed from the vinyl and silicon hydride groups via hydrosilation to cross-link the polymer [152]. PDMS has a high temperature resistance (due to high bond energy of Si-O backbone), a low surface energy due to the high mobility of the Si-O chain, is chemically stable and optically transparent [176]. Only its hydrophobic nature can be disadvantageous in some cases, but it can be made more hydrophilic

via oxygen plasma activation. Due to its excellent properties, it is widely used in science, industry and our daily lives e.g. in medicine as surfactant and anti-foaming agent, in cosmetics as well as in food. Especially the research areas of microfluidics and softlithographie were pushed by George M. Whitesides, and PDMS was extensively used [142–148, 152, 153]. The viscoelastic polymer is also gas permeable, thus also suitable for many biological studies [145]. Still, the compatibility of PDMS with cells is discussed ambiguous in literature, it may depend on the cell line and each approach has to be tested separately [150]. Further, the material can be spin-coated due to its viscosity (depending on the number of monomers). Also the autofluorescence was shown to be very low and comparable to the one of glass [151]. PDMS presents the perfect material for rapid prototyping [148] and is accessible to every standard laboratory as structures can be produced in a fast and in-expensive way in almost unlimited designs.

5.2 Quantitative Analysis of Autofluorescence of Microwell Materials

Autofluorescence, the natural emission of light, is common in biological substances, for example in amino acids due to the aromatic ring system like tryptophan, tyrosin and phenylalanin [177]. Also other biological molecules such as riboflavin, melanin, collagen, chlorophyll or nicotinamide adenine dinucleotide phosphate (NADPH) can be excited with UV or deep UV [177]. This property can be useful, since specimen or organisms can be analyzed without further fluorescent dyes. Chloroplasts, daphnia or chlorella, for example, can be excited under the microscope without labeling [178]. But otherwise, e.g. the autofluorescence of polymers, can be obstructive for some experimental setups. In most readouts the desired target is illustrated with the help of fluorescent molecules or dyes. Especially for single-cell measurements, where each cell is observed separately and the signal is not averaged over the whole population, the intensity can be quite low. Further, often only low concentrations of fluorescent markers are used to avoid phototoxicity or the dyes are quite expensive (e.g. labelled antibodies) and thus only applied in nM concentrations. Moreover, if the target molecule is only present in limited quantities, which is for example the case of secreted cytokines per cell (fM), a low background signal is important. Unfortunately, many polymers, which are used for microfluidics or microstructures, such as parylene, polyimid and polyester show a non negligible autofluorescence [179]. But for such sensitive measurements, as mentioned above, a good signal-to-noise ratio is essential for an accurate, high quality readout. Thus, the right choice of material when designing a new setup, is crucially.

Therefore, we measured the autofluorescence of seven different materials, which are potential candidates for the development of microwells to observe cells at the single

cell level or in groups. The materials were all measured with the same background (in ibidi glass dishes) on the same microscope (Nikon) with 50% lamp intensity and 200 ms exposure time. The materials were measured with a quadband filter with the following channels: DAPI (exc: BP 392 nm, bandwidth 23 nm, emi: 432 nm, bandwidth 40 nm), GFP (exc: BP 474 nm, bandwidth 27 nm, emi: 515 nm, bandwidth 35 nm), PI (exc: BP 554 nm, bandwidth 23 nm, emi: 595 nm, bandwidth 35 nm) and Cy5 (exc: BP 625 nm, bandwidth 18 nm, emi: 730 nm, bandwidth 140). Even when some materials were tested before, the independent control if the materials are suitable for the specific needs we have, is important. And also when these outcomes are just rough estimates, as they are not calibrated to the thickness of the structures respectively, a first valuation is key to further develop only microwells with materials which completely fulfill the set requirements.

In summary, PDMS (both in-house made and the commercial ones from Microsurfaces Ltd.), Liquid Glass and the polycarbonate foil show a relative low autofluorescence as expected, thus are conceivable microwell materials (Figure 5.2). However, the polycarbonate foil was excluded due to the pores as discussed before. The index-matched polymer MY-134, SU-8 [180] and PEG-DA show a significant autofluorescence as assumed from our experience (PEG-DA) and literature (SU-8), thus not applicable for fluorescence measurements. The reason for the autofluorescence of MY-134 could be the missing inert atmosphere during the first and the missing pure oxygen during the second curing step. A potential approach to decrease the autofluorescence of SU-8 and PEG-DA could be to increase the baking and/or curing times and/or steps. In the case of PEG-DA, the purification of the monomer and photo-bleaching the structures could be helpful [181].

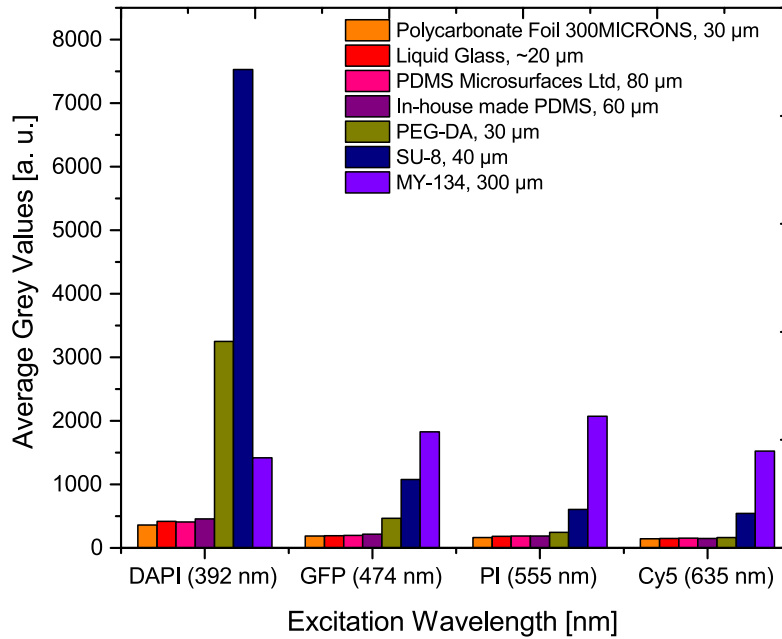


Figure 5.2: Autofluorescence of seven different potential microwell materials. A hot-embossed polycarbonate foil (300 µm depth, from 300MICRONS, orange), in-house made Liquid glass structures (various depths, red), PDMS wells in micromesh foils (80 µm depth, Microsurfaces Ltd., pink), in-house-made PDMS microwells (60 µm depth, purple), in-house micromolded PEG-DA microwells (30 µm depth, green), in-house SU-8 microwells (40 µm depth, dark blue) and molded and UV cured MY-134 wells (300 µm depth, blue) were analyzed. Autofluorescence was measured in four different channels (DAPI, GFP, PI and Cy5) on a Nikon Ti eclipse microscope with 200 ms exposure time and 50% of light intensity and plotted as grey values. Structures were placed on glass bottom ibidi dishes for a standard background.

5.3 Analysis of Biocompatibility of Microwell Materials

Another important parameter, which should be considered during the development of microwells next to autofluorescence, is biocompatibility (compatibility with biological systems). In general, biocompatibility of the material is given by the components itself. If all components are biocompatible, the whole composition should be also harmless to cells. On the other hand, the overall biocompatibility of the material can be increased in some cases. For example, the biocompatibility of SU-8 should increase with curing or another baking step; incomplete curing therefore, can lead to harmful properties [165]. Or, in case of the indexed-matched elastomer MY-134, the curing has to be processed under argon atmosphere for 20 min to cure the polymer completely, another 15 min under pure oxygen are necessary to bleach the photoinitiator and within a last step, the structures have to be incubated for 4-6 days in ethanol to ensure that biotoxic components are diluted. Of this complex and time-consuming

protocol with its several steps is not followed completely, biocompatibility is not given and apoptosis occurs within 5 h [161]. If missing biocompatibility is the only parameter, which is the reason not to use the material, several steps could be done to increase biocompatibility: ultra-violet irradiation, plasma deposition, more washing steps or incubation steps in harmless buffers to wash out toxic remains or coating the surface of the final structures with proteins such as fibronectin. In the following, the test results of different materials for the fabrication of single-cell or multi-cell microwells are described as well as further process steps, which were performed to increase biocompatibility, if not given by the material itself. The **polycarbonate** foil was not tested with cells, due to the pores in the material (Chapter 5.1). The differentiation between suspension cells and the pores would not be possible. **PEG-DA** was already shown as an excellent material for single-cell time-lapse measurements, if no fluorescence readout was needed [140, 141]. Since the technical possibilities for the complete curing of **MY-134** under inert atmosphere and thereafter under pure oxygen are not given yet, the biocompatibility tests with MY-134 are deferred. The **SU-8** resist was not tested for biocompatibility, since the results of the autofluorescence tests were unambiguous. The autofluorescence is too high and the material is not suitable for fluorescence microscopy experiments. Further, the new **Microresist Technology** resist was tested in our group with adherent and non-adherent cells. Microwells made with the prototype resist with a diameter of 60 μm were incubated with three different cell lines (A549, Huh7, MDA-MB-231) for 24 h. After the incubation cells did not adhere to the substrate, but were not dead yet (negative trypan blue staining). So far, no final conclusion can be made about the applicability for our needs. But, FN coating should be tested to increase the attachment of the cells to the material to test further the viability. Next, the non-adherent MOLM-13 cell line was tested with 30 μm microwells, made out of the prototype resist, for two days. Unfortunately, almost all cells were dead after incubation. Also here, further coating should help to increase the viability of the cells and thus the biocompatibility of the prototype resist. The biocompatibility of **Liquid Glass** structures (50 μm wells) was tested by A. Reiser with Huh7 cells for 24 h without any further coating after the UV sterilization. The cells proliferate on the substrate, in the wells as well as between the wells. A specific passivation would be necessary to avoid the adhesion on the bridges between the wells. Therefore, the technique from the group of Smith et al. could be tested [182]. Further, Smith developed with the group of Maniura-Weber a protocol for the surface functionalization of microwells with the help of micro contact printing of FN and the specific passivation with Pluronic F127 [183]. Moreover, Viasnoff and co-workers recently established a highly advanced method to coat even the walls of the microwells with a different substance than the bottom of the wells and passivate the runways additionally [184]. For suspension cells, a 48 h time-lapse from E. Chatzopoulou showed that MOLM-13 cells, treated with CellROX and PI markers only, are dead after the two days of incubation in Liquid Glass microwells. Here, a coating with FN would help to increase the viability of the cells potentially.

PDMS was found to be an excellent material for single-cell studies. First tests with MOLM-13 cells showed perfect results with high viability of the cells after 48 h. It is noteworthy to say that only the sterilization with UV or gas is successful. The sterilization with ethanol is not useful, since the absorbed ethanol will diffuse out during the measurement and cause cell death. Due to the positive results of the pre-tests, PDMS was the material of choice and PDMS microwells were fabricated with the help of a molding cast to analyze stem cell proliferation over seven days. The whole manufacture process, design of the structures as well as the study itself are described in Chapter 5.5 in detail.

5.4 Summary and Outlook

To summarize the knowledge gained from experiments and literature, the tested materials, fabrication techniques, setups/manufacturers, advantages and disadvantages as well as final conclusions per material, were tabulated (Figure 5.3). Moreover, the table includes three more materials: cyclo olefin polymers (COP) and cyclo olefin-copolymer (COC) as well as MY-134 MC. The cyclic olefin polymers are promising since they are low in autofluorescence (data not shown, measured by C. Leu), are easy to manufacture, e.g. with etching or hot embossing and have a high biocompatibility. In fact, both materials were already excessively used for single-cell time-lapse measurements, since COC (Topas) was previously and COP (Zeonor) is nowadays the material of ibidi foils. First tests with microwell fabrication were made, but further development is needed. MY-133 MC was already mentioned in the context with MY-134 as an alternative material since it can be cured conveniently with ambient humidity and can be structured with already established micro molding technique.

Nr.	Material	Technique	Name of Company/Platform	Advantages	Disadvantages	Conclusion
1	PDMS	Micromolding	Custom-made replicates	Low autofluorescence Easy use, any structure possible Cheap and fast production	Bubbles in small wells present Biocompatibility depends on cell line Secretion /uptake of molecules	Works well Hydrophilicity could increase with plasma treatment
2	Preliminary: PDMS Future: silicon	Cast Molding with mold from ibidi	Custom-made replicates	See above	See above	Good for bigger structures See above
3	COP	3D Printing	Zeonor	Low autofluorescence High biocompatibility	Printing has to be improved	Promising
4	COC	Hot embossing	Topas	High biocompatibility	Not tested yet	Promising
5	COC	Etching	Topas	Easy procedure, any structures possible COC etched foil can be bond to COC	Bonding to glass needs specific silanization	Promising
6	Humidity-curable polymer	Cast Molding	MY-133 MC	Water matching refractive index Easy use, cheap and fast production	Not tested yet	Promising
7	UV-curable Polymer	Cast Molding	MY-134	Water matching refractive index Easy use, cheap and fast production	No full curing of bigger structures Autofluorescence not negligible	Excluded
8	Photo lacquer	Spin-coating	SU-8	Easy use	High autofluorescence	Excluded
9	Biocompatible lacquer	Spin-coating	BIO-NIL	Easy use Bonding to glass possible High biocompatibility	Not really biocompatible so far Not commercially available yet	Promising But bonding with ibidi foil needs specific, yet unknown silanization
10	Biocompatible silicon	FullTrac inserts ibidi	Casting mould replicates	Low autofluorescence Easy use	Only four wells per structure	Low statistics
11	Biocompatible silicon	Scratch Inserts ibidi	Casting mould replicates	Low autofluorescence Easy use, high biocompatibility	Large surface hinders tracking of suspension cells	Excluded
12	Polycarbonate	Hot embossing	300 MICRONS Foil	Low autofluorescence	Optical anisotropy, bubbles	Excluded
13	PEG-DA	Micromolding in capillaries	Custom-made	High biocompatibility	High autofluorescence Low reproducibility, many steps	Excluded
14	LiquidGlass	μ Transfer Molding (μ TM) Sintering	Karlsruhe Institute of Technology	Low autofluorescence, good transparency High biocompatibility Reusability	Expensive, many steps, long process Restricted in area/geometries/dimensions Bending of large structures	Excluded
15	Glass	Etching	Licarda CC 384 well Microplate	Low autofluorescence Reusability	Low biocompatibility (due to roughness?) Not negligible autofluorescence Round bottom of subwells	Excluded

Figure 5.3: Decisionmatrix for different microwell materials.

5.5 Application: Time-resolved Proliferation Study of MDS Stem Cells

5.5.1 State of the Art

Hematopoietic Stem Cells (HSC)

Throughout our whole life, the blood system is responsible to continuously provide the body with blood cells, since mature blood cells have a short life time. Approximately one trillion (10^{12}) cells are developed in human adult bone marrow, making blood the most regenerative tissue [185]. This establishment and maintenance is based on self-renewing hematopoietic stem cells (HSC), which are present in small quantities (1 per 10^5) in the bone marrow [186, 187] and the division in progenitor cells. These two features are possible due to asymmetric cell division (approx. 10%), which depends on intrinsic as well as extrinsic factors; it has been suggested that stem cell differentiation is a stochastic process [188]. Despite the fact that they divide not frequently, it is believed that the whole pool of HSCs is turning over every few weeks [189]. Furthermore, it was found that HSCs can switch between dormancy, where the activity is preserved, and self-renewal during the homeostasis and repair modes [189]. In the 1960s, the multilineage differentiation of HSCs was discovered and around 20 years later, the classical hierarchical roadmap with the HSCs on the apex, was established (Figure 5.4, Discrete Differentiation) [186, 187, 190, 191]. In this model, the mononuclear HSCs form either more HSCs (self-renewal) or committed progenitors, such as lymphocytes or common myeloid progenitors (CMP). Out of these CMPs, which are large blast cells, megakaryocyte-erythroid progenitors (MEPs) or granulocyte-macrophage progenitors (GMPs) can be developed. CLPs are the progenitors of T and B lymphocytes, MEPs of erythrocytes and megakaryocyte platelets and GMPs are the progenitors of maturing cells such as neutrophils, eosinophils, basophil mast cells, dendritic cells, kupffer or langhans cells as well as monocyte macrophages (see a complete overview in [186]). This tree-like branched model has step-wise processes with distinct states (multipotent, oligopotent and unipotent) and considers HSC to be homogenous [191].

In contrast, during the last decades, a continuous differentiation process has gained growing acceptance (Figure 5.4, Continuous Differentiation) [191, 192]. The differentiation during early human hematopoiesis is not defined by discrete intermediate progenitor stages and branched tree-like decisions in this model, but by a cellular continuum. Velten et al. proposed the existence of so called low-primed undifferentiated (CLOUD)-HSPCs as transitory stages [192]. From these CLOUD-HSPCs, distinct, but independent lineages are developed within the continuous flow of differentiation. The lineages emerge earlier than thought and deepen gradually forced by fate mediators and gene expression.

With increasing methodologies, the ability to unravel the self-generation of HSCs as well as the generation of lineage-committed progeny is growing. Moreover, the heterogeneity of stem cells was recognized, whereas it was believed before that HSCs are homogenous [191]. Further, it was found that HSCs maybe cannot progeny unlimited and produce progenitors and thus are not equal with embryonic stem cells [186]. Despite the fact that blood is probably the most investigated developmental system due to seminal mouse experiments [185], still many open questions are arising. For example, whether the intermediate progenitors are present in the continuous model or if the fate of lineage-biased HSCs is predetermined [191]. However, new methods such as novel functional assays, omics-based techniques, non-invasive lineage tracing and single-cell time-lapse measurements will further support *in vivo* experiments and promote the understanding of hematopoiesis.

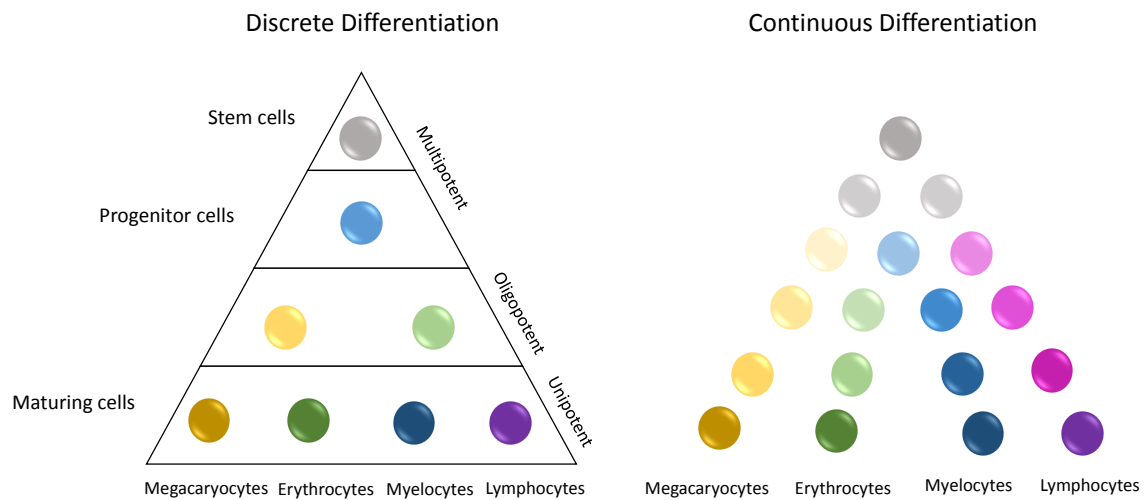


Figure 5.4: Two HSC Differentiation Models in Comparison. The Discrete Differentiation model illustrates step-wise hematopoiesis with distinct states (multipotent, oligopotent and unipotent) in a tree-like hierarchy from stem cells to progenitors over to maturing cells. In contrast, the Continuous Differentiation model in early hematopoiesis is based on a continuous flow of differentiation and lineage trajectories evolve independent of each other. Figure adapted from [191].

Myelodysplastic Syndrome (MDS)

The characteristic of the Myelodysplastic Syndrome (MDS) is a clonal stem cell disorder with active, but ineffective hematopoiesis [193]. MDS patients are grouped in high-risk (median survival of 6 years) and low-risk patients with a median survival of 6 months [194]. MDS can lead to cytopenia (reduction in number of mature blood cells) or acute myeloid leukemia (AML). The syndrome was divided in 5 subclasses by morphology in 1982 by the French-American-British (FAB), which was recently

reconsidered by the World Health Organization (WHO) into 8 subclasses [194]. If MDS evolves after the exposure to a mutagen such as toxic materials or after therapy of another disease, it is called secondary MDS [194]. Especially older people between 60 and 75 are diagnosed with MDS with a incidence of 15-50 per 100,000 humans per year (for >70 year old humans) with balanced sex distribution [194]. Clinical indications are fatigue, exertional dyspnea (shortness of breath), anemia, thrombocytopenia, leukopenia, granulocytopenia etc during the further progress in MDS.

Distinction to Acute Myeloid Leukemia (AML)

MDS may not only be the early phase of AML, and should not be considered as preleukemia anymore [195]. There are biological and clinical differences between the two diseases, whenever they show similarities, e.g. similar survival using the same therapy. But in contrast with AML, most MDS patients show increased programmed cell death, e.g. apoptosis and proliferation *in vitro* and *in vivo* [193, 195], presumably for compensation of the two progresses with each other. Most patients with MDS do not evolve AML until death. So far, the FAB classification distinguishes between MDS and AML by the number of fibroblasts. Patients who have less than 30% blasts are classified with MDS and the ones with more than 30% blasts are diagnosed with AML [195]. This is a rather arbitrary classification. Also the new classification by the WHO is better, but not optimal (AML diagnosis if more than 20% blasts are present)[195]. Albitrar at el. proposed that biological parameters, such as apoptosis and proliferation rate or differentiation, would provide a more distinct, precise and appropriate classification than the one based on the number of blasts [195]. Span and co-workers have taken up this idea and suggested low-risk MDS, identified by high proliferation, shorter cell doubling times and high apoptosis rates, whereas high-risk MDS shows the opposite trends [193].

Therapeutic Approach

The cure of MDS is uncommon, also since the usual enhanced age of the patients is the bottleneck. Allogeneic bone marrow transplantation is the only curative treatment, which is unfortunately not possible for elderly patients (>60 years). However, the life quality of the patients can be increased with curative approaches, e.g. erythrocyte treatment against anemia. Further, it has to be distinguished between low-risk patients and high-risk patients, who need aggressive chemotherapy and/or stem cell transplantation [195]. Also here, the age and the healthy fitness of the patients is limiting the therapeutic possibilities. Moreover, next to allogeneic bone marrow transplantation, which implies high toxicity, the autologous transplantation is an alternative (higher survival rates). Furthermore, hematopoietic growth fac-

tors, demethylating agents, immunosuppressive agents or more toxic substances, e.g. arsenic trioxide, can be applied [195].

5.5.2 Single-Cell Time-lapse Setup

PDMS Microwell Fabrication

The first step to investigate the proliferation of stem cells with single-cell time-lapse measurements was the preparation of the PDMS microwells. The microwells have a diameter and a depth of 300 μm to host single to few cells per well (Figure 5.5). This size provides enough space for the cells to divide for 7 days and ensures that the cells still can be tracked in single-cell resolution. The depth of the well ensures that the cells can not escape due to stage movement. Furthermore, a wall was designed around the 30 microwells to block thermal convection from the wells in the dish and to prevent great movement of the cells. The less movement of the cells, the easier the tracking and identification of the cells will be during data analysis. A dish was chosen as experimental format to provide sufficient supply of media during the one week measurement (3 mL). The whole protocol for the PDMS microwell fabrication can be looked up in the Appendix A.3. In short, PDMS was pored on a polyoxymethylen (POM, ibidi) casting mold, after removing bubbles from the PDMS mixture (10:1 monomer:cross-linker solution) and covered with a smooth foil to guarantee proper adhesion of the structures to the glass bottom of the dishes later on. Further, the so covered mold was placed between two metal plates, which was then fixed with two clamps for curing. This sandwich construct was cured overnight at room temperature and afterwards in the oven at 50 $^{\circ}\text{C}$ for another overnight. The clamps were then released and the foil removed to peel the PDMS microwells out of the mold. For sterilization, the structures were either exposed to UV for 10 min or gas sterilized (external company, DMB Apparatebau GmbH). The UV sterilization causes some changes to the PDMS surface (methyl groups are hydrolyzed and created hydroxyl groups are quite reactive, a SiO_2 is formed), but no difference to the gas sterilization was observed.

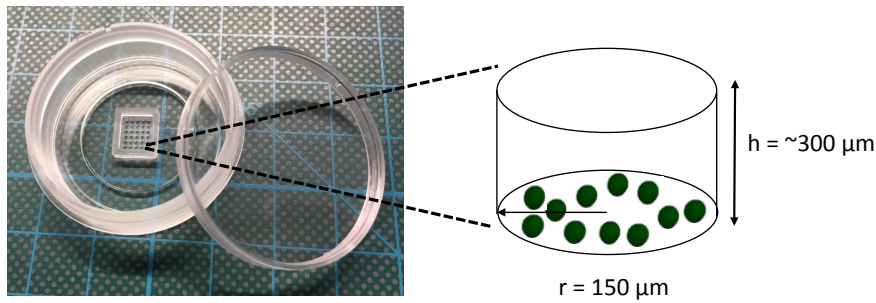


Figure 5.5: Photographic and schematic illustration of in-house made PDMS microwells. PDMS structure with 30 microwells and a surrounding wall to avoid convection streams is formed out of a polyoxymethylen mold and is placed in a glass bottom ibidi dish for measurements (photograph on the left). Microwells have a spacing of 500 μm to each other (zoom in on the right) and a diameter and depth of 300 μm .

HSC preparation

HSC cells were prepared by Michele Kyncl from the group of Dr. Katharina Götze, Klinikum rechts der Isar, III. Med. Klinik, TU Munich. The samples were taken from iliac crest surgery of anonymous donors with MDS diagnosis, which were tested negative for hepatitis B and C as well as for the HI virus (S1 classification). The cells, which were termed in the following 'healthy cells' have its origin from healthy bone marrow donors.

In detail, MDS samples were obtained by the cytological aspiration of bone marrow from the iliac crest region. Samples were diluted with PBS and mononuclear cells were isolated by gradient separation. The cell suspension was centrifuged and mononuclear cells were collected from the interphase. After centrifugation, cell pellets were mixed with freeze medium and frozen at -80°C . For long term storage, healthy and MDS samples were stored in a N_2 biotank.

On the day of the experiment, the patient and donor samples were thawed and immediately placed into media. Reducing dead cells, density gradient separation was performed. Mononuclear cells were centrifuged, washed with PBS and after another centrifugation step mixed with CellTrace™ Violet stain (a proliferation dye) in PBS and incubated in a water bath. The reaction was stopped by adding ice-cold medium containing HBSS, heat-inactivated FCS, HEPES, and Pen/Strep. After incubating on ice, the suspension was centrifuged and antibody staining was performed. Cells were first incubated with biotin-coupled antibodies, including anti-CD4, anti-CD8a, anti-CD1, anti-CD19, and anti-CD235a. The mixture was incubated on ice in the dark and then centrifuged. Pellets were resuspended with fluorescence-coupled antibody mix. After incubating on ice in the dark, medium was added and the cell suspension was centrifuged. Pellets were resuspended in medium containing propid-

ium iodide and filtered. Lin⁻CD45dim CD34⁺ CD38⁻ CD45RA-CD90⁺ cells were sorted with 4 lasers. Cells were collected in serum free medium.

Assessment of Single-Cell Arrays

As a next step, the sterilized PDMS microwells were incubated with 3 mL medium at 37 °C before seeding to get rid of bigger bubbles. Remaining smaller bubbles were removed with energetic up and down pipetting of the media. The structures have to be free from bubbles, since they hinder the seeded cells to settle down and disturb the tracking of the cells later during data analysis. Afterwards, the cells were directly seeded into the microwells with gentle handling. The seeding density varies from well to well, but it was taken care that not too many cells are in each well to guarantee a single-cell readout. The cells were incubated for 10 min to let them settle down by gravity. The density was checked and another seeding step followed if necessary to adapt the occupation of the wells to its optimum (2-3 cells per well).

Image acquisition

Time-lapse measurements were performed with a Nikon Ti eclipse microscope and an Okolab incubation box at 37°C and 10% CO₂ (final app. 5%). The stage was slowed down to reduce shaky movements of the cells, which would distract the cell tracking. The 7 day measurement protocol was divided in 24 h intervals of image acquisition, which are connected in series, to stabilize the software and the computer system (big data sets of min. 1.8 TB). Bright field images were acquired every 4-5 minutes, to do justice to the motility of the cells, with an exposure time of 5 ms. Usually, two healthy samples and two MDS samples were imaged in parallel per measurement, thus 120 field of views (wells) were set in total. Images were taken with a 20x objective and -5-10 µm out of focus, since the cells are then brighter and the contrast to the well bottom is higher. A high signal-to-noise ratio increases the ease and feasibility of the user to identify and track the cells.

Identification and Tracking of Single Cells

The following data analysis was performed in collaboration with the group of Dr. Carsten Marr from Helmholtz Zentrum München, Institute of Computational Biology.

For the identification and tracking of the HSC and the healthy cells, the software tool *The Tracking Tool* (tTt) was used [30]. This tool enables the manual tracking of single cells in long-term experiments with high accuracy. Even when the data shows uneven illumination or differences in brightness between wells or images within one

well a robust analysis should be guaranteed. Large data sets can be analyzed without expert knowledge and an user-friendly interface allows for manual inspection to ensure the validity and quality of the data.

As a first step, the microscopy data is converted from proprietary Nikon format (.nd) to TIFF files, to open the data in tTt and qTfy (will be needed later on). The image stacks are examined manually to select those cells, which should be tracked and an identity (ID) is given. This ID is controlled over time, if the track is not lost or changed by accident. The track will be lost only, when the cell dies. In our case, all cells were tracked to quantify how many cells divided or died in total. Further, qTfy, a software for the quantification of cellular and molecular properties, is needed to assemble the lineage trees for each single cell. This non-automated single-cell analysis ensures a high accuracy and quality of the data for conclusive lineage trees to analyze the proliferation of stem cells as well as apoptosis and possibly even motility.

5.5.3 Results and Discussion

Also here, the advantages of time-lapse measurements are obviously, since the continuous observation of cell division, cell shape, motility, real-time tracking of cell cycle times and size changes of stem cells is possible. However, due to the limited access to the rare and costly stem cell samples as well as data analysis challenges [5, 30], time-lapse studies were performed in the past [4, 22, 29, 141, 196, 197], but not standard yet.

In Figure 5.6, the distributions of the time to first division (t_{div}) of healthy cells in comparison to MDS cells, are shown. The violin plots show the kernel density distribution (grey) to estimate the distribution of t_{div} as well as statistical values such as the 50% quantile (bold red line) and the 25% and 75% quantiles (red lines) above and underneath the 50% quantile. The left graph shows 51 healthy cells and the right plot depicts 30 MDS cells; since the statistic is not vast, the following statements are preliminary and conditionally. The median of t_{div} for healthy cells is 57.33 ± 21.10 h, which is slightly longer than for MDS cells (48.50 ± 18.71 h). But due to the overlap of the standard deviations of the medians, the difference is not significant. Further, the 25% and 75% quantiles are broader distributed and shifted to later time points (25% quantile: 48.67 h, 75% quantile: 71.17 h) than for MDS cells. Here, the 25% quantile is closer to the median (45.08 h) than the upper 75% quantile (59.33 h). In summary, the values of t_{div} for both cell samples are similar, while the violin shapes of the kernel density distributions differ.

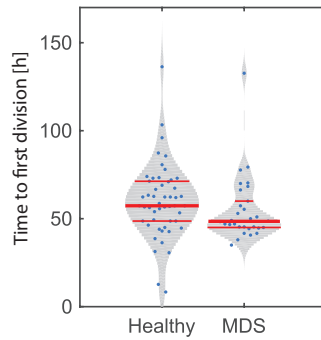


Figure 5.6: Distribution of time to first division of healthy cells in comparison to MDS cells. The median of the time to first division (bold red line, 50% quantile) for healthy cells (57.33 ± 21.10 h) is slightly higher than for MDS cells (48.50 ± 18.71 h). The 25% and 75% quantiles (red lines) overlap for both conditions, indicating no significant differences. In contrast, the shape of the kernel density (grey) differs.

Additionally, the length of the cell cycle was analyzed (Figure 5.7). The data points (blue) are pooled per time frame and are plotted per row. The shape of the rows have no meaning and is only curvy due for better illustration. For the healthy sample 482 cells and for the MDS sample 213 cells were analyzed. In contrast to the time to first division, the median of cell cycle duration (time between two divisions) is slightly shorter for the healthy cells (23.67 ± 14.34 h) than for the MDS cells (27.0 ± 13.18 h). Further, the shapes of the kernel density estimation are similar (grey). The 25% and 75% quantiles are distributed analogically, which can be seen by the calculated inter-quartile range (the difference between the 75% and the 25% quantiles), which is for both cell types 13 h.

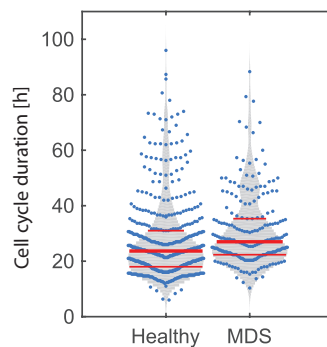


Figure 5.7: Distribution of cell cycle duration of healthy and MDS cells. The distribution of the kernel density estimation (grey) of the cell cycle duration distribution for healthy and MDS cells is quite similar, as well as the inter-quartile range (difference between 25% and 75% quantiles, red lines), which is for both cell types 13 h. The 50% quantile (bulk red line) of MDS cells (27.0 ± 13.18 h) is slightly higher than for the healthy cells (23.67 ± 14.34 h).

In literature, it was reported that the first division takes longer than the following divisions [188, 196, 197]. This could be due to a trauma phase due to the thawing, sample preparation, sorting, seeding and medium change. Also our results showed a longer time to first division than the following divisions (cell cycle durations) by comparison of Figure 5.6 and Figure 5.7.

Further, the apoptosis rate was determined, defined by the end of a cell track. In the sample of healthy cells 3% and for the MDS cells 10% of cells died. Further quantification with apoptosis markers are planned for a defined end point assessment.

5.5.4 Outlook

The preliminary results for the comparison between healthy cells and MDS cells show neither a significant difference in time points of the first division nor in the cell cycle length. It is noteworthy to say that the statistics of the one analyzed experiment (one MDS and one healthy sample) was not very high for both samples and further experiments are needed for reliable statements. Due to variable brightness levels, cell movement and seeding density, the automated segmentation, identification and tracking of the cells was not possible so far and manual tracking with tTt was applied.

In forthcoming experiments a low seeding density (likely one starting cell per well), the avoidance of bubbles and differences in brightness (between the wells and over time), as well as low movement of the cells should allow the automated data analysis and the separate annotation of cell fates (division, apoptosis). Lineage trees could then be created and used for deeper analysis of the stem cell behavior.

Moreover, the samples were fixed after the 7 day measurement for future determination of differentiation stages. Still, little is known about the correlation between cell cycle length and differentiation. Thus, single-cell time-lapse measurements provide an essential insight into the development of the myelodysplastic syndrome and potential approaches for chemotherapy to increase the life span and quality of patients.

Chapter 6

Conclusion and Outlook

In the present work, pair-wise event-time correlations of fluorescence markers were shown to be a powerful tool for the investigation of apoptosis signaling cascades. The chronological order of key players in different cell death pathways was assessed for the identification of novel target sites for chemotherapy.

The key contributors of the downstream signal transduction in apoptosis were illustrated with specific fluorescence markers. The events of lysosomal membrane permeabilization (LMP), the mitochondria outer membrane permeabilization (MOMP), the level of reactive oxygen species (ROS), which are cellular stress indicators, and the subsequent oxidative burst (OxBurst) as well as the release of calcium ions were observed in the early phase (initiation) phase of apoptosis.

In the late phase of apoptosis (execution), the onset of the caspase-3/7 activity (CASP), the flip of the membrane lipid phosphatidylserine (PhS-Flip) as well as the final permeabilization of the plasma membrane (PMP) are important checkpoints on the pathway to cell death.

The photochemistry of the markers and the mode of action inside the cell was examined and the single-cell fluorescence traces over time were analyzed for specific features, which are characteristic for the particular marker. The time courses were then put into the biological context of the marker. Further, phenomenological functions were assessed to reflect the time courses and with a maximum-likelihood fitting routine best fits were estimated. Significant changes in fluorescence were detected and the so called event times were extracted. For the early markers, the offset of fluorescence is significant, while for the late markers the onset time points are characteristic for apoptotic incidents. The event times of two markers are then used for pair-wise correlations to assess the sequence of events in the signaling cascade.

Insight was gained into the cellular interaction with 58 nm amino-modified polystyrene nanoparticles (PS-NH₂ NPs) with pair-wise correlations of early phase markers. The nanotoxicity study showed that a low concentration of PS-NH₂ NPs triggers LMP, which is leading to MOMP and OxBurst in A549 human lung cancer cells. Further, with high concentrations of PS-NH₂ NPs, an additional pathway to the lysosomal cascade was observed: the mitochondrial pathway with the event sequence MOMP-OxBurst-LMP.

The lysosomal but not the second pathway, triggered by MOMP, was monitored for the comparing Huh7 hepatocarcinoma cell line.

Further, the ROS rate was correlated with MOMP and LMP. It was found that MOMP is correlated with the ROS rate in both NP concentrations. In contrast, no correlation between LMP and the ROS rate was detected.

In the next chapter, the chronological order of the events MOMP, OxBurst and calcium release were investigated in A549 cells treated with the combinatorial chemotherapy of Etoposide (ETO) and the chemosensitizer PS89. Chemosensitizers are discovered to increase the vulnerability of cancer cells, which are often resistant to common cytostatica. Further, sensitizer enable a concentration reduction of the cytostatica, which are causing massive toxicity and side effects. For the single ETO and PS89 as well as for the combination for both the same order of events was examined: OxBurst follows MOMP, almost coincidentally, which is leading to the calcium ion release out of the stressed endoplasmic reticulum. Moreover, the effect enhancement was scrutinized, since synergistic (more than additive) effects would be desirable.

In addition to this, the ROS rate, which is proportional to the slope of the CellROX curve, as well as the area under the curve (AUC) of a ratiometric calcium indicator, which is representing the amount of released calcium ions, should be analyzed and correlated with the events MOMP, OxBurst and calcium release.

In the last part of this work, a suitable material for microwells was sought. Microwells, which are microenvironments densely packed in arrays, provide a convenient experimental setup for a high-throughput readout of suspension cells. Two main criteria must be fulfilled: low autofluorescence for fluorescence readouts and high biocompatibility. Seven materials were tested and PDMS conclusively complies both requirements.

Thus, the monitoring of stem cell proliferation and apoptosis was performed in PDMS microwells. Therefore, healthy stem cells as well as stem cells with the myelodysplastic syndrome (MDS) were observed in parallel for around 7 days. First outcomes show that the time to first division is in average longer than the cell cycle duration for both the healthy and the MDS cells. The time to first division as well as the cell cycle duration was similar in both samples. The apoptosis rate for the healthy cells was slightly lower than in MDS cells.

In summary, single-cell time-lapse measurements enable the resolution of signaling transduction cascades in a dynamic and a high-throughput manner. Average based bulk measurements mask the presence of potential sub-populations and do not allow to resolve the heterogeneity in cellular response.

Moreover, pair-wise event time correlations facilitate the assessment of relations between the events within a signaling cascade. The cellular heterogeneity in response (noise) can be investigated and further the strength of the correlations, as well as the time delays between the events, can be inspected.

6.1 3D Microwells for Adherent Cells in Apoptosis Studies

2D micro-structured surfaces are a straightforward, cost-effective and mostly reproducible setup for the observation of many different phenomena such as cell migration, cell-to-cell-communication, gene expression etc. Hundreds of cells can be observed in parallel with a high time resolution in a high-throughput manner. However, in the nanotoxicity (Chapter 3) and the combinatorial chemotherapy study (Chapter 4), a non negligible fraction of cells detached during the observation time. Over the process of apoptosis, where the formation of apoptotic bodies is characteristic, the relief of cells was recognized to be adverse. The statistics decreased by losing cells and a slight bias could be created by discarding time traces of detaching cells.

Thus, the embedding of adherent cells in 3D microwells could counteract this issue. As discussed in Chapter 5, different potential materials are conceivable. In addition, three more materials could be chosen: the cyclo olefin polymer (COP), the cyclo olefin-copolymer (COC) as well as the index-matched polymer MY-134 MC, which is cured by ambient humidity. Both cyclic olefin polymers are auspicious, since they are low in autofluorescence, microwells can easily be manufactured by etching or hot embossing and show a high biocompatibility.

The surface of such micro-molded or hot-embossed microwells have to be chemically modified to guarantee the controlled adhesion of the cells. The group of Maniura et al. developed a promising approach for microwell functionalization [183]. In short, the plasma cleaned PDMS microwells were incubated with a fibronectin (FN) solution and the surface is coated completely with the protein. Further, glutaraldehyde (GA) is bonded to another layer of PDMS via an aminosilane. The GA covered stamp was repeatedly placed on top of the FN coated microwells. After incubation, the FN on the bridges between the wells is removed due to reaction of FN with GA. Next, a solution of cell-repellent pluronic was applied to the microwells. After rinsing, the cells adhere purposefully only inside the wells and not on the bridges in between. The bifunctionalized microwells represent an ideal environment for the observation of cells in apoptosis studies, but also for the performance of ELISAs or the detection of immune response, e.g. secreted cytokines.

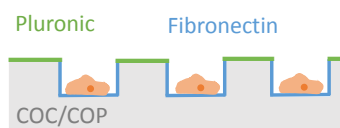


Figure 6.1: Schematic of specific microwell functionalization. The microwells, which are hot-embossed or molded with cyclo olefin polymers (COP) or cyclo olefin-copolymer (COC), are functionalized inside the wells with cell-friendly fibronectin (blue). The area between the wells is passivated with pluronic (green) to avoid unspecific adhesion.

6.2 The Future of Deep Machine Learning in Biological Data

For a precise determination of signaling cascades, a thorough data analysis has to be guaranteed. Here, the single cells were selected semi-automated in a custom written ImageJ plugin. The assortment of the desired cells by discarding of detaching, doubling, floating and migrating cells is tedious as well as time and click intensive. Next to the local confinement of the cells, which can be provided by the used micropatterned slides [10] or microfluidics [198], an automated readout of the cells increases the faster availability and a higher accuracy of single-cell data. Therefore, modern machine learning, especially deep learning methods such as neural network architectures were used for the recognition of cell counting, detection and morphology as well as for image reconstruction [199]. Also the classification of cells can be achieved with supervised machine learning [200]. Furthermore, in drug discovery the advantages of machine learning algorithms can be used for a label-free detection of drug responses [201]. Thus, machine learning was already implemented in several different fields of natural science. For our purposes, the recently published generic deep-learning-based software **U-Net**, seems to be promising for the detection and segmentation of cells [202]. The freely available ImageJ plugin is pre-trained to segment single cells and can be adapted for individual needs. The plugin is not restricted to specific data, but can be trained on new data, thus providing a broad applicability within biomedical image data. Only one or two representative images in high quality are needed for training, not big data sets as usually required in the past. Further, it is stated that both, unskilled researchers as well as experienced users, can train the program for their demands. Thus, U-Net represents a suitable, adaptable, fast and convenient opportunity to analyze single cells for the generation of reliable time traces. Henceforth, also for the fitting routine and the extraction of event times, neural networks can be beneficial. In the future, machine learning methods such as deep learning and neural network architectures will be essential for data analysis.

Bibliography

- [1] Rainer Opgen-Rhein and Korbinian Strimmer. From correlation to causation networks: A simple approximate learning algorithm and its application to high-dimensional plant gene expression data. *BMC Systems Biology*, 1, 2007. ISSN 17520509. doi: 10.1186/1752-0509-1-37.
- [2] Adam P. Arkin and David V. Schaffer. Network news: Innovations in 21st century systems biology. *Cell*, 144(6):844–849, 2011. ISSN 00928674. doi: 10.1016/j.cell.2011.03.008.
- [3] Hopin Lee, Robert D. Herbert, and James H. McAuley. Mediation Analysis. *JAMA - Journal of the American Medical Association*, 321(7):697–698, 2007. ISSN 15383598. doi: 10.1001/jama.2018.21973.
- [4] Timm Schroeder. Long-term single-cell imaging of mammalian stem cells. *Nature methods*, 8(4 Suppl):S30–S35, 2011. ISSN 1548-7091. doi: 10.1038/nmeth.1577.
- [5] Stavroula Skylaki, Oliver Hilsenbeck, and Timm Schroeder. Perspective Challenges in long-term imaging and quantification of single-cell dynamics. *Nature Publishing Group*, 34(11):1137–1144, 2016. ISSN 1087-0156. doi: 10.1038/nbt.3713.
- [6] Maureen A. Walling and Jason R.E. Shepard. Cellular heterogeneity and live cell arrays. *Chemical Society Reviews*, 40(7):4049–4076, 2011. ISSN 03060012. doi: 10.1039/c0cs00212g.
- [7] Peter S. Swain Michael B. Elowitz, Arnold J. Levine, Eric D. Siggia. Stochastic Gene Expression in a Single Cell. *Science*, 297:1183–1187, 2002. doi: 10.1126/science.1070919.
- [8] Martin Etzrodt, Max Endeke, and Timm Schroeder. Review Quantitative Single-Cell Approaches to Stem Cell Research. *Stem Cell*, 15(5):546–558, 2014. ISSN 1934-5909. doi: 10.1016/j.stem.2014.10.015.
- [9] James C. W. Locke and Michael B. Elowitz. Using movies to analyse gene circuit dynamics in single cells. *Nature Reviews Microbiology*, 7(5):383–392, 2009. ISSN 1740-1526. doi: 10.1038/nrmicro2056.

- [10] J. O Reiser, A., Zorn, M. L., Murschhauser, A., & Rädler. Single Cell Microarrays Fabricated by Microscale Plasma-Initiated Protein Patterning (μ PIPP). In *Cell-Based Microarrays*, pages 41–54. Humana Press, New York, NY, 2018.
- [11] J F Kerr, C M Winterford, and B V Harmon. Apoptosis. Its significance in cancer and cancer therapy. *Cancer*, 73(8):2013–2026, 1994. ISSN 0008-543X. doi: 10.1002/1097-0142(19940415)73:8<2013::AID-CNCR2820730802>3.0.CO;2-J.
- [12] Scott W.Lowe and Athena W.Lin. Apoptosis in cancer. *Carcinogenesis*, 21(3):485–495, 2000.
- [13] Bruce a Chabner and Thomas G Roberts. Timeline: Chemotherapy and the war on cancer. *Nature reviews. Cancer*, 5(1):65–72, 2005. ISSN 1474-175X. doi: 10.1038/nrc1529.
- [14] Ingrid Herr and Klaus-michael Debatin. Review article Cellular stress response and apoptosis in cancer therapy. *Blood*, 98(9):2603–2614, 2001.
- [15] Dino Di Carlo and Luke P Lee. -CELL ANALYSIS for Quantitative Biology. *Anal Chem*, 78(23):7918–7925, 2006.
- [16] Sabrina L. Spencer, Suzanne Gaudet, John G. Albeck, John M. Burke, and Peter K. Sorger. Non-genetic origins of cell-to-cell variability in TRAIL-induced apoptosis. *Nature*, 459(7245):428–432, 2009. ISSN 0028-0836. doi: 10.1038/nature08012.
- [17] Pratikkumar Shah, Ajeet Kaushik, and Xuena Zhu. Chip based single cell analysis for nanotoxicity. *The Royal Society of Chemistry*, 139:2088–2098, 2014. doi: 10.1039/c3an02280c.
- [18] Iris Hansjosten, Juliane Rapp, Luisa Reiner, Ruben Vatter, Susanne Fritsch-Decker, Ravindra Peravali, Taina Palosaari, Elisabeth Joossens, Kirsten Gerloff, Peter Macko, Maurice Whelan, Douglas Gilliland, Isaac Ojea-Jimenez, Marco P. Monopoli, Louise Rocks, David Garry, Kenneth Dawson, Peter J.F. Röttgermann, Alexandra Murschhauser, Joachim O. Rädler, Selina V.Y. Tang, Pete Gooden, Marie France A. Belinga-Desaunay, Abdullah O. Khan, Sophie Briffa, Emily Guggenheim, Anastasios Papadimitriou, Iseult Lynch, Eugenia Valsami-Jones, Silvia Diabaté, and Carsten Weiss. Microscopy-based high-throughput assays enable multi-parametric analysis to assess adverse effects of nanomaterials in various cell lines. *Archives of Toxicology*, 92(2):633–649, 2018. ISSN 14320738. doi: 10.1007/s00204-017-2106-7.
- [19] Yangzhe Wu, Tian Yu, Timothy A Gilbertson, Anhong Zhou, Hao Xu, and Kytai Truong Nguyen. Biophysical Assessment of Single Cell Cytotoxicity :

- Diesel Exhaust Particle-Treated Human Aortic Endothelial Cells. *PLoS ONE*, 7(5):1–10, 2012. doi: 10.1371/journal.pone.0036885.
- [20] Julia Blechinger, Alexander T Bauer, Adriano A Torrano, Christian Gorzelanny, Christoph Bräuchle, and Stefan W Schneider. Uptake Kinetics and Nanotoxicity of Silica Nanoparticles Are Cell Type Dependent. *Small*, 9(23):3970–3980, 2013. doi: 10.1002/sml.201301004.
- [21] Peter J F Röttgermann, Kenneth A Dawson, and Joachim O Rädler. Time-Resolved Study of Nanoparticle Induced Apoptosis Using Microfabricated Single Cell Arrays. *Microarrays*, pages 1–11, 2016. ISSN 2076-3905.
- [22] Hanna M Eilken, Shin-Ichi Nishikawa, and Timm Schroeder. Continuous single-cell imaging of blood generation from haemogenic endothelium. *Nature*, 457(7231):896–900, 2009. ISSN 1476-4687. doi: 10.1038/nature07760.
- [23] John G. Albeck, John M. Burke, Bree B. Aldridge, Mingsheng Zhang, Douglas A. Lauffenburger, and Peter K. Sorger. Quantitative Analysis of Pathways Controlling Extrinsic Apoptosis in Single Cells. *Molecular Cell*, 30(1):11–25, 2008. ISSN 10972765. doi: 10.1016/j.molcel.2008.02.012.
- [24] Sabrina L. Spencer and Peter K. Sorger. Measuring and modeling apoptosis in single cells. *Cell*, 144(6):926–939, 2011. ISSN 00928674. doi: 10.1016/j.cell.2011.03.002.
- [25] Conor M. Henry, Emilie Hollville, and Seamus J. Martin. Measuring apoptosis by microscopy and flow cytometry. *Methods*, 61(2):90–97, 2013. ISSN 10462023. doi: 10.1016/j.ymeth.2013.01.008.
- [26] Sabine Pietkiewicz, Jörn H. Schmidt, and Inna N. Lavrik. Quantification of apoptosis and necroptosis at the single cell level by a combination of Imaging Flow Cytometry with classical Annexin V/propidium iodide staining. *Journal of Immunological Methods*, 423:99–103, 2015. ISSN 18727905. doi: 10.1016/j.jim.2015.04.025.
- [27] Sara Lindström and Helene Andersson-Svahn. Miniaturization of biological assays - Overview on microwell devices for single-cell analyses. *Biochimica et Biophysica Acta - General Subjects*, 1810(3):308–316, 2011. ISSN 03044165. doi: 10.1016/j.bbagen.2010.04.009.
- [28] JR Swedlow, Ilya Goldberg, Erik Brauner, and PK Sorger. Informatics and quantitative analysis in biological imaging. *Science*, 300(5616):100–102, 2003. doi: 10.1126/science.1082602.Informatics.
- [29] Felix Buggenthin, Carsten Marr, Michael Schwarzfischer, Philipp S Hoppe, Oliver Hilsenbeck, Timm Schroeder, and Fabian J Theis. An automatic method

- for robust and fast cell detection in bright field images from high-throughput microscopy. *BMC Bioinformatics*, 14(1):297, 2013. ISSN 1471-2105. doi: 10.1186/1471-2105-14-297.
- [30] Oliver Hilsenbeck, Michael Schwarzfischer, Stavroula Skylaki, Bernhard Schauburger, Philipp S Hoppe, Dirk Loeffler, Konstantinos D Kokkaliaris, Simon Hastreiter, Eleni Skylaki, Adam Filipczyk, Michael Strasser, Felix Buggenthin, Justin S Feigelman, Jan Krumsiek, Adrianus J J van den Berg, Max Endeke, Martin Etzrodt, Carsten Marr, Fabian J Theis, and Timm Schroeder. Software tools for single-cell tracking and quantification of cellular and molecular properties. *Nat Biotech*, 34(7):703–706, 2016. ISSN 1087-0156. doi: 10.1038/nbt.3626\rhttp://www.nature.com/nbt/journal/v34/n7/abs/nbt.3626.html#supplementary-information.
- [31] Jean-yves Tinevez, Nick Perry, Johannes Schindelin, Genevieve M Hoopes, Gregory D Reynolds, Emmanuel Laplantine, Sebastian Y Bednarek, Spencer L Shorte, and Kevin W Eliceiri. TrackMate : An open and extensible platform for single-particle tracking. *Methods*, 115:80–90, 2017. doi: 10.1016/j.ymeth.2016.09.016.
- [32] Lorenzo Galluzzi, Ilio Vitale, Stuart A. Aaronson, John M. Abrams, Dieter Adam, Patrizia Agostinis, Emad S. Alnemri, Lucia Altucci, Ivano Amelio, and Et al. Molecular mechanisms of cell death: Recommendations of the Nomenclature Committee on Cell Death 2018. *Cell Death and Differentiation*, 25(3):486–541, 2018. ISSN 14765403. doi: 10.1038/s41418-017-0012-4.
- [33] Majdouline Abou-ghali and Johnny Stiban. Regulation of ceramide channel formation and disassembly : Insights on the initiation of apoptosis. *Saudi Journal of Biological Sciences*, 22(6):760–772, 2015. ISSN 1319-562X. doi: 10.1016/j.sjbs.2015.03.005.
- [34] Lorenzo Galluzzi, Naoufal Zamzami, Thibault De La Motte Rouge, Christophe Lemaire, Catherine Brenner, and Guido Kroemer. Methods for the assessment of mitochondrial membrane permeabilization in apoptosis. *Apoptosis*, 12(5): 803–813, 2007. ISSN 13608185. doi: 10.1007/s10495-007-0720-1.
- [35] G Kroemer, W S El-Deiry, P Golstein, M E Peter, D Vaux, P Vandenabeele, B Zhivotovsky, M V Blagosklonny, W Malorni, R A Knight, M Piacentini, S Nagata, and G Melino. Classification of cell death: recommendations of the Nomenclature Committee on Cell Death. *Cell Death and Differentiation*, 12: 1463–1467, 2005. ISSN 14765403. doi: 10.1038/sj.cdd.4401724.
- [36] Alexandra Murschhauser, Peter J. F. Röttgermann, Daniel Woschée, Martina F. Ober, Yan Yan, Kenneth A. Dawson, and Joachim O. Rädler. A

- high-throughput microscopy method for single-cell analysis of event-time correlations in nanoparticle-induced cell death. *Communications Biology*, 2(1):35, 2019. ISSN 2399-3642. doi: 10.1038/s42003-019-0282-0.
- [37] Peter J F Röttgermann, Samira Hertrich, Ida Berts, Max Albert, Felix J. Segerer, Jean François Moulin, Bert Nickel, and Joachim O. Rädler. Cell motility on polyethylene glycol block copolymers correlates to fibronectin surface adsorption. *Macromolecular Bioscience*, 14(12):1755–1763, 2014. ISSN 16165195. doi: 10.1002/mabi.201400246.
- [38] Peter J. F. Röttgermann, Alicia Piera Alberola, and Joachim O. Rädler. Cellular self-organization on micro-structured surfaces. *Soft Matter*, 10(14):2397, 2014. ISSN 1744-683X. doi: 10.1039/c3sm52419a.
- [39] <http://creativecommons.org/licenses/by/4.0/>, 2019.
- [40] Nicole Rusk. The fluorescence microscope. *Nature Milestones*, 7(1967):2009, 2009. ISSN 1465-7392. doi: 10.1038/ncb1941.
- [41] Mariana G Bexiga, Juan A Varela, Fengjuan Wang, Federico Fenaroli, Anna Salvati, Iseult Lynch, Jeremy C Simpson, and Kenneth A Dawson. Cationic nanoparticles induce caspase 3-, 7- and 9-mediated cytotoxicity in a human astrocytoma cell line. *Nanotoxicology*, 5(4):557–567, dec 2011. ISSN 1743-5390. doi: 10.3109/17435390.2010.539713.
- [42] Fabian Koczian, Olga Nagło, Britta Hettich, Uli Kazmaier, Stephan A Sieber, Binje Vick, Jan Vomacka, Simone Braig, Irmela Jeremias, Phil Servatius, Stefan Zahler, and Themistoklis Zisis. Targeting the ER-mitochondria interface sensitizes leukemia cells towards cytostatics. *Haematologica*, page haematol.2018.197368, 2018. ISSN 0390-6078. doi: 10.3324/haematol.2018.197368.
- [43] Maria Eugenia Guicciardi, Marcel Leist, and Gregory J Gores. Lysosomes in cell death. *Oncogene*, pages 2881–2890, 2004.
- [44] M O Hengartner. The biochemistry of apoptosis. *Nature*, 407(6805):770–6, 2000. ISSN 0028-0836. doi: 10.1038/35037710.
- [45] Sten Orrenius Pierluigi Nicotera. The role of calcium in apoptosis. *Cell Calcium*, 23(2/3):173–180, 1998. ISSN 09660844. doi: 10.1023/A:1009226316146.
- [46] G M Cohen. Caspases: the executioners of apoptosis. *The Biochemical journal*, 326 (Pt 1:1–16, 1997. ISSN 03784274. doi: 10.1016/S0378-4274(98)80028-3.
- [47] Seth W Perry, John P Norman, Justin Barbieri, Edward B Brown, and A Harris. Gradient : a Practical Usage Guide. *Biotechniques*, 50(2):98–115, 2011. doi: 10.2144/000113610.Mitochondrial.

- [48] Russell C. Scaduto and Lee W. Grotyohann. Measurement of mitochondrial membrane potential using fluorescent rhodamine derivatives. *Biophysical Journal*, 76(1 I):469–477, 1999. ISSN 00063495. doi: 10.1016/S0006-3495(99)77214-0.
- [49] Michael P. Murphy. Selective targeting of bioactive compounds to mitochondria. *Trends in Biotechnology*, 15(8):326–330, 1997. ISSN 01677799. doi: 10.1016/S0167-7799(97)01068-8.
- [50] Juliette Logan, Nicholas Schwarz, Philip Hockberger, Andrew Monteith, Philip Chan, Weiming Yu, William Marszalec, and David Wokosin. Imaging of Mitochondrial and Non-Mitochondrial Responses in Cultured Rat Hippocampal Neurons Exposed to Micromolar Concentrations of TMRM. *PLoS ONE*, 8(3): e58059, 2013. doi: 10.1371/journal.pone.0058059.
- [51] Luciano Merlini, Patrizia Sabatelli, Annarita Armaroli, Saverio Gnudi, Alessia Angelin, Paolo Grumati, Maria Elena Michelini, Andrea Franchella, Francesca Gualandi, Enrico Bertini, Nadir Mario Maraldi, Alessandra Ferlini, Paolo Bonaldo, and Paolo Bernardi. Cyclosporine a in Ullrich congenital muscular dystrophy: Long-term results. *Oxidative Medicine and Cellular Longevity*, 2011, 2011. ISSN 19420900. doi: 10.1155/2011/139194.
- [52] Kaisa M. Heiskanen, Manjunatha B. Bhat, Hsing Wen Wang, Jianjie Ma, and Anna Liisa Nieminen. Mitochondrial depolarization accompanies cytochrome c release during apoptosis in PC6 cells. *Journal of Biological Chemistry*, 274(9):5654–5658, 1999. ISSN 00219258. doi: 10.1074/jbc.274.9.5654.
- [53] Niamh M.C. Connolly, Pierre Theurey, Vera Adam-Vizi, Nicolas G. Bazan, Paolo Bernardi, Juan P. Bolaños, Carsten Culmsee, and Et al. Guidelines on experimental methods to assess mitochondrial dysfunction in cellular models of neurodegenerative diseases. *Cell Death and Differentiation*, 25(3):542–572, 2018. ISSN 14765403. doi: 10.1038/s41418-017-0020-4.
- [54] A. Haj-Yehia H.-U. Simon and F. Levi-Schaffer. Role of reactive oxygen species (ROS) in apoptosis induction. *Apoptosis*, 5:415–418, 2000.
- [55] Xianhua Wang & Huaqiang Fang & Zhanglong Huang & Wei Shang & Tingting Hou & Aiwu Cheng & Heping Cheng. Imaging ROS signaling in cells and animals. *J Mol Med*, 91:917–927, 2013. ISSN 09462716. doi: 10.1007/s00109-013-1067-4.
- [56] Martin D. Bootman, Katja Rietdorf, Tony Collins, Simon Walker, and Michael Sanderson. Ca²⁺-sensitive fluorescent dyes and intracellular Ca²⁺ imaging. *Cold Spring Harbor Protocols*, 8(2):83–99, 2013. ISSN 19403402. doi: 10.1101/pdb.top066050.

-
- [57] D. Thomas, S. C. Tovey, T. J. Collins, M. D. Bootman, M. J. Berridge, and P. Lipp. A comparison of fluorescent Ca²⁺ indicator properties and their use in measuring elementary and global Ca²⁺ signals. *Cell Calcium*, 28(4):213–223, 2000. ISSN 01434160. doi: 10.1054/ceca.2000.0152.
- [58] Jeffrey T. Lock, Ian Parker, and Ian F. Smith. A comparison of fluorescent Ca²⁺ indicators for imaging local Ca²⁺ signals in cultured cells. *Cell Calcium*, 58(6):638–648, 2015. ISSN 15321991. doi: 10.1016/j.ceca.2015.10.003.
- [59] N. Milanovich, M. Suh, R. Jankowiak, G. J. Small, and J. M. Hayes. Binding of TO-PRO-3 and TOTO-3 to DNA: Fluorescence and hole-burning studies. *Journal of Physical Chemistry*, 100(21):9181–9186, 1996. ISSN 00223654. doi: 10.1021/jp9600625.
- [60] Daniel Woschée. *The dynamics of apoptosis on the single-cell basis*. PhD thesis, LMU Munich, 2016.
- [61] Peter P. Fu, Qingsu Xia, Huey-Min Hwang, Paresh C. Ray, and Hongtao Yu. Mechanisms of nanotoxicity: Generation of reactive oxygen species. *Journal of Food and Drug Analysis*, 22(1):64–75, 2014. ISSN 10219498. doi: 10.1016/j.jfda.2014.01.005.
- [62] Tian Xia, Michael Kovoichich, Monty Liong, Jeffrey I Zink, and Andre E Nel. Cationic Polystyrene Nanosphere Toxicity Depends on Cell-Specific Endocytic and Mitochondrial Injury Pathways. *ACS Nano*, 2(1):85–96, 2008.
- [63] Daniele Rubert Nogueira, Clarice M. Bueno Rolim, and Ammad Ahmad Farooqi. Nanoparticle induced oxidative stress in cancer cells: Adding New Pieces to an incomplete Jigsaw Puzzle. *Asian Pacific Journal of Cancer Prevention*, 15(12):4739–4743, 2014. ISSN 15137368. doi: 10.7314/APJCP.2014.15.12.4739.
- [64] A. Nel. Toxic Potential of Materials at the Nanolevel. *Science*, 311(5761):622–627, 2006. ISSN 0036-8075. doi: 10.1126/science.1114397.
- [65] Andre Nel, Tian Xia, and Ning Li. Toxic Potential of Materials. *Science*, 311(5726):622–627, 2007. ISSN 0036-8075. doi: 10.1126/science.1114397.
- [66] Andre E. Nel, Lutz Mädler, Darrell Velegol, Tian Xia, Eric M.V. Hoek, Ponisseril Somasundaran, Fred Klaessig, Vince Castranova, and Mike Thompson. Understanding biophysicochemical interactions at the nano-bio interface. *Nature Materials*, 8(7):543–557, 2009. ISSN 14761122. doi: 10.1038/nmat2442.
- [67] Sergio Anguissola, David Garry, Anna Salvati, Peter J. O’Brien, and Kenneth A Dawson. High content analysis provides mechanistic insights on the pathways of toxicity induced by amine-modified polystyrene nanoparticles. *PLoS ONE*, 9(9), 2014. ISSN 19326203. doi: 10.1371/journal.pone.0108025.

- [68] Pakatip Ruenraroengsak, Pavel Novak, Deborah Berhanu, Andrew J Thorley, Eugenia Valsami-Jones, Julia Gorelik, Yuri E Korchev, and Teresa D Tetley. Respiratory epithelial cytotoxicity and membrane damage (holes) caused by amine-modified nanoparticles. *Nanotoxicology*, 6(1):94–108, feb 2012. ISSN 1743-5390. doi: 10.3109/17435390.2011.558643.
- [69] Fengjuan Wang, Lu Yu, Marco P. Monopoli, Peter Sandin, Eugene Mahon, Anna Salvati, and Kenneth A. Dawson. The biomolecular corona is retained during nanoparticle uptake and protects the cells from the damage induced by cationic nanoparticles until degraded in the lysosomes. *Nanomedicine: Nanotechnology, Biology, and Medicine*, 9(8):1159–1168, 2013. ISSN 15499634. doi: 10.1016/j.nano.2013.04.010.
- [70] Fengjuan Wang, Mariana G Bexiga, Sergio Anguissola, Patricia Boya, Jeremy C Simpson, and Kenneth A Dawson. Time resolved study of cell death mechanisms induced by amine-modified polystyrene nanoparticles. *Nanoscale*, pages 10868–10876, 2013.
- [71] Silvia Milani, Francesca Baldelli Bombelli, Andrzej S. Pitek, Kenneth A. Dawson, and Joachim Rädler. Reversible versus irreversible binding of transferrin to polystyrene nanoparticles: Soft and hard corona. *ACS Nano*, 6(3):2532–2541, 2012. ISSN 19360851. doi: 10.1021/nn204951s.
- [72] Jong Ah Kim, Aberg Christoffer, Guillermo de Carcer, Marcos Malumbres, Anna Salvati, and Kenneth a Dawson. Low Dose of Amino-Modified Nanoparticles Induces Cell Cycle Arrest. *ACS nano*, 7(9):7483–7494, 2013. doi: 10.1021/nn403126e.
- [73] Yuexian Liu, Wei Li, Fang Lao, Ying Liu, Liming Wang, Ru Bai, Yuliang Zhao, and Chunying Chen. Intracellular dynamics of cationic and anionic polystyrene nanoparticles without direct interaction with mitotic spindle and chromosomes. *Biomaterials*, 32(32):8291–8303, 2011. ISSN 01429612. doi: 10.1016/j.biomaterials.2011.07.037.
- [74] Oleg Lunov, Tatiana Syrovets, Cornelia Loos, G. Ulrich Nienhaus, Volker Mailänder, Katharina Landfester, Mustapha Rouis, and Thomas Simmet. Amino-functionalized polystyrene nanoparticles activate the NLRP3 inflammasome in human macrophages. *ACS Nano*, 5(12):9648–9657, 2011. ISSN 19360851. doi: 10.1021/nn203596e.
- [75] Akin Akinc, Mini Thomas, Alexander M. Klibanov, and Robert Langer. Exploring polyethylenimine-mediated DNA transfection and the proton sponge hypothesis. *Journal of Gene Medicine*, 7(5):657–663, 2005. ISSN 1099498X. doi: 10.1002/jgm.696.

-
- [76] Ming Zhao, Fernando Antunes, John W Eaton, and Ulf T Brunk. Lysosomal enzymes promote mitochondrial oxidant production , cytochrome c release and apoptosis. *Eur. J. Biochem.* 270), 3786:3778–3786, 2003. doi: 10.1046/j.1432-1033.2003.03765.x.
- [77] Heidi K Baumgartner, Julia V Gerasimenko, Christopher Thorne, Louise H Ashurst, Stephanie L Barrow, Michael a Chvanov, Stuart Gillies, David N Criddle, Alexei V Tepikin, Ole H Petersen, Robert Sutton, Alastair J M Watson, and Oleg V Gerasimenko. Caspase-8-mediated apoptosis induced by oxidative stress is independent of the intrinsic pathway and dependent on cathepsins. *American journal of physiology. Gastrointestinal and liver physiology*, 293(1): G296–G307, 2007. ISSN 0193-1857. doi: 10.1152/ajpgi.00103.2007.
- [78] Joachim Manns, Merle Daubrawa, Stefan Driessen, Florian Paasch, Nadine Hoffmann, Antje Löffler, Kirsten Lauber, Alexandra Dieterle, Sebastian Alers, Thomas Iftner, Klaus Schulze-Osthoff, Björn Stork, and Sebastian Wesselborg. Triggering of a novel intrinsic apoptosis pathway by the kinase inhibitor staurosporine: activation of caspase-9 in the absence of Apaf-1. *The FASEB journal : official publication of the Federation of American Societies for Experimental Biology*, 25(9):3250–3261, 2011. ISSN 0892-6638. doi: 10.1096/fj.10-177527.
- [79] I Kruman, Q Guo, and M P Mattson. Calcium and reactive oxygen species mediate staurosporine-induced mitochondrial dysfunction and apoptosis in PC12 cells. *J Neurosci Res*, 51(3):293–308, 1998. doi: 10.1002/(SICI)1097-4547(19980201)51:3<293::AID-JNR3>3.0.CO;2-B[pil].
- [80] A-C Johansson, H Steen, K Llinger, and K Roberg. Cathepsin D mediates cytochrome c release and caspase activation in human fibroblast apoptosis induced by staurosporine. *Cell Death and Differentiation*, 10:1253–1259, 2003. ISSN 1350-9047. doi: 10.1038/.
- [81] Â Ahmed Belmokhtar, Josette Hillion, and Evelyne Se. Staurosporine induces apoptosis through both caspase-dependent and caspase-independent mechanisms. *Oncogene*, pages 3354–3362, 2001.
- [82] Su Ryeon Seo and Jeong Taeg Seo. Calcium overload is essential for the acceleration of staurosporine-induced cell death following neuronal differentiation in PC12 cells. *Experimental and Molecular Medicine*, 41(4):269–276, 2009. ISSN 20926413. doi: 10.3858/emm.2009.41.4.030.
- [83] Magdalena L. Circu and Tak Yee Aw. Reactive oxygen species, cellular redox systems, and apoptosis. *Free Radical Biology and Medicine*, 48(6):749–762, 2010. ISSN 08915849. doi: 10.1016/j.freeradbiomed.2009.12.022.

- [84] I N Lavrik and P H Krammer. Regulation of CD95/Fas signaling at the DISC. *Cell Death and Differentiation*, 19(1):36–41, 2012. ISSN 1350-9047. doi: 10.1038/cdd.2011.155.
- [85] M E Peter, A Hadji, a E Murmann, S Brockway, W Putzbach, A Pattanayak, and P Ceppi. The role of CD95 and CD95 ligand in cancer. *Cell death and differentiation*, 22(4):549–59, 2015. ISSN 1476-5403. doi: 10.1038/cdd.2015.3.
- [86] Naoto Itoh, Shin Yonehara, Ai Ishii, Minako Yonehara, Sei Ichi Mizushima, Masazumi Sameshima, Atsushi Hase, Yoshiyuki Seto, and Shigekazu Nagata. The polypeptide encoded by the cDNA for human cell surface antigen Fas can mediate apoptosis. *Cell*, 66(2):233–243, 1991. ISSN 00928674. doi: 10.1016/0092-8674(91)90614-5.
- [87] M. E. Peter and P. H. Krammer. The CD95(APO-1/Fas) DISC and beyond. *Cell Death & Differentiation*, 10(1):26–35, 2003. ISSN 1350-9047. doi: 10.1038/sj.cdd.4401186.
- [88] D. Berg, M. Lehne, N. Müller, D. Siegmund, S. Münkkel, W. Sebald, K. Pfizenmaier, and H. Wajant. Enforced covalent trimerization increases the activity of the TNF ligand family members TRAIL and CD95L. *Cell Death and Differentiation*, 14(12):2021–2034, 2007. ISSN 13509047. doi: 10.1038/sj.cdd.4402213.
- [89] F. C. Kischkel, S. Hellbardt, I. Behrmann, M. Germer, M. Pawlita, P. H. Krammer, and M. E. Peter. Cytotoxicity-dependent APO-1 (Fas/CD95)-associated proteins form a death-inducing signaling complex (DISC) with the receptor. *The EMBO Journal*, 14(22):5579–5588, 1995. ISSN 02614189. doi: 10.1002/j.1460-2075.1995.tb00245.x.
- [90] Carsten Scaffidi, Simone Fulda, Anu Srinivasan, Claudia Friesen, Feng Li, Kevin J Tomaselli, Klaus-michael Debatin, Peter H Krammer, and Marcus E Peter. Two CD95 (APO-1 / Fas) signaling pathways. *EMBO Journal*, 17(6): 1675–1687, 1998.
- [91] Jiang J., Kini V., Belikova N., Serinkan B.F., Borisenko G.G., Tyurina Y.Y., Tyurin V.A., and Kagan V.E. Cytochrome c release is required for phosphatidylserine peroxidation during Fas-triggered apoptosis in lung epithelial A549 cells. *Lipids*, 39(11):1133–1142, 2004.
- [92] Harald Wajant. The Fas signaling pathway: more than a paradigm. *Science*, 296(5573):1635–1636, 2002. ISSN 00368075. doi: 10.1126/science.1071553.
- [93] S Nagata and P Golstein. The Fas death factor. *Science (New York, N.Y.)*, 267(5203):1449–1456, 1995. ISSN 0036-8075. doi: 10.1126/science.7533326.

-
- [94] S Nagata. Fas ligand-induced apoptosis. *Annual Review of Genetics*, 32:29–55, 1999. ISSN 0066-4197. doi: 10.1146/annurev.genet.33.1.29.
- [95] Bryan C. Barnhart, Elizabeth C. Alappat, and Marcus E. Peter. The CD95 Type I/Type II model. *Seminars in Immunology*, 15(3):185–193, 2003. ISSN 10445323. doi: 10.1016/S1044-5323(03)00031-9.
- [96] Bryan C. Barnhart, Patrick Legembre, Eric Pietras, Concetta Bubici, Guido Franzoso, and Marcus E. Peter. CD95 ligand induces motility and invasiveness of apoptosis-resistant tumor cells. *EMBO Journal*, 23(15):3175–3185, 2004. ISSN 02614189. doi: 10.1038/sj.emboj.7600325.
- [97] Stefanie Wagner, Jonathan Bloh, Cornelia Kasper, and Detlef Bahnemann. Toxicological issues of nanoparticles employed in photocatalysis. *Green*, 1(2): 171–188, 2011. ISSN 18698778. doi: 10.1515/GREEN.2011.013.
- [98] Leroy F. Liu, Xuan Fu, Shan Wan, Haiyan Qi, and Yi Lisa Lyu. Etoposide Induces ATM-Dependent Mitochondrial Biogenesis through AMPK Activation. *PLoS ONE*, 3(4):e2009, 2008. doi: 10.1371/journal.pone.0002009.
- [99] Takashi Nakagawa, Shigeomi Shimizu, Tetsuya Watanabe, Osamu Yamaguchi, Kinya Otsu, Hirotaka Yamagata, Hidenori Inohara, Takeshi Kubo, and Yoshihide Tsujimoto. Cyclophilin D-dependent mitochondrial permeability transition regulates some necrotic but not apoptotic cell death. *Nature*, 434(7033): 652–658, 2005. ISSN 00280836. doi: 10.1038/nature03317.
- [100] O Nagano, S Okazaki, and H Saya. Redox regulation in stem-like cancer cells by CD44 variant isoforms. *Oncogene*, 32(44):5191–8, 2013. ISSN 1476-5594. doi: 10.1038/onc.2012.638.
- [101] F Antunes, E Cadenas, and U T Brunk. Apoptosis induced by exposure to a low steady-state concentration of H₂O₂ is a consequence of lysosomal rupture. *The Biochemical journal*, 356(Pt 2):549–555, 2001. ISSN 02646021. doi: 10.1042/0264-6021:3560549.
- [102] K Roberg and K Ollinger. Oxidative stress causes relocation of the lysosomal enzyme cathepsin D with ensuing apoptosis in neonatal rat cardiomyocytes. *The American Journal of Pathology*, 152(5):1151–1156, 1998. ISSN 0002-9440.
- [103] K Arin R Roberg, U no Johansson, and Karin Ollinger. Lysosomal Release of Cathepsin D Precedes Relocation of Potential During Apoptosis Induced By Oxidative Stress. *Free radical biology & medicine*, 27(11-12):1228–1237, 1999.
- [104] Boris Turk, Veronica Stoka, Jerica Rozman-Pungerčar, Tina Cirman, Gabriela Droga-Mazovec, Kristina Orešić, and Vito Turk. Apoptotic pathways: Involvement of lysosomal proteases. *Biological Chemistry*, 383(7-8):1035–1044, 2002. ISSN 14316730. doi: 10.1515/BC.2002.112.

- [105] C. E. Chwieralski, T. Welte, and F. Bühling. Cathepsin-regulated apoptosis. *Apoptosis*, 11(2):143–149, 2006. ISSN 13608185. doi: 10.1007/s10495-006-3486-y.
- [106] Karin Roberg, Katarina Kågedal, and Karin Öllinger. Microinjection of cathepsin d induces caspase-dependent apoptosis in fibroblasts. *The American journal of pathology*, 161(1):89–96, 2002. ISSN 0002-9440. doi: 10.1016/S0002-9440(10)64160-0.
- [107] Nicolas Bidère, Hans K. Lorenzo, Sylvie Carmona, Mireille Laforge, Francis Harper, Céline Dumont, and Anna Senik. Cathepsin D triggers Bax activation, resulting in selective apoptosis-inducing factor (AIF) relocation in T lymphocytes entering the early commitment phase to apoptosis. *Journal of Biological Chemistry*, 278(33):31401–31411, 2003. ISSN 00219258. doi: 10.1074/jbc.M301911200.
- [108] Karin Öllinger. Inhibition of cathepsin D prevents free-radical-induced apoptosis in rat cardiomyocytes. *Archives of Biochemistry and Biophysics*, 373(2): 346–351, 2000. ISSN 00039861. doi: 10.1006/abbi.1999.1567.
- [109] K. Kagedal. The lysosomal protease cathepsin D mediates apoptosis induced by oxidative stress. *The FASEB Journal*, 15(5), 2001. ISSN 15306860. doi: 10.1096/fj.00-0708fje.
- [110] U.T. Brunk and I. Svensson. Oxidative stress, growth factor starvation and Fas activation may all cause apoptosis through lysosomal leak. *Redox Report*, 4(1-2):3–11, 1999. ISSN 1351-0002. doi: 10.1179/135100099101534675.
- [111] Nicolas Bidère, Hans K. Lorenzo, Sylvie Carmona, Mireille Laforge, Francis Harper, Céline Dumont, and Anna Senik. Cathepsin D triggers Bax activation, resulting in selective apoptosis-inducing factor (AIF) relocation in T lymphocytes entering the early commitment phase to apoptosis. *Journal of Biological Chemistry*, 278(33):31401–31411, 2003. ISSN 00219258. doi: 10.1074/jbc.M301911200.
- [112] U.T. Brunk, J. Neuzil, and J.W. Eaton. Lysosomal involvement in apoptosis. *Redox Report*, 6(2):91–97, 2001. ISSN 1351-0002. doi: 10.1179/135100001101536094.
- [113] L P Deiss, H Galinka, H Berissi, O Cohen, and A Kimchi. Cathepsin D protease mediates programmed cell death induced by interferon-gamma, Fas/APO-1 and TNF-alpha. *the The European Molecular Biology Organization Journal*, 15(15):3861–3870, 1996. ISSN 0261-4189.
- [114] Lea Bojič, Ana Petelin, Veronika Stoka, Thomas Reinheckel, Christoph Peters, Vito Turk, and Boris Turk. Cysteine cathepsins are not involved in Fas/CD95

- signalling in primary skin fibroblasts. *FEBS Letters*, 581(27):5185–5190, 2007. ISSN 00145793. doi: 10.1016/j.febslet.2007.10.005.
- [115] K R Hande. Clinical Oncology Update Etoposide : Four Decades of Development of a Topoisomerase II Inhibitor. *European Journal of Cancer*, 34(10):1514–1521, 1998.
- [116] John L. Nitiss. Targeting DNA topoisomerase II in cancer chemotherapy. *Nature Reviews Cancer*, 9(5):338–350, 2009. ISSN 1474175X. doi: 10.1038/nrc2607.
- [117] Scott H. Kaufmann. Cell death induced by topoisomerase-targeted drugs: More questions than answers. *Biochimica et Biophysica Acta - Gene Structure and Expression*, 1400(1-3):195–211, 1998. ISSN 01674781. doi: 10.1016/S0167-4781(98)00136-5.
- [118] Grant R. Zimmermann, Joseph Lehár, and Curtis T. Keith. Multi-target therapeutics: when the whole is greater than the sum of the parts. *Drug Discovery Today*, 12(1-2):34–42, 2007. ISSN 13596446. doi: 10.1016/j.drudis.2006.11.008.
- [119] Andrew L. Hopkins. Network pharmacology: The next paradigm in drug discovery. *Nature Chemical Biology*, 4(11):682–690, 2008. ISSN 15524469. doi: 10.1038/nchembio.118.
- [120] Feng Zhu, Jia Jia, Yu Zong Chen, Zhiwei W. Cao, Xiaohua Ma, and Yixue X. Li. Mechanisms of drug combinations: interaction and network perspectives. *Nature Reviews Drug Discovery*, 8(2):111–128, 2009. ISSN 1474-1776. doi: 10.1038/nrd2683.
- [121] Albert László Barabási, Natali Gulbahce, and Joseph Loscalzo. Network medicine: A network-based approach to human disease. *Nature Reviews Genetics*, 12(1):56–68, 2011. ISSN 14710056. doi: 10.1038/nrg2918.
- [122] Jürgen Eirich, Simone Braig, Liliana Schyschka, Phil Servatius, Judith Hoffmann, Sabrina Hecht, Simone Fulda, Stefan Zahler, Iris Antes, Uli Kazmaier, Stephan A. Sieber, and Angelika M. Vollmar. A small molecule inhibits protein disulfide isomerase and triggers the chemosensitization of cancer cells. *Angewandte Chemie - International Edition*, 53(47):12960–12965, 2014. ISSN 15213773. doi: 10.1002/anie.201406577.
- [123] Mark D. McDonnell and Derek Abbott. What is stochastic resonance? Definitions, misconceptions, debates, and its relevance to biology. *PLoS Computational Biology*, 5(5), 2009. ISSN 1553734X. doi: 10.1371/journal.pcbi.1000348.
- [124] C V Wolf D M Arkin A P Rao. Control, exploitation and tolerance of intracellular noise. *Nature*, 421(6919):190, 2002.

- [125] Suzanne Gaudet, Sabrina L. Spencer, William W. Chen, and Peter K. Sorger. Exploring the contextual sensitivity of factors that determine cell-to-cell variability in receptor-mediated apoptosis. *PLoS Computational Biology*, 8(4), 2012. ISSN 1553734X. doi: 10.1371/journal.pcbi.1002482.
- [126] X. Xia, M. S. Owen, R. E.C. Lee, and S. Gaudet. Cell-to-cell variability in cell death: Can systems biology help us make sense of it all? *Cell Death and Disease*, 5(5):e1261–11, 2014. ISSN 20414889. doi: 10.1038/cddis.2014.199.
- [127] M. L. Würstle, E. Zink, J. H.M. Prehn, and M. Rehm. From computational modelling of the intrinsic apoptosis pathway to a systems-based analysis of chemotherapy resistance: Achievements, perspectives and challenges in systems medicine. *Cell Death and Disease*, 5:1–11, 2014. ISSN 20414889. doi: 10.1038/cddis.2014.36.
- [128] M.D. Dana S. Thompson, M.D., John D. Hainsworth, M.D., Kenneth R. Hande, M.D., May Holzmer, R.N., t and F. Anthony Greco. Prolonged administration of low dose infusional etoposide in patients with advanced malignancies: A phase I/II study. *Cancer*, 73(11):2824–2831, 1994. ISSN 0008-543X. doi: 10.1002/1097-0142(19940601)73:11<2824::AID-CNCR2820731127>3.0.CO;2-T.
- [129] C. I. Bliss. The toxicity of poisons applied jointly. *Annals of applied biology*, 26(3):585–615, 1939.
- [130] P. Pacher and G. Hajnóczky. Propagation of the apoptotic signal by mitochondrial waves. *EMBO Journal*, 20(15):4107–4121, 2001. ISSN 02614189. doi: 10.1093/emboj/20.15.4107.
- [131] David E. Clapham. Calcium signaling. *Cell*, 131:1047–1058, 2007. doi: 10.1201/9781420038231.
- [132] György Hajnóczky, Erika Davies, and Muniswamy Madesh. Calcium signaling and apoptosis. *Biochemical and Biophysical Research Communications*, 304(3):445–454, 2003. ISSN 0006291X. doi: 10.1016/S0006-291X(03)00616-8.
- [133] G Hajnóczky, G Csordás, M Madesh, and P Pacher. Control of apoptosis by IP(3) and ryanodine receptor driven calcium signals. *Cell calcium*, 28(5-6): 349–63, 2000. ISSN 0143-4160. doi: 10.1054/ceca.2000.0169.
- [134] Rosario Rizzuto, Diego De Stefani, Anna Raffaello, and Cristina Mammucari. Mitochondria as sensors and regulators of calcium signalling. *Nature Reviews Molecular Cell Biology*, 13(9):566–578, 2012. ISSN 14710072. doi: 10.1038/nrm3412. URL <http://dx.doi.org/10.1038/nrm3412>.

-
- [135] D. Chandra, B. Bhatia, X. Deng, G. Choy, D. G. Tang, and P. Daniel. Association of Active Caspase 8 with the Mitochondrial Membrane during Apoptosis: Potential Roles in Cleaving BAP31 and Caspase 3 and Mediating Mitochondrion-Endoplasmic Reticulum Cross Talk in Etoposide-Induced Cell Death. *Molecular and Cellular Biology*, 24(15):6592–6607, 2004. ISSN 0270-7306. doi: 10.1128/mcb.24.15.6592-6607.2004.
- [136] N. Yadav, S. Kumar, T. Marlowe, A. K. Chaudhary, R. Kumar, J. Wang, J. O’Malley, P. M. Boland, S. Jayanthi, T. K.S. Kumar, N. Yadava, and D. Chandra. Oxidative phosphorylation-dependent regulation of cancer cell apoptosis in response to anticancer agents. *Cell Death and Disease*, 6(11): e1969–13, 2015. ISSN 20414889. doi: 10.1038/cddis.2015.305.
- [137] Petra S Dittrich and Andreas Manz. Lab-on-a-chip : microfluidics in drug discovery. *Nature*, 5(March):210–218, 2006. doi: 10.1038/nrd1985.
- [138] Mirren Charnley, Marcus Textor, and Matthias P Lutolf. Integration column : microwell arrays for mammalian cell culture. *Integrative Biology*, pages 625–634, 2009. doi: 10.1039/b918172p.
- [139] Elisavet I. Chatzopoulou, Claudia C. Roskopf, Farzad Sekhavati, Todd A. Bra-ciak, Nadja C. Fenn, Karl Peter Hopfner, Fuat S. Oduncu, Georg H. Fey, and Joachim O. Rädler. Chip-based platform for dynamic analysis of NK cell cytotoxicity mediated by a triplebody. *Analyst*, 141(7):2284–2295, 2016. ISSN 13645528. doi: 10.1039/c5an02585k.
- [140] E. I. Chatzopoulou, P. Raharja-Liu, A. Murschhauser, F. Sekhavati, F. Buggenthin, A. M. Vollmar, C. Marr, and J. O. Rädler. A single-cell micro-trench platform for automatic monitoring of cell division and apoptosis after chemotherapeutic drug administration. *Scientific Reports*, 8(1):1–10, 2018. ISSN 20452322. doi: 10.1038/s41598-018-36508-8.
- [141] Farzad Sekhavati, Max Endeke, Susanne Rappl, Anna Kristina Marel, Timm Schroeder, and Joachim O. Rädler. Marker-free detection of progenitor cell differentiation by analysis of Brownian motion in micro-wells. *Integrative Biology (United Kingdom)*, 7(2):178–183, 2015. ISSN 17579708. doi: 10.1039/c4ib00158c.
- [142] Abraham D Jessamine M. K. Ng, Irina Gitlin, Stroock and George M Whitesides. Review Components for integrated poly (dimethylsiloxane) microfluidic systems. *Electrophoresis*, 23:3461–3473, 2010.
- [143] George M Whitesides Stroock and Abraham D. Flexible Methods for Microfluidics. *Physics Today*, June(2001):42–48, 2001. doi: 10.1063/1.1387591.

- [144] Younan Xia and George M. Whitesides. Soft Lithography. *Annual Review of Materials Science*, 28(1):153–184, 2002. ISSN 0084-6600. doi: 10.1146/annurev.matsci.28.1.153.
- [145] Samuel K. Sia and George M. Whitesides. Microfluidic devices fabricated in poly(dimethylsiloxane) for biological studies. *Electrophoresis*, 24(21):3563–3576, 2003. ISSN 01730835. doi: 10.1002/elps.200305584.
- [146] J C McDonald and G M Whitesides. PDMS as a Material for Fabricating Microfluidic Devices. *Accounts of Chemical Research*, 35(7):491–499, 2002.
- [147] J. Cooper McDonald, David C. Duffy, Janelle R. Anderson, Daniel T. Chiu, Hongkai Wu, Olivier J.A. Schueller, and George M. Whitesides. Review General Fabrication of microfluidic systems in poly (dimethylsiloxane). *Electrophoresis*, 21:27–40, 2000.
- [148] Duffy DC, McDonald JC, Schueller OJA, and Whitesides GM. Rapid prototyping of microfluidic systems in poly(dimethylsiloxane). *Analytical Chemistry*, 70(23):4974–4984, 1998.
- [149] Keil J. Regehr, Maribella Domenech, Justin T. Koepsel, Kristopher C. Carver, Stephanie J. Ellison-Zelski, William L. Murphy, Linda A. Schuler, Elaine T. Alarid, and David J. Beebe. Biological implications of polydimethylsiloxane-based microfluidic cell culture. *Lab on a Chip*, 9(15):2132–2139, 2009. ISSN 14730189. doi: 10.1039/b903043c.
- [150] Skarphedinn Halldorsson, Edinson Lucumi, Rafael Gómez-Sjöberg, and Roman M.T. Fleming. Advantages and challenges of microfluidic cell culture in polydimethylsiloxane devices. *Biosensors and Bioelectronics*, 63:218–231, 2015. ISSN 18734235. doi: 10.1016/j.bios.2014.07.029.
- [151] Patrick A. Limbach, Chong Ahn, William R. Heineman, Carl J. Seliskar, Se Hwan Lee, Aigars Piruska, and Irena Nikcevic. The autofluorescence of plastic materials and chips measured under laser irradiation. *Lab on a Chip*, 5(12):1348, 2005. ISSN 1473-0197. doi: 10.1039/b508288a.
- [152] Jessamine Ng Lee, Xingyu Jiang, Declan Ryan, and George M. Whitesides. Compatibility of mammalian cells on surfaces of poly(dimethylsiloxane). *Langmuir*, 20(26):11684–11691, 2004. ISSN 07437463. doi: 10.1021/la048562+.
- [153] Enoch Kim, Younan Xia, and G.m. Whitesides: Micromolding in capillaries: Applications in materials science. *J. Am. Chem. Soc.*, 118:5722(Figure 1): 5722–5731, 1996.
- [154] Elisavet Chatzopoulou. *Single-cell arrays for dynamic analysis of cell processes*. PhD thesis, LMU Munich, 2018.

-
- [155] Farzad Sekhavati. *Dynamic response of individual cells in heterogeneous population*. PhD thesis, LMU Munich, 2015.
- [156] Won-gun Koh, Alexander Revzin, and Michael V Pishko. Poly (ethylene glycol) Hydrogel Microstructures Encapsulating Living Cells. *Society*, 18(February): 2459–2462, 2002. doi: 10.1021/la0115740.
- [157] Won-gun Koh, Alexander Revzin, Tony Reeves, and Michael Pishko. BioMEMs Materials and Fabrication Technology : Control of Mammalian Cell and Bacteria Adhesion on Substrates Micropatterned with Poly (ethylene glycol) Hydrogels. *Biomedical Microdevices*, pages 11–19, 2003.
- [158] Alexander Revzin, Ryan J. Russell, Vamsi K. Yadavalli, Won Gun Koh, Curt Deister, David D. Hile, Michael B. Mellott, and Michael V. Pishko. Fabrication of poly(ethylene glycol) hydrogel microstructures using photolithography. *Langmuir*, 17(18):5440–5447, 2001. ISSN 07437463. doi: 10.1021/la010075w.
- [159] Alexander Revzin, Ronald G Tompkins, and Mehmet Toner. Surface Engineering with Poly (ethylene glycol) Photolithography to Create High-Density Cell Arrays on Glass Surface Engineering with Poly (ethylene glycol) Photolithography to Create High-Density Cell Arrays on Glass. *Langmuir*, 19(23): 9855–9862, 2003. doi: 10.1021/la035129b.
- [160] A Revzin, K Sekine, A Sin, R G Tompkins, and M Toner. Development of a microfabricated cytometry platform for characterization and sorting of individual leukocytes. *Lab on a Chip*, 5(1):30–37, 2005. ISSN 1473-0197. doi: 10.1039/b405557h.
- [161] Andrea Ravasio, Sree Vaishnavi, Benoit Ladoux, and Virgile Viasnoff. High-resolution imaging of cellular processes across textured surfaces using an indexed-matched elastomer. *Acta Biomaterialia*, 14:53–60, 2015. ISSN 18787568. doi: 10.1016/j.actbio.2014.11.006.
- [162] Petra Schwill, Armin Lambacher, Jonas Mücksch, Philipp Blumhardt, Christian Niederauer, and Michael Heymann. Direct characterization of the evanescent field in objective-type total internal reflection fluorescence microscopy. *Optics Express*, 26(16):20492, 2018. doi: 10.1364/oe.26.020492.
- [163] Cuong Cao, Sam W Birtwell, Jonas Høgberg, Anders Wolff, Hywel Morgan, and Dang Duong Bang. Surface Modification of Photoresist Su-8 for Low Autofluorescence and Bioanalytical Applications. *Micro Total Analysis Systems 2011*, pages 1161–1163, 2011.
- [164] Marc Hennemeyer, Ferdinand Walther, Sandra Kerstan, Katrin Schürzinger, Alexander M. Gigler, and Robert W. Stark. Cell proliferation assays on plasma

- activated SU-8. *Microelectronic Engineering*, 85(5-6):1298–1301, 2008. ISSN 01679317. doi: 10.1016/j.mee.2008.01.026.
- [165] Krishnamurthy V. Nemani, Karen L. Moodie, Jeffery B. Brennick, Alison Su, and Barjor Gimi. In vitro and in vivo evaluation of SU-8 biocompatibility. *Materials Science and Engineering C*, 33(7):4453–4459, 2013. ISSN 09284931. doi: 10.1016/j.msec.2013.07.001.
- [166] Ming Ni, Wen Hao Tong, Deepak Choudhury, Nur Aida Abdul Rahim, Ciprian Iliescu, and Henry Yu. Cell culture on MEMS platforms: A review. *International Journal of Molecular Sciences*, 10(12):5411–5441, 2009. ISSN 14220067. doi: 10.3390/ijms10125411.
- [167] Michael Stangegaard, Z. Wang, J. P. Kutter, M. Dufva, and A. Wolff. Whole genome expression profiling using DNA microarray for determining biocompatibility of polymeric surfaces. *Molecular BioSystems*, 2(9):421–428, 2006. ISSN 1742206X. doi: 10.1039/b608239d.
- [168] Xin-Hong Cui Wei Zhang, Bang Xiong, Wen-Fang Sun, Shuai An, Kuang-Fei Lin, Mei-Jin Guo. Acute and Chronic Toxic Effects of Bisphenol A on *Chlorella pyrenoidosa* and *Scenedesmus obliquus*. *Environmental toxicology*, 29(6):714–722, 2014. ISSN 1522-7278. doi: 10.1002/tox.
- [169] Homa Darmani and Ahmad S. Al-Hiyasat. Reproductive toxic effect of bisphenol A dimethacrylate in mice. *Journal of Biomedical Materials Research - Part A*, 69(4):637–643, 2004. ISSN 00219304. doi: 10.1002/jbm.a.30029.
- [170] Nora Benachour and Aziz Aris. Toxic effects of low doses of Bisphenol-A on human placental cells. *Toxicology and Applied Pharmacology*, 241(3):322–328, 2009. ISSN 0041008X. doi: 10.1016/j.taap.2009.09.005.
- [171] Vicki I. Chin, Philippe Taupin, Sandeep Sanga, John Scheel, Fred H. Gage, and Sangeeta N. Bhatia. Microfabricated platform for studying stem cell fates. *Biotechnology and Bioengineering*, 88(3):399–415, 2004. ISSN 00063592. doi: 10.1002/bit.20254.
- [172] Ferdinand Walther, Polina Davydovskaya, Stefan Zürcher, Michael Kaiser, Helmut Herberg, Alexander M. Gigler, and Robert W. Stark. Stability of the hydrophilic behavior of oxygen plasma activated SU-8. *Journal of Micromechanics and Microengineering*, 17(3):524–531, 2007. ISSN 09601317. doi: 10.1088/0960-1317/17/3/015.
- [173] Sarah L. Tao, Ketul C. Popat, James J. Norman, and Tejal A. Desai. Surface modification of SU-8 for enhanced biofunctionality and nonfouling properties. *Langmuir*, 24(6):2631–2636, 2008. ISSN 07437463. doi: 10.1021/la703066z.

-
- [174] Frederik Kotz, Klaus Plewa, Werner Bauer, Norbert Schneider, Nico Keller, Tobias Nargang, Dorothea Helmer, Kai Sachsenheimer, Michael Schäfer, Matthias Worgull, Christian Greiner, Christiane Richter, and Bastian E. Rapp. Liquid Glass: A Facile Soft Replication Method for Structuring Glass. *Advanced Materials*, pages 4646–4650, 2016. ISSN 15214095. doi: 10.1002/adma.201506089.
- [175] Nico Keller, Frederik Kotz, Dieter Schild, Bastian E. Rapp, Kai Sachsenheimer, Dorothea Helmer, Karl Arnold, Werner Bauer, Christiane Richter, and Tobias M. Nargang. Three-dimensional printing of transparent fused silica glass. *Nature*, 544(7650):337–339, 2017. ISSN 0028-0836. doi: 10.1038/nature22061.
- [176] Wacker. Solid and liquid silicone rubber material and processing guidelines. *Product Datasheet*, page 104, 2014.
- [177] Frédéric Jamme, Slavka Kascakova, Sandrine Villette, Fatma Allouche, Stéphane Pallu, Valérie Rouam, and Matthieu Réfrégiers. Deep UV autofluorescence microscopy for cell biology and tissue histology. *Biology of the Cell*, 105(7):277–288, 2013. ISSN 02484900. doi: 10.1111/boc.201200075.
- [178] W. B. Amos, J. G. White, and M. Fordham. Use of confocal imaging in the study of biological structures. *Applied Optics*, 26(16):3239, 2009. ISSN 0003-6935. doi: 10.1364/ao.26.003239.
- [179] Bo Lu, Siyang Zheng, Brandon Quoc Quach, and Yu Chong Tai. A study of the autofluorescence of parylene materials for μ TAS applications. *Lab on a Chip*, 10(14):1826–1834, 2010. ISSN 14730189. doi: 10.1039/b924855b.
- [180] Gabriela Blagoi, Stephan Keller, Alicia Johansson, Anja Boisen, and Martin Dufva. Functionalization of SU-8 photoresist surfaces with IgG proteins. *Applied Surface Science*, 255(5 PART 2):2896–2902, 2008. ISSN 01694332. doi: 10.1016/j.apsusc.2008.08.089.
- [181] Chad I. Rogers, Jayson V. Pagaduan, Gregory P. Nordin, and Adam T. Woolley. Single-monomer formulation of polymerized polyethylene glycol diacrylate as a nonadsorptive material for microfluidics. *Analytical Chemistry*, 83(16): 6418–6425, 2011. ISSN 00032700. doi: 10.1021/ac201539h.
- [182] Mirjam Ochsner, Marc R Dusseiller, H Michelle Grandin, Sheila Luna-Morris, Marcus Textor, Viola Vogel, and Michael L Smith. Micro-well arrays for 3D shape control and high resolution analysis of single cells. *Lab on a chip*, 7(8): 1074–1077, 2007. ISSN 1473-0197. doi: 10.1039/b704449f.
- [183] Markus Rottmar, Maria Håkanson, Michael Smith, and Katharina Maniura-Weber. Stem cell plasticity, osteogenic differentiation and the third dimension.

- Journal of Materials Science: Materials in Medicine*, 21(3):999–1004, 2010. ISSN 09574530. doi: 10.1007/s10856-009-3926-7.
- [184] Vincent Studer, Celine Stoecklin, Virgile Viasnoff, Zhang Yue, Wilhelm W. Chen, Eileen Fong, and Richard de Mets. A New Approach to Design Artificial 3D Microniches with Combined Chemical, Topographical, and Rheological Cues. *Advanced Biosystems*, 2(7):1700237, 2018. doi: 10.1002/adbi.201700237.
- [185] Sergei Doulatov, Faiyaz Notta, Elisa Laurenti, and John E. Dick. Hematopoiesis: A human perspective. *Cell Stem Cell*, 10(2):120–136, 2012. ISSN 19345909. doi: 10.1016/j.stem.2012.01.006.
- [186] Donald Metcalf. On Hematopoietic Stem Cell Fate. *Immunity*, 26(6):669–673, 2007. ISSN 10747613. doi: 10.1016/j.immuni.2007.05.012.
- [187] Stuart H. Orkin and Leonard I. Zon. Hematopoiesis: An Evolving Paradigm for Stem Cell Biology. *Cell*, 132(4):631–644, 2008. ISSN 00928674. doi: 10.1016/j.cell.2008.01.025.
- [188] By Shiang Huang, Ping Law, Karl Francis, Bernhard O Palsson, and Anthony D Ho. Symmetry of Initial Cell Divisions Among Primitive Hematopoietic Progenitors. *Blood*, 94(8):2595–2604, 1999.
- [189] Anne Wilson, Maike Jaworski, Leonid Eshkind, Ernesto Bockamp, Andreas Trumpp, H. Robson MacDonald, William Blanco-Bose, Sandra Offner, Cyrille F. Dunant, Richard C. van der Wath, Pietro Lió, Elisa Laurenti, and Gabriela Oser. Hematopoietic Stem Cells Reversibly Switch from Dormancy to Self-Renewal during Homeostasis and Repair. *Cell*, 135(6):1118–1129, 2008. ISSN 00928674. doi: 10.1016/j.cell.2008.10.048.
- [190] Sean J. Morrison Nobuko Uchida Weissman and Irving L. The biology of hematopoietic stem cells. *Annu. Rev. Cell Dev. Biol.*, 11:35–71, 1995.
- [191] Yifan Zhang, Shuai Gao, Jun Xia, and Feng Liu. Hematopoietic Hierarchy – An Updated Roadmap. *Trends in Cell Biology*, 28(12):976–986, 2018. ISSN 18793088. doi: 10.1016/j.tcb.2018.06.001.
- [192] Christoph Lutz, Daniel Nowak, Eike C. Buss, Lars M. Steinmetz, Tobias Boch, Wolf-Karsten Hofmann, Simon Raffel, Lars Velten, Christoph Hirche, Andreas Trumpp, Sandra Blaszkiewicz, Saiful Islam, Bianca P. Hennig, Wolfgang Huber, Simon F. Haas, Marieke A. G. Essers, and Anthony D. Ho. Human haematopoietic stem cell lineage commitment is a continuous process. *Nature Cell Biology*, 19(4):271–281, 2017. ISSN 1465-7392. doi: 10.1038/ncb3493.
- [193] Lambert F.R. Span, Gertie Vierwinden, Arie H. Pennings, Jan B.M. Boezeman, Reinier A.P. Raymakers, and Theo De Witte. Programmed cell death is

- an intrinsic feature of MDS progenitors, predominantly found in the cluster-forming cells. *Experimental Hematology*, 33(4):435–442, 2005. ISSN 0301472X. doi: 10.1016/j.exphem.2004.12.009.
- [194] Wolf-K. Hofmann Koeffler and H. Philipp. Myelodysplastic Syndrome. *Annual Reviews Medicine*, 56:1–16, 2005. ISSN 00257125. doi: 10.1016/B978-0-323-47913-4.00018-5.
- [195] Maher Albitar, Taghi Manshouri, Yu Shen, Diane Liu, Miloslav Beran, Hagop M. Kantarjian, Anna Rogers, Iman Jilani, Chung Wu Lin, Sherry Pierce, Emil J. Freireich, and Elihu H. Estey. Myelodysplastic syndrome is not merely "preleukemia". *Blood*, 100(3):791–798, 2002. ISSN 00064971. doi: 10.1182/blood.V100.3.791.
- [196] Ingrid A M Denkers, Wieslawa Dragowska, Bruno Jaggi, Branko Palcic, and M Lansdorpb. Time lapse Video recordings of Highly Purified Human Hematopoietic Progenitor Cells in Culture. *Stem Cells*, 11:243–248, 1993.
- [197] C. Eaves, J. Ramunas, L. McCaffrey, K. Farn, L. Kelly, B. Dykstra, A. Blaylock, E. Jervis, E. Szumsky, and D. Kent. High-resolution video monitoring of hematopoietic stem cells cultured in single-cell arrays identifies new features of self-renewal. *Proceedings of the National Academy of Sciences*, 103(21):8185–8190, 2006. ISSN 0027-8424. doi: 10.1073/pnas.0602548103.
- [198] Matthias Kaiser, Florian Jug, Thomas Julou, Siddharth Deshpande, Thomas Pfohl, Olin K. Silander, Gene Myers, and Erik Van Nimwegen. Monitoring single-cell gene regulation under dynamically controllable conditions with integrated microfluidics and software. *Nature Communications*, 9(1), 2018. ISSN 20411723. doi: 10.1038/s41467-017-02505-0.
- [199] Bo Zhu, Jeremiah Z. Liu, Stephen F. Cauley, Bruce R. Rosen, and Matthew S. Rosen. Image reconstruction by domain-transform manifold learning. *Nature*, 555(7697):487–492, 2018. ISSN 14764687. doi: 10.1038/nature25988.
- [200] Thomas Blasi, Holger Hennig, Huw D. Summers, Fabian J. Theis, Joana Cerveira, James O. Patterson, Derek Davies, Andrew Filby, Anne E. Carpenter, and Paul Rees. Label-free cell cycle analysis for high-throughput imaging flow cytometry. *Nature Communications*, 7:1–9, 2016. ISSN 20411723. doi: 10.1038/ncomms10256.
- [201] Hirofumi Kobayashi, Cheng Lei, Yi Wu, Ailin Mao, Yiyue Jiang, Baoshan Guo, Yasuyuki Ozeki, and Keisuke Goda. Label-free detection of cellular drug responses by high-throughput bright-field imaging and machine learning. *Scientific Reports*, 7(1):1–9, 2017. ISSN 20452322. doi: 10.1038/s41598-017-12378-4.

- [202] Ilka Diester, Sean Walsh, Olaf Tietz, Alexander Dovzhenko, Özgün Çiçek, Ahmed Abdulkadir, Olaf Ronneberger, Anton Böhm, Klaus Palme, Thorsten Falk, Zoe Jäckel, Matias Simons, Deniz Saltukoglu, Marco Prinz, Jan Deubner, Robert Bensch, Tuan Leng Tay, Thomas Brox, Dominic Mai, Katharina Seiwald, Cristina Dal Bosco, and Yassine MARRAKCHI. U-Net: deep learning for cell counting, detection, and morphometry. *Nature Methods*, 16(1):67–70, 2018. ISSN 1548-7091. doi: 10.1038/s41592-018-0261-2.

Appendix A

Methods and Standard Protocols

A.1 Cell Culture

A549 Cell Culture

Human lung carcinoma epithelial cells, adherent

Sources: The one with the higher passage is from Carsten Rudolph, Klinikum, 2006, most likely from ATCC, cultured in MEM; the one with the low passage is ordered from DSMZ, thus A549 ATCC® CCL-185™, 2018; cultured in DMEM

Culture media:

- MEM/DMEM GlutaMAX Gibco
- 10% FCS

Doubling time: ~31h h

Passaging:

1. Suck off the old media from the T25 flask (yellow closed cap, with protein bottom)
2. Wash cells with 5 mL PBS
3. Suck PBS off and add 500 μ L 0.5% EDTA/Trypsin
4. Incubate for 3 min at 37 °C and 5% CO₂
5. If the cells are rounded, but not detached, hit the flask gently to get them in solution
6. Add 4.5 mL media to stop trypsinisation and re-suspend them thoroughly
7. Take out 20 μ L CS for Neubauer counting chamber and count them (see WIKI how to count)
8. Centrifuge them at 800 rpm for 3 min
9. Suck off the media and re-suspend the cell pellet again in 5 mL media

Dilute the cell suspension as the following: 1:3 for two days (e.g. Mo-Wd), 1:4 over the weekend

Freezing:

- 1.5 mL of final Cryomedium (with cells) per cryovial, preparation of 6 vials
Total volume: 9 mL. 1:1 dilution of CS and Cryomedium 4.5 mL Cryomedium:
- 900 μ L DMSO (20%, 10% final), 1.35 mL FCS (30%, final: 15%) and 2.25 mL CM (50%, final: around 75% with cells). Put it on ice.
- Label cryovials
- Prepare 4.5 mL of a cell suspension with 4 Mio cells/mL
- Cryomedium mixed with CS final cell concentration: Around 2 Mio cells/mL, so \sim 3 Mio cells per Cryovial

Thawing:

- Suspend the frozen cells drop by drop carefully in 9 mL of pre-warmed CM (MEM/DMEM GlutaMAX, 10% FCS)
- Centrifuge for 3 min, 700 rpm
- Re-suspend in 10 mL CM, seed in a T75 flask (due to the big pellet). If it is a smaller pellet than re-suspend the pellet in 5 mL and seed them in a T25 flask
- CM change at the following day
- Split them two days after freezing, three days if they are not 70-80% confluent after two days (centrifuge for 3 min, 800 rpm, seed 20 000 cells/cm², see passaging)

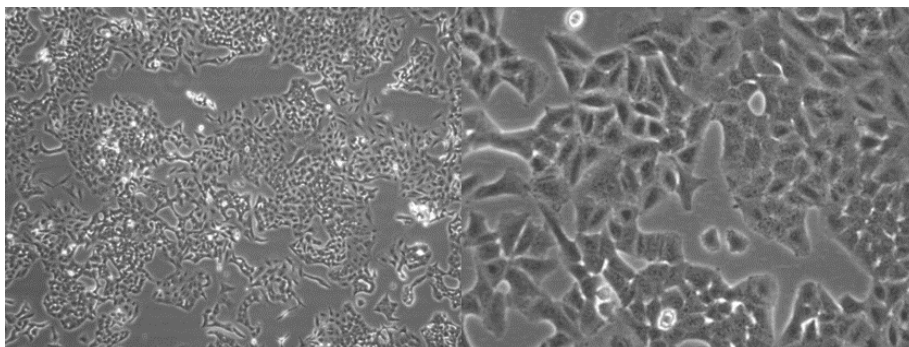


Figure A.1: A549 cells with 5x objective (left) and 20x objective (right).

Huh7 Cell Culture

Human liver carcinoma (Hepatoma)

Source: I.A.Z., Munich

General:

- Culture in T25 Sarstedt flask (yellow lids)
- 5 mL media per T25 flask
- mean generation time ~30 h

Cell culture medium:

- RPMI 1640 + GlutaMAX Gibco
- 10% FCS
- 5 mM HEPES
- 1 mM Sodiumpyruvate

Passaging:

1. remove old media
 2. washing with ~5 mL PBS
 3. 0.5 mL 0.5% Trypsin/EDTA per T25 for 2 min in incubator (additional 1 min if cells still adherent)
 4. re-suspend with additional 4.5 mL fresh cell culture medium
 5. collect cell suspension in 15 mL reaction tube
 6. counting cells using Neubauer counting chamber centrifugation 800 rcf/3 min/RT
 7. seeding of cells in needed concentration in new T25 flask with a total volume of 5 mL
- due to cell metabolism it's normal that there are fringy cells after longer cultivation (pH change of media)
 - a medium exchange after 48 h of cultivation is recommended

Freezing:

1. 1.5 mL of final Cryomedium (with cells) per cryovial, preparation of 6 vials
 - Total volume: 9 mL. 1:1 dilution of CS and Cryomedium 4.5 mL Cryomedium:
2. 900 μ L DMSO (20%, 10% final), 1.35 mL FCS (30%, final: 15%) and 2.25 mL CM (50%, final: around 75% with cells). Work on ice.
3. Label cryovials
4. Prepare 4.5 mL of a cell suspension with 4 Mio cells/mL
5. Cryomedium mixed with CS final cell concentration: Around 2 Mio cells/mL, so \sim 3 Mio cells per Cryovial

Thawing:

1. Suspend the frozen cells drop by drop carefully in 9 mL of pre-warmed CM
2. Centrifuge for 3 min, 700 rpm
3. Re-suspend in 10 mL CM, seed in a T75 flask (due to the big pellet). If it is a smaller pellet than re-suspend the pellet in 5 mL and seed them in a T25 flask
4. CM change at the following day
5. Split them two days after freezing, three days if they are not 70-80% confluent after two days (centrifuge for 3 min, 800 rpm, seed 20 000 cells/cm², see passaging)

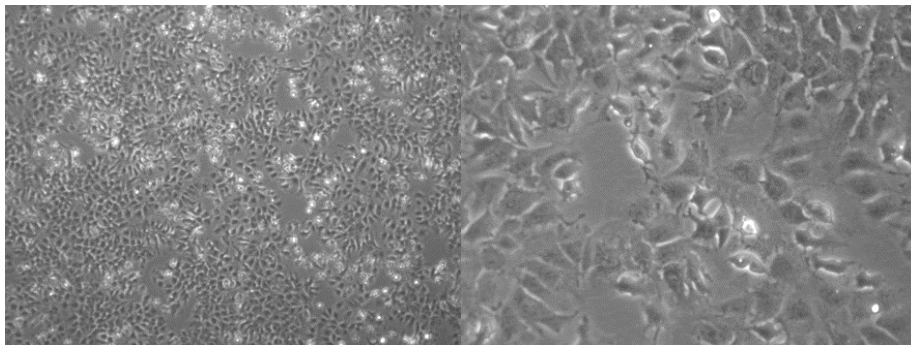


Figure A.2: Huh7 cells with 5x objective (left) and 20x objective (right).

MOLM-13 Cell Culture

Acute myeloid leukemia (AML), suspension cell line Source: DSMZ, provided by Prof. Fuat Oduncu chair in the Medical School on 28.01.14 (collaborateur of Elisavet Chatzopoulou)

Doubling time: ~ 19-20 h.

Medium:

- RPMI GlutaMAX Gibco
- 20% FCS, but can also be changed to 10% FCS

Passaging:

1. Mix the cell suspension and pipet it in a 15 mL falcon
2. Take out 20 μ L for the Neubauer counting chamber (see WIKI how to count)
3. Centrifuge at 800 rpm for 3 min
4. Suck off the supernatant and re-suspend the cell pellet again in 5 mL media
5. Dilute the cell suspension as the following:
 - 200 000 cells/mL (mostly ~ 1:14) for two days (Mo-Wd, Wd-Fr)
 - 150 000 cells/mL over the weekend (Fr-Mo)

Freezing:

1. Centrifugation for 3 min at 800 rcf as usual
2. Resuspend the cell suspension in a volume of Cryo media to have finally ~ 3 Mio cells/mL.
3. Cryomedium: 70% CM (RPMI 1640 with 10-20% FCS), 20% FCS and 10% DMSO.
4. Overnight in -80°C, afterwards storage in N₂ tank.

Thawing:

1. Take the cryovial out of the liquid nitrogen (gloves, goggles!)
2. Warmed up in the hands, then completely in the water bath
3. Suspend cells in 9 mL of MOLM CM (Gibco RPMI GlutaMAX and 10-20% FCS)
4. Centrifuge for 3 minutes at 700 rpm
5. Re-suspend pellet in 10 mL CM (big pellet)
6. Seed in T75 flask
7. Change the media after one day

Jurkat Cell Culture

Human peripheral blood T lymphocytes, acute T cell leukemia

Source: Prof. Vollmar, Biological Pharmacy, DMSZ authenticated and mycoplasma tested, ACC 282

Doubling time: ~ 24 h

Medium:

- RPMI 1640 GlutaMAX
- 10% FCS
- 1 mM sodiumpyruvate

Passaging:

- optimum cell density between 0.1×10^6 cells/mL - 1×10^6 cells/mL (max 1.5×10^6 cells/mL)
- split every two days
- only centrifuge if the media should be changed completely, for example for experiments. Therefore, centrifuge at 400 g, 5 min at room temperature. Re-suspend in fresh media.
- If the cells are happy, cell aggregates or isles of cells are visible
- If the cells are stressed, dead cells are visible as black dots on the bottom of the flask, e.g. after exposure to cytotoxic solutions or after thawing.

Freezing:

- let the cells grow very dense in three T75 flasks
- count the cells while centrifuging the cell suspension at 400 g for 5 min
- dilute the cells to 2 Mio cells/mL to have finally 1 Mio cells/mL in the cryo vial
- For 6 Cryovials a 1,6 ml:

Ratio 1:1 of cell suspension and cryo media:

- 2,5 mL 10% FCS media
- 2 mL FCS ~20% FCS finally
- 0,5 mL DMSO ~ 5% finally

4.8 mL of this mixture and 4.8 mL of cell suspension

- Important: work on ice! And freeze gently and slowly (use purple cryo vial container)

Thawing:

- Re-suspend the cells in 10 mL **20% FCS** media
- Centrifuge for 5 min at 400 g
- Re-suspend the cells in 5 mL **20% FCS** media
- Seed in T25 flask
- One or two days after freezing: change the media (maybe again in 20% FCS media)
- let them grow longer than usual; optimum $> 0.5 \times 10^6$ cells/mL and $>90\%$ viability
- centrifuge the first passages to get rid of cell fragments
- culture is then performed in 10% FCS media (see above)

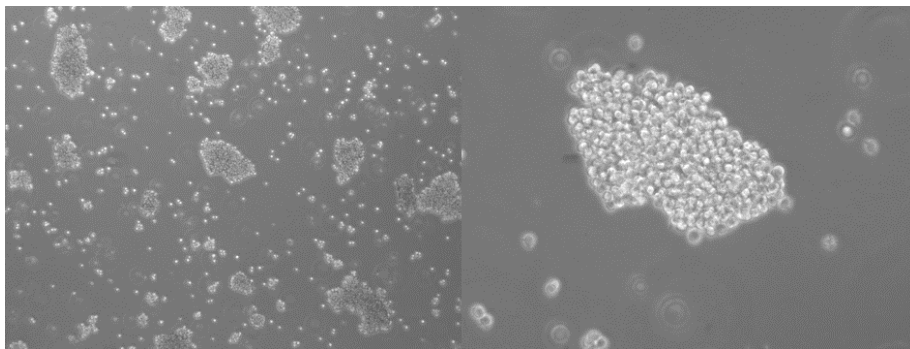


Figure A.3: Healthy Jurkat cells form aggregates, which are shown in 5x magnification (left) and 20x magnification (right).

A.2 Microscale Plasma-Initiated Protein Patterning (μ PIPP)

Reagents:

- PLL-PEG (2) (2mg/mL) in 150 mM NaCl and 10 mM Hepes (Gibco), pH = 7,4 (PLL (20)-g (3.5)-PEG (2), abbreviated PLL-PEG(2), SuSoS) store at 4°C
- FN (1 mg/mL) in PBS (Yoproteins) store at 4°C
- Dimethylsiloxan monomer
- Silicon elastomer curing agent (crosslinker)
- Sterile PBS
- Ethanol
- Milli Q water
- Isopropanol for cleaning the surfaces

FN and PLL-PEG(2) are stored in the s.p.s.-Box (surface patterning stuff) in the fridge in the membrane lab

Equipment:

- μ -slide 8 well, uncoated (ibidi) or ibidi foil uncoated and sticky 8well slide
- Si-wafer with structures
- (sterile) hood
- Tweezers
- Cutter, razor blades, cutting board
- Pipettes
- Plasma cleaner
- Desiccator
- Petri dishes

How to prepare the PDMS-stamp:

- Weighing: 11:1 mixture of PDMS (10 m/m monomer, 1 m/m crosslinker) (you need 10 g for one complete wafer)
- Get rid of bubbles with the desiccator for 0.5 h
- Blow PDMS crumbs, dust and so on with the air pistol from the wafer

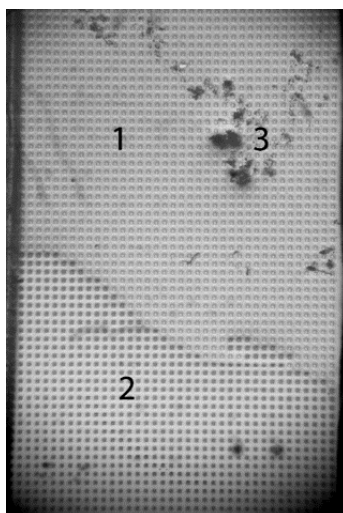
- Pour the PDMS onto the Si-wafer with 3 mm thickness
- Place the wafer into the desiccator for another 0.5 h (or longer if needed)
- Cure overnight in the 50°C oven

How to cut the PDMS-stamp:

- Cut with the scalpel eight squares out of the casting
- Be careful: the Si-wafer can break, so don't use too much pressure
- Turn and put them on the cutting mat, the structure is now facing you
- Every edge of the square has to be cut to let the plasma flow underneath, use the blade here
- Cut each square in half
- Clean the blade with a tissue and isopropanol after every cut

Place two stamps in each well and make sure that plasma is accessible to the structures; the structure is now on the bottom of the slide parts which are not covered by the stamp get hydrophilized.

Check attachment of the stamp in your dish with the stereo microscope before the plasma process:



- 1 = area with not attached structures (light)
- 2 = area with structures attached to the dish (dark)
- 3 = particles under the stamp

Do not mark anything with an edding before the plasma treatment, afterwards it is okay.

Put the sample into the plasma cleaner (side of the stamp parallel to the table side):

- Times:
 - 7 min pump,
 - 2 min flood with gas
 - 3 min plasma process
 - Pressure: 0.2-0.44 mbar (before process), flow = ~ 5 (only adjustable when GAS-button is pressed)
 - Power: 70 % at 4.5 (35 W) or 100% at 9.9 for 50 W (depends on plasma cleaner)

PLL-PEG treatment:

- Put the stamps right after plasma cleaning in the hood
- Incubate the lid of the slide with ethanol for 5 minutes, afterwards for 1 minute with Milli Q
- Add a drop PLL-PEG(2) close to each stamp (4 μ L per stamp); capillary action will attract the liquid underneath the stamp. Don't touch the stamp with the tip of your pipette.
- Incubate for at least 25 min

Alternative: You can also use the ibidi untreated foils, place the stamps, plasma treat the foils add the PLL-PEG and rinse the foil once with 800 μ L MilliQ after removing the stamps. Let the foil dry and glue a sticky 8 well slide onto it. Store it at RT. Add the FN solution directly before seeding the cells.

Fibronectin treatment

- Add 300 μ L PBS in each well, remove the stamps in one pull and strictly avoid drying of the substrate
- FN working solution (35 μ g/mL for A549): dilute FN-Stock solution (1 mg/mL) 1:28.6 in PBS
- For Huh7 cells, e.g. usually 50 μ g/mL are used
- Remove PBS and add 180 μ L FN working solution in each well
- Incubate for 45 min

Afterwards dilute FN with PBS, wash three times with 300 μ L PBS each well and leave them in 240 μ L PBS for storage over night at 4 °C.

Incubate with medium before seeding cells.

A.3 Protocol for the Fabrication of 3D PDMS Multi-Cell-Wells

Equipment:

- Desiccator
- Oven with 50 °C
- Two normal bar clamps
- Bar clamp, where increase the pressure by not seizing but by clamping (e.g. from ibidi)
- Two metal plates
- Plate of gum or similar
- Ibidi foils, bigger than the normal microscope ones
- 5 mL syringe with needle
- Tweezers
- POM wafer
- PDMS (10:1)

Procedure:

1. Prepare 5.5 mL of PDMS solution (5 mL of PDMS monomer and 0,5 mL crosslinker)
2. Fill it in the syringe (with the open end closed with the needle and the safety cap) and desiccate it for 30-45 min to remove bubbles. Let the syringe open; do not close it with the stamp.
3. Fill the bubble free PDMS, with the needle very close to the structure, in the wafer.
4. Let the PDMS settle down for 1 h.
5. Remove bubbles with a needle if there are still some.
6. Remove the foil from the ibidi foil and place now the clean site gently on the wafer with the PDMS. The best way is to hold the foil on one side and to place it on the structures gradually. You can follow the procedure; the PDMS will suck onto the foil. The ibidi foil guarantees a smooth bottom of the structures to ensure the adhesion afterwards on the glass bottom of the dish.
7. Place the gum foil on top of the ibidi foil. This will distribute the pressure more even and balance some irregularities in the metal plates.

8. Place the sandwich between the two metal plates.
9. Fix the sandwich with the clip bar clamp directly above and underneath the POM wafer. With this type of bar clamp, it is easier not to get the sandwich out of place.
10. As soon as this clamp is fixed, place the other two bar clamps next to the first bar clamp.
11. Now you can remove the first bar clamp.
12. Let the structure harden overnight at room temperature. Take care that excessive PDMS can be released and a tissue underneath can be helpful.
13. Harden this formation in the oven overnight.
14. Remove the clamps and peel off the foils gently.
15. Place the tweezers in one edge of the structure and pull out the structures out of the wafer.

A.4 Fluorescence Microscopy

Concentrations of the Fluorescence Markers

Marker	Concentration
MOMP	
TMRM	10 nM
Mito Tracker Deep red	0.0066%
Oxidative Stress/Burst	
CellROX Deep Red	100 nM
CellROX orange	100 nM
CellROX green	100 nM
LMP	
Lysotracker Deep Red	75 nM
Calcium level	
Calbryte-630	1 μ M
Calbryte-590	1 μ M
Calbryte-520	1 μ M
Caspase 3/7 Activation	
CellEvent Caspase 3/7 Green	3%
Phosphatidylserine Flip	
pSIVA-IANBD	2%
PMP	
Propidium Iodide	1%
Toto-3 Iodide	1 μ M

Table A.1: Concentrations of Fluorescence Markers.

Absorption- and Emissionmaxima of the Fluorescence Markers

Marker	Absorbance [nm]	Emission [nm]	Filter
MOMP			
TMRM	548	574	YFP
Mito Tracker Deep red	644	665	Cy5
Oxidative Stress/Burst			
CellROX Deep Red	640	665	Cy5
CellROX orange	545	565	YFP
CellROX green	485	520	GFP
LMP			
Lysotracker Deep Red	647	688	Cy5
Calcium level			
Calbryte-630	608	626	Cy5
Calbryte-590	573	588	YFP
Calbryte-520	492	514	GFP
Caspase 3/7 Activation			
CellEvent Caspase 3/7 Green	502	530	GFP
Phosphatidylserine Flip			
pSIVA-IANBD	478	525	GFP
PMP			
Propidium Iodide	535	617	YFP
Toto-3 Iodide	642	660	Cy5

Table A.2: Absorption- and emission maxima of the used fluorescence marker and the corresponding filter.

Exposure Times of the Fluorescence Markers

Marker	Exposure Time
MOMP	
TMRM	300 ms
Mito Tracker Deep red	300 ms
Oxidative Stress/Burst	
CellROX Deep Red	300 ms
CellROX orange	300 ms
CellROX green	300 ms
LMP	
Lysotracker Deep Red	150 ms
Calcium level	
Calbryte-630	150 ms
Calbryte-590	150 ms
Calbryte-520	150 ms
Caspase 3/7 Activation	
CellEvent Caspase 3/7 Green	300 ms
Phosphatidylserine Flip	
pSIVA-IANBD	300 ms
PMP	
Propidium Iodide	300 ms
Toto-3 Iodide	150 ms

Table A.3: Exposure times of fluorescence markers.

List of figures

1.1	Relation between cause and correlation.	1
2.1	Motivation for Single-Cell Time-Lapses.	5
2.2	Overview of cell death types.	8
2.3	Process of apoptosis.	9
2.4	Live-cell imaging on single-cell arrays.	11
2.5	Chemical Structure LysoTracker.	13
2.6	Exemplary 30 h time traces of LysoTracker.	14
2.7	Chemical Structure of TMRM Marker.	15
2.8	Exemplary 30 h time traces of TMRM marker in NP induced apoptosis.	16
2.9	Exemplary 24 h time traces of TMRM marker in chemotherapy.	17
2.10	Exemplary 24 h time traces of CellROX ROS detection agent in combinatorial chemotherapy induced apoptosis	19
2.11	Typical and atypical time traces of the CellROX marker.	19
2.12	Exemplary time traces of Calbryte-520 of 24 h in chemotherapy.	21
2.13	Caspase marker mode of action.	22
2.14	Exemplary 30 h time traces of CellEvent green in NP induced apoptosis.	22
2.15	Mode of action pSIVA marker.	23
2.16	Exemplary 30 h time traces of pSIVA-IANBD in NP induced apoptosis.	24
2.17	Mode of action PMP markers.	24
2.18	Chemical Structure Toto-3 Iodide.	25
2.19	Chemical Structure Propidium Iodide.	25
2.20	Exemplary 30 h single-cell time traces of PI in NP induced apoptosis.	26
2.21	Time traces early marker with fitting functions.	28
2.22	Time traces late marker with fitting functions.	29
2.23	Workflow.	31
3.1	Overview of the apoptosis signaling cascade induced by 58 nm sized cationic amino-modified polystyrene (PS-NH ₂) nanoparticles.	35
3.2	Overview of the pathways type I and type II in FasL induced apoptosis.	37
3.3	MNM induced cell death in monolayer and single cells.	40
3.4	Distribution of event times of early markers in A549 cells.	41
3.5	Scatter plots of early marker in A549 cells.	43
3.6	Scatter plots of early markers in Huh7.	44
3.7	Schematic model of LMP and MOMP pathways in NP induced apoptosis in A549 cells.	46

List of figures

3.8	Distribution of event times of late markers in A549 cells.	47
3.9	Scatter plots of OxBurst and PI correlation in A549 cells.	48
3.10	Correlation late marker with early marker in A549 cells.	49
3.11	Correlation of ROS with MOMP and LMP.	51
3.12	results Cathepsin D Inhibition with pepstatin A.	52
3.13	Results of FasLigand Experiments.	54
3.14	Gamma distributions of early markers in A549 and Huh7 cells.	56
4.1	Chemical structure of Etoposide.	57
4.2	Mode of action Etoposide.	58
4.3	Chemical structure of PS89.	60
4.4	Hypothetic Pathway in Combinatorial Chemotherapy.	62
4.5	Histograms event time distributions.	64
4.6	Early Event Time Correlations in Combinatorial Chemotherapy.	65
4.7	Signaling Cascade CC.	66
4.8	Lag Time of Depolarisation.	69
4.9	Pie chart of Cellular Response.	70
4.10	Heterogeneity in Cellular Response.	72
4.11	Gamma fits to delay time distributions.	73
4.12	Dynamic Bliss Analysis of Early Marker Combinations.	74
4.13	Dynamic Bliss Analysis of PMP.	75
4.14	Analysis of Triple Combinations.	77
5.1	Polycarbonate Foil	82
5.2	Autofluorescence of seven different potential microwell materials	90
5.3	Decisionmatrix for different microwell materials.	93
5.4	Two HSC Differentiation Models.	95
5.5	Photographic and schematic illustration of PDMS microwells.	98
5.6	Time to first division.	101
5.7	Cell cycle duration.	101
6.1	Outlook Specific Patterning	105
A.1	A549 cell culture.	130
A.2	Huh7 cell culture.	132
A.3	Jurkat cell culture.	135

List of abbreviations

μPIPP	Microscale Plasma-Initiated Protein Patterning
AML	Acute Myeloid Leukemia
CASP	Caspase-3/7
DA	Diacylate
DMA	Dimethacrylate
DNA	Desoxyribonulceinacid
ETO	Etoposide
FACS	Fluorescence Activated Cell Sorting
FN	Fibronectin
HHBS	Hanks Buffer with 20 mM HEPES
HSC	Hematopoetic Stem Cell
LMP	Lysosomal Membrane Permeabilization
MDS	Myelodysplastic Syndrome
MOMP	Mitochondria Outer Membrane Permeabilization
MTT	3-(4,5-dimethylthiazol-2-yl)-2,5-diphenyltet-razolium bromide
NCCD	Nomenclature Committee on Cell Death
NP	Nanoparticle
OxBurst	Oxidative Burst
PC	Polycarbonate
PCA	Principal Component Analysis
PCD	Programmed Cell Death
PDI	Protein Disulfide Isomerase
PDMS	Polydimethylsiloxane
PEG	Polyethylen glycol
PhS-Flip	Phosphatidylserine Flip
PI	Propidium Iodide
PLL	Poly-L-Lysin
PMP	Plasma Membrane permeabilization
PS-NH ₂	Amino-modified Polystyrene (nanoparticles)
ROS	Reactive Oxygen Species
STS	Staurosporine
TMRM	Tetramethylrhodamine
TOP2	Topoisomerase 2
Toto-3	Toto-3 Iodide

Danksagung

An dieser Stelle möchte ich mich bei allen bedanken, die mich bei der Entstehung dieser Doktorarbeit unterstützt haben. Besonders danken möchte ich...

...meinem Doktorvater **Prof. Joachim Rädler**, der mir die Möglichkeit gegeben hat, am Biophysiklehrstuhl als Chemikerin meine Doktorarbeit zu machen, der meinen Fokus immer wieder auf grundlegende Fragen gelenkt hat und mich immer dazu bewegt hat, noch einen Schritt weiter zu denken. Ich habe viel gelernt in den letzten 3 Jahren, vielen Dank!

...meiner Zweitkorrekturin **Prof. Angelika Vollmar** aus der biologischen Pharmazie, die mir immer neue Sichtweisen auf meine Daten gegeben hat,

...meinen Kollaborationspartnern **Dr. Katharina Götze** und **Michele Kyncl** vom Klinikum r. d. Isar, **Dr. Carsten Marr** und seiner Gruppe aus der computationellen Biologie, **Prof. Kenneth Dawson** und **Dr. Daithi Garry** von der UCD Dublin sowie **Dr. Bernhard Wunderlich** und **Dr. Jenny Oberg** der Firma Heidenhain,

...dem **Projektcluster NanoMILE**, mit dem ich viele interessante Meetings und Konferenzen besuchen konnte,

...**CeNS** für den Travel Award, das BPS Meeting in San Francisco war super,

...**NIM** für das interdisziplinäre Netzwerk des Graduiertenkollegs,

...meiner lieben Dinnerrunde **Ricarda, David, Bene und Peter** für die vielen köstlichen Menüs, Eisnachmittage und Tanzeinlagen,

...dem office2000, **Jürgen** und **Valentin** für die vielen Eisbachsprints mit Mr. Crab,

...**Philipo** und **Flo** für die vielen erheiternden Mittagspausen und 'tiefsinnigen' Gesprächen,

...**Ellie**, because you always made me laugh!

...**Timon**, der mir immer wieder gezeigt hat was im Leben wirklich wichtig ist,

...der lieben **Sonja** für die vielen entspannten aktive Pause-Pilatesstunden,

...**Daniel** und **Julie**, für die tatkräftige Unterstützung in der Datenanalyse,

...unserem Rettungsteam **Charlott, Philipp, Susi** und **Gerlinde**,

...meinen **ehemaligen Kollegen** Tobias, Matthias, Judith, Miriam, Janina R. und Fang,

...meinen **ehemaligen Bürokollegen** Anton, Janina L., Eva, Luisa, Yasmin,

...meinen jetzigen Bürokollegen, **Anita, Christoph** und **Sophia**, ich bin immer gerne ins Büro gegangen,

...meinen **Studenten** und **HiWis**,

...den **Korrekturlesern** Ricarda, Peter, Amelie, Daniel und Ellie für das Entwirren meiner langen Sätze,

...dem **ganzem Lehrstuhl** für die lustigen Faschings-, Halloween- und Weihnachtsfeiern, Betriebsausflüge und Anholzfahrten, sowie den **Rennrädlern** für die vielen motivierenden Laufrunden,

...meinem **Chemielehrer** aus der Oberstufe **Herrn Robert Wagner**, ohne dessen faszinierende Stunden ich nie Chemie studiert hätte!,

...meiner lieben Schwester **Victoria** und **meinen Eltern**, weil sie immer für mich da waren und mich in allen Lebenslagen immer unterstützt haben. DANKE. Ohne eure Gelassenheit, Bodenständigkeit und Liebe würde ich nicht da stehen wo ich heute bin.

...**mio cuore**, perché mi ami sempre così com'io sono, e tu ci sei sempre per me.

